UAB
Universitat Autònoma de Barcelona

Testing the ΛCDM Model: Cross-Correlations of Cosmic Voids and CMB Lensing

Umut Emek Demirbozan

Testing the ΛCDM Model: Cross-Correlations of Cosmic Voids and CMB Lensing

Umut Emek Demirbozan

Advisors:

Dr. Ramon Miquel

Dr. Seshadri Nadathur

A thesis submitted for the degree of

Philosophiae Doctor (PhD) Departament de Física

Universitat Autònoma de Barcelona

In loving memory of my grandmothers,

and with deep gratitude to my father and stepmother,
for their support and inspiration.

"For small creatures such as we, the vastness is bearable only through love."

— Carl Sagan

"Two things are infinite: the universe and human stupidity; and I am not sure about the universe."

— Albert Einstein

I, Umut Emek Demirbozan, declare that this thesis titled, "Testing the ΛCDM Model: Cross-Correlations of Cosmic Voids and CMB Lensing" and the work presented in it are my own. I confirm that:

- This work was done wholly or mainly while in candidature for a research degree at this University.
- Where any part of this thesis has previously been submitted for a degree or any other qualification at this University or any other institution, this has been clearly stated.
- Where I have consulted the published work of others, this is always clearly attributed.
- Where I have quoted from the work of others, the source is always given. With the exception of such quotations, this thesis is entirely my own work.
- I have acknowledged all main sources of help.
- Where the thesis is based on work done by myself jointly with others, I have made clear exactly what was done by others and what I have contributed myself.

Abstract

Modern cosmology is undergoing a rapid transformation, driven by unprecedented data from large-scale structure surveys of galaxies and observations of the cosmic microwave background (CMB). Now more than ever, it is crucial to collectively analyze multiple datasets to gain deeper insights and fully exploit the wealth of available information. Consequently, the cross-correlation of large-scale structures (LSS) of the universe with the CMB is becoming an increasingly vital and rapidly advancing field.

The largest observable structures in the universe, known as cosmic voids, are expansive regions characterized by a relative lack of galaxies. These cosmic voids influence the CMB through gravitational lensing, causing a negative imprint on the CMB convergence (κ). This effect provides insight into the distribution of matter within voids, and can also be used to study the growth of structure. In addition, voids are also the regions where we can observe secondary CMB anisotropies caused by the Integrated Sachs-Wolfe (ISW) effect as colder than usual CMB temperature in void positions. This effect is a direct probe of the acceleration of the Universe.

Motivated by ongoing discussions regarding the strength of the ISW effect caused by voids and the possible connection of a large void to the CMB Cold Spot, this thesis extends these studies to include the CMB lensing imprints of voids.

As the standard model of cosmology, Λ Cold Dark Matter (ΛCDM), fits a great amount of different cosmological observations with incredible efficiency, our main motivation is to test this model using superstructures in the LSS and the CMB with the help of N-body simulations.

We begin by utilizing DES Year-1 data, employing two distinct void finder algorithms— 2D and `VIDE`—along with a template fitting method which includes

Gaussian filtering of the CMB lensing convergence (κ) map and stacking CMB patches on void centers. Moreover, we also cross-correlate voids with the mass maps produced by Dark Energy Survey Y3 data set to show the consistency of produced mass maps.

We then measure this lensing imprint by cross-correlating the *Planck* CMB (κ) map with voids identified in the DES Y3 data set, covering approximately 4,200 deg^2 of the sky. We again use two distinct void-finding algorithms: a 2D void-finder which operates on the projected galaxy density field in thin redshift shells, and a new code, `Voxel`, which operates on the full 3D map of galaxy positions. We employ an optimal matched filtering method for cross-correlation, using the MICE N-body simulation both to establish the template for the matched filter and to calibrate detection significances. Using the DES Y3 photometric luminous red galaxy sample, we measure A_κ, the amplitude of the observed lensing signal relative to the simulation template, obtaining $A_\kappa = 1.03 \pm 0.22$ (4.6σ significance) for `Voxel` and $A_\kappa = 1.02 \pm 0.17$ (5.9σ significance) for 2D voids, both consistent with ΛCDM expectations. We additionally invert the 2D void-finding process to identify superclusters in the projected density field, for which we measure $A_\kappa = 0.87 \pm 0.15$ (5.9σ significance). We then show that the leading source of noise in our measurements is *Planck* noise, implying that future data from the Atacama Cosmology Telescope (ACT), South Pole Telescope (SPT) and CMB-S4 will increase sensitivity and allow for more precise measurements.

Resum

La cosmologia moderna està experimentant una ràpida transformació, impulsada per dades sense precedents de les cartografies d'estructures a gran escala de galàxies i les observacions del fons còsmic de microones (CMB). Ara més que mai, és crucial analitzar col·lectivament múltiples conjunts de dades per obtenir una comprensió més profunda i aprofitar plenament la riquesa d'informació disponible. En conseqüència, la correlació creuada de les estructures a gran escala (LSS) de l'univers amb el CMB s'està convertint en un camp cada vegada més vital i en ràpida evolució.

Les estructures observables més grans de l'univers, conegudes com a buits còsmics, són regions extenses caracteritzades per una falta de galàxies. Aquests buits còsmics influeixen en el CMB a través del fenomen de lent gravitacional, causant una impressió negativa en la convergència del CMB (κ). Aquest efecte proporciona una visió de la distribució de la matèria dins dels buits i també pot ser utilitzat per estudiar el creixement de l'estructura. A més, els buits també són les regions on podem observar l'efecte Sachs-Wolfe integrat (ISW) com a temperatura del CMB més freda del normal en les posicions dels buits. Aquest efecte és una sonda directa de l'acceleració de l'Univers.

Motivats per les discussions en curs sobre la força de l'efecte ISW causat pels buits i la possible connexió d'un gran buit amb el Cold Spot del CMB, aquesta tesi amplia aquests estudis per incloure les empremtes de lent del CMB dels buits.

Com el model estàndard de cosmologia, el model de Matèria Fosca Freda Lambda (ΛCDM), s'ajusta a una gran quantitat d'observacions cosmologiques diferents amb una eficiència increïble, la nostra principal motivació és testejar aquest model utilitzant superestructures en el LSS i el CMB amb l'ajuda de simulacions de molts cossos.

Comencem utilitzant dades del primer any de DES, emprant dos algoritmes de cerca de buits distints: 2D i `VIDE`, juntament amb un mètode d'ajustament de plantilles. Això implica filtrar gaussianament el CMB i reescalar retalls del CMB centrats en posicions de buits. A més, també correlacionem creuadament els buits amb els mapes de masses produïts pel conjunt de dades dels 3 primer anys de DES per mostrar la consistència dels mapes de masses produïts.

Després mesurem aquesta empremta de lent correlacionant creuadament el mapa de convergència de lent del CMB de *Planck* (κ) amb buits identificats en el conjunt de dades DES Y3, cobrint aproximadament 4.200 graus quadrats del cel. Utilitzem de nou dos algoritmes de cerca de buits distints: un cercador de buits 2D que opera sobre el camp de densitat de galàxies projectat en closques de redshift fines, i un nou codi, `Voxel`, que opera sobre el mapa complet en 3D de posicions de galàxies. Emprem un mètode de filtratge òptim per a la correlació creuada, utilitzant la simulació molts cossos MICE tant per establir la plantilla per al filtre com per calibrar les significances de detecció. Utilitzant la mostra de galàxies roges lluminoses fotomètriques a DES Y3, mesurem A_κ, l'amplitud del senyal de lent observat en relació amb la plantilla de simulació, obtenint $A_\kappa = 1.03 \pm 0.22$ (significància de 4.6σ) per `Voxel` i $A_\kappa = 1.02 \pm 0.17$ (significància de 5.9σ) per buits 2D, ambdós consistents amb les expectatives de ΛCDM. A més, invertim el procés de cerca de buits 2D per identificar supercúmuls en el camp de densitat projectat, per als quals mesurem $A_\kappa = 0.87 \pm 0.15$ (significància de 5.9σ). Llavors mostrem que la principal font de soroll en les nostres mesures és el soroll de *Planck*, la qual cosa implica que futures dades del Telescopi de Cosmologia d'Atacama (ACT), el Telescopi del Pol Sud (SPT) i el CMB-S4 augmentaran la sensibilitat i permetran mesures més precises.

Acknowledgements

Here I am, in very different circumstances than planned. Throughout this intense journey, I faced difficulties I had not encountered before in my life. Yet, I have arrived at the end of this journey. In many ways, I could have done things much better. I still believe that I did my best when the situation was not in my favor. A PhD is an education in the end, and if it had been a smooth journey, the gains in problem-solving would not have arisen. I now feel much more comfortable handling dead-ends and quickly identifying bottlenecks that can extinguish a project. I feel like I have made almost every possible mistake that can be made, and by doing so, I have gained skills and confidence. I feel comfortable handling such situations and am better prepared for my next projects. Although most of my life circumstances tried to hold me back on this journey, I did not give in to these difficulties. I am glad that I was there for my father when my help and opinions led to saving his life during complex medical situations. Most of my work consisted of solving complex collaboration dynamics and dealing with unexpected circumstances. Yet, I am glad I was able to produce this thesis and contribute my part to humanity's knowledge in this historic time of modern cosmology.

Having said that, I extend my heartfelt gratitude to Seshadri Nadathur for his expertise and insightful explanations, which were invaluable throughout this journey. I am also deeply thankful to Ramon Miquel for his continuous guidance and oversight during the entire duration of my PhD. I also thank Andreu, Carles, Jonas, Santi, and Hui for their discussions related to my project. I thank the PREBIST programme for funding my PhD. I thank my PhD mentors for their generous support during this journey; their guidance was very important to me as I navigated numerous personal challenges. I thank the people of ICG, as my visits to ICG in Portsmouth were a

very fruitful time during my PhD. I also thank Andras Kovacs for his guidance in the first stage of my PhD.

I thank UAB Physics Department, Jordi Mompart, Carles Navau, and Francesc Poblet for handling administrative duties and patiently answering my questions and document requests. I also thank Cristina Cardenas and other administrative assistants from IFAE for the paperwork related to trips. I am very grateful for the computing help from PIC, especially Christian and Carles, for their generous assistance. I also thank my group members Marco, Giulia, Cesar, Calum, Laura, Lucy, William, and Martine for their warm conversations.

I would also like to express my understanding and empathy for my fellow students Mahboubeh, Anil, and Divya, who could not make it to this point. I send my heartfelt gratitude to Ismael Ferrero; I am honored to have him as my third author on my very first first-author paper. I also thank Anna Porredon and Santi Avila for their support and guidance throughout the DES publication journey. I send my sincere thanks to Andreu for the insightful discussions during group meetings.

I also acknowledge my lovely cats, who entered my life during the harshest COVID lockdowns, Kibaryuz and Ufaklik (Dilayla). Unfortunately, Ufaklik passed away, and Kibaryuz got lost. I also thank my friends Anil, Cem, Cemile, Eda, Chaitanya, Saptam and Kerim for their kind friendship and support.

I would also like to express my gratitude to Shadab Alam, who hosted me at the Royal Observatory of Edinburgh; my time and connections there were truly valuable. Additionally, I thank Qianjun Hang (Ellen) for hosting me at UCL and always helping with my questions. Shadab and Ellen's help was very important, and I learned a great deal from them. I thank our dog "Dob," a 12-year-old Rottweiler who refuses to die; I did not even think that he would see these days. I thank my family members and especially my aunt, Ferhan Ulke, for her sincere support. Thanks !

Contents

Introduction

Modern cosmology has witnessed a significant evolution with the advent of large-scale structure surveys and cosmic microwave background (CMB) telescopes, transitioning into a data-centric discipline. The discovery of the Universe's accelerated expansion has led to the widespread acceptance of the Λ Cold Dark Matter (ΛCDM model, grounded in Einstein's general relativity and the Friedmann-Robertson-Walker metric) (Perlmutter et al., 1999, Riess et al., 1998). This model has undergone rigorous testing, aligning closely with a wide array of observations (Eisenstein et al., 2005, Planck Collaboration et al., 2020b). Despite its remarkable success, recent findings have highlighted notable discrepancies. Among these, some measurements of the Integrated Sachs-Wolfe (ISW) effect in large cosmic voids have reported signals exceeding ΛCDM predictions derived from N-body simulations (Granett et al., 2008, Kovács et al., 2022). However, this finding has not been replicated by other studies (Hang et al., 2021, Nadathur & Crittenden, 2016). Moreover, the Cold Spot in the CMB, potentially linked with the super-sized Eridanus void, has been a subject of debate (Kovács et al., 2021, Mackenzie et al., 2017, Naidoo et al., 2016, Smith & Huterer, 2010). While it has been suggested that the Cold Spot's anomaly could be attributed to the presence of a large supervoid rather than being an intrinsic temperature fluctuation, no supervoid within the ΛCDM framework is considered capable of inducing such a pronounced effect on the CMB (Nadathur et al., 2014, Owusu et al., 2023). However, perhaps the biggest challenge to ΛCDM comes from the well-documented Hubble tension—the discrepancy between the locally measured expansion rate of the Universe and the rate predicted by ΛCDM based on early Universe observations. This tension stands out as the most significant challenge (Di Valentino et al., 2021, Freedman et al., 2024, Khalife et al., 2024, Riess et al., 2022,

Verde et al., 2023)

Given these challenges, verifying ΛCDM predictions through observational data has become critically important. Recent studies of CMB lensing effects in cosmic voids, assessing their consistency with ΛCDM expectations, are key to this verification process. If these studies reveal discrepancies, they could indicate new physics emerging from these vast under-dense regions. Therefore, the utilization of cosmic voids in cosmological research has been gaining traction. Not only do they serve as powerful tools for advancing cosmological studies, but they also provide unique opportunities to constrain the sum of neutrino masses from particle physics (Kreisch et al., 2019, Pisani et al., 2019, Verza et al., 2019, Zhang et al., 2019). Furthermore, the examination of void abundance and density profiles offers a pathway to differentiate between Modified Gravity (MG) theories and General Relativity, particularly because voids have the capacity to circumvent screening mechanisms in dense environments (Baker et al., 2018, Khoury & Weltman, 2004, Vainshtein, 1972). Therefore, it is of utmost interest to study the CMB lensing imprints of cosmic voids and their expectations within the current consensus cosmological model, ΛCDM. This thesis is organized as follows: Chapter 1 presents the background cosmological information. Chapter 2 details the void × CMB lensing results obtained from the DES Y1 dataset using two different void finders. Chapter 3 presents the cross-correlation of voids with DES Y3 weak lensing mass maps. Chapter 4 presents the void × CMB lensing results from the DES Y3 dataset by applying a matched filter method. Finally, Chapter 5 provides the discussion and conclusions of this thesis.

Chapter 1

Background and Motivation

1.1 Cosmological Background

Since the time humans have evolved sufficiently on Earth, they have wondered about their natural surroundings with strong curiosity. After the pre-historic eras, humans developed sufficient mathematical reasoning and sophisticated tools to investigate nature. Cosmology is the result of this investigation of nature at the largest possible scales; as such, it asks some fundamental questions about the Universe as a whole, such as how it started, how it has evolved, and how it will continue to evolve. To answer these questions and develop models of the Universe, it is necessary to make careful observations.

1.1.1 Expanding Universe

Starting with the beginning of the 20th century, for the first time in history, we understood that we live in a Universe much larger than our Milky Way galaxy. Shapley and Curtis had a famous debate on whether the observed "nebulae" were part of our own galaxy or not (NASA, 2020). "The Great Debate" was later resolved by the observations of Edwin Hubble, who used the Cepheid variable stars in these nebulae to measure their distances and showed that they are actually very distant, extra-galactic objects (Hubble, 1926).

Moreover, Hubble's meticulous observations revealed a direct linear correlation

between the distances to extragalactic objects and their recession velocities. This is shown in Equation 1.1 and illustrated in Edwin Hubble's original diagram in Figure 1.1. It is important to note that the H_0 referred to here is the Hubble Constant as observed today, and its value is subject to one of the most significant tensions in cosmology at the time of writing this thesis. This issue will be elaborated in more detail in subsequent chapters.

$$H_0 = \frac{v_{\text{gal}}}{d_{\text{gal}}} \tag{1.1}$$

Therefore, in modern cosmology distances are usually quoted in comoving coordi-

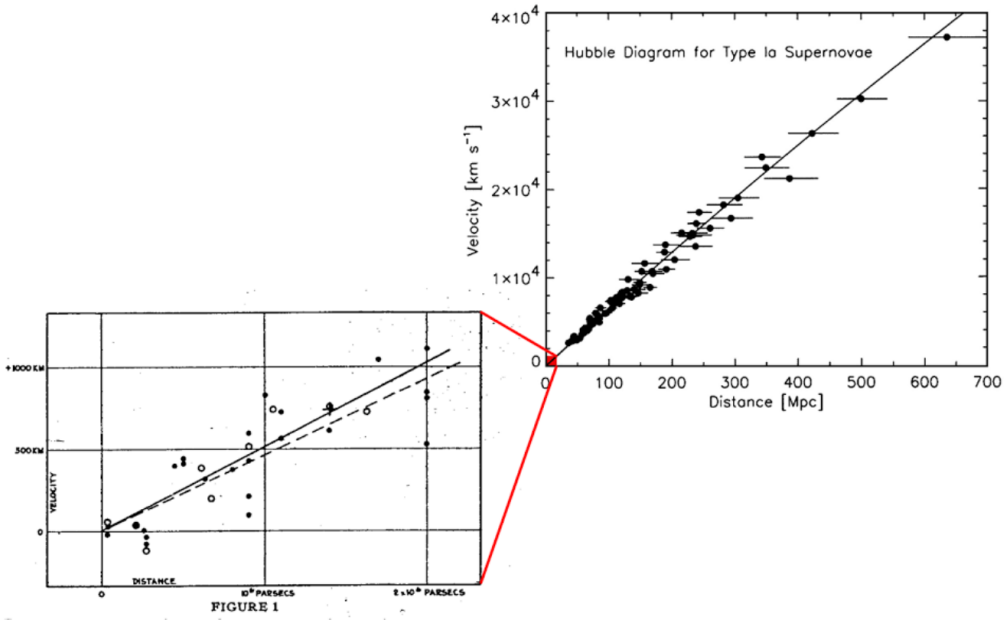

Figure 1.1: The pioneering 1929 Hubble diagram, showcasing the initial empirical evidence for the expansion of the Universe. This graph demonstrates the direct proportionality between the distances of galaxies and their respective velocities of recession, providing concrete support for the concept of an expanding cosmos as independently described by Hubble Hubble (1929) and Lemaître Lemaître (1927). On the right, a modern version of the diagram is shown as comparison. Credit:E. Hubble; R. Kirshner, PNAS, 2004

nates which are insensitive to the expansion of the Universe. Due to the uniformity of cosmic expansion, the coordinates of individual points in space remain invariant. The interval between these coordinates is termed the comoving distance (x) while the physical distance, which represents the real measurable separation between two

points in the Universe, is shown as

$$d = a(t)x. \tag{1.2}$$

In cosmology, the scale factor $a(t)$ is standardized by defining its current value as unity ($a(t_0) = 1$), with t_0 symbolizing the current age of the Universe. To describe the time variation in the scale factor, we introduce the Hubble rate

$$H(t) \equiv \frac{\dot{a}}{a} \tag{1.3}$$

The current value of the Hubble rate, denoted as H_0, is parameterized using the dimensionless Hubble parameter, h. This relationship is expressed as follows:

$$H_0 = 100h\,\mathrm{km\ s^{-1}Mpc^{-1}}.$$

Therefore, the natural units of the comoving system is Mpc/h and through this thesis the sizes and distances of the voids will be based on this framework of the comoving distance.

Moreover, the velocities of galaxies measured by Hubble in 1929, as well as those obtained from contemporary large-scale structure surveys, are derived by analyzing the spectra of galaxies. By assuming a Doppler shift for receding galaxies in an expanding Universe, the observed spectra can be compared to a non-moving reference spectrum on Earth. This allows for the calculation of the Doppler shift. Due to the expansion of the Universe, this shift typically appears towards the red end of the visible spectrum, a phenomenon known as redshift. The redshift, z, of a galaxy is defined as:

$$1 + z = \frac{\lambda_o}{\lambda_e}, \tag{1.4}$$

where λ_o and λ_e refer to the observed and emitted wavelengths, respectively. It is important to note that in reality, peculiar velocities of galaxies can affect these measurements, leading to Redshift Space Distortions (RSD) (Hamilton, 1998, Kaiser, 1987).

Furthermore, redshift is related to the radial velocity via the equation derived

from Einstein's special relativity:

$$z + 1 = \sqrt{\frac{1 + \frac{v}{c}}{1 - \frac{v}{c}}}, \tag{1.5}$$

where v is the radial velocity of the galaxy relative to the observer, and c is the speed of light.

However, on cosmological scales, redshift occurs as a consequence of the expansion of the Universe's fabric, and it is quantitatively related to the scale factor by:

$$1 + z = \frac{a_0}{a(t)} \tag{1.6}$$

We will use this equation in Section 1.1.2 within the framework of Friedmann Equations.

1.1.2 FLRW Metric and Friedmann Equations

As explained in previous sections, the beginning of the 20th Century was a pivotal moment in the history of cosmology. Einstein's general relativity and Hubble's observations rapidly changed the picture of the Universe. Perhaps, one of the most fundamental equations in cosmology was also discovered at this time.

The Cosmological Principle, also affirmed during this period, postulates that the Universe is isotropic and homogeneous on very large scales. This implies that no observer occupies a privileged position in the Universe, and the Universe appears uniform when viewed on large scales. It is noteworthy that this differs from the Perfect Cosmological Principle, wherein the Universe is supposed to be homogeneous and isotropic across both space and time, a postulate fundamental to steady-state cosmologies. Given the evident temporal evolution of the Universe, the Cosmological Principle is applicable solely in the space domain.

It is surprising to know that Friedmann's equations can also be derived from Newton's Mechanics, Newton himself had all the tools to derive this equation. The same equation can also be derived from Einstein's GR equations.

The most general isotropic and homogeneous metric of an expanding Universe

is given by the Friedmann-Robertson-Walker (FRW) metric:

$$ds^2 = -c^2dt^2 + a(t)^2\left(\frac{dr^2}{1-kr^2} + r^2d\theta^2 + r^2\sin^2\theta d\phi^2\right) \tag{1.7}$$

where spherical coordinates are used, c is the speed of light and $a(t)$ is the scale factor. The parameter k represents the curvature of the Universe and can take one of three values: $k = 1$, $k = 0$, or $k = -1$, corresponding to a closed, flat, and open universe, respectively.

- $k = 1$: Indicates a positive curvature, corresponding to a closed universe that is spatially finite. This model suggests that if you travel far enough in one direction, you would eventually return to your starting point, analogous to the surface of a sphere.

- $k = 0$: Indicates zero curvature, corresponding to a flat universe. This is the critical case between a closed and open universe and suggests that the geometry of the universe follows the rules of Euclidean geometry, where parallel lines never meet.

- $k = -1$: Indicates negative curvature, corresponding to an open universe that is spatially infinite. In this model, the universe expands forever, and the geometry is hyperbolic, meaning parallel lines diverge.

These curvature parameters play a critical role in the dynamics of the universe's expansion and its ultimate fate, influencing theories and observations in cosmology.

By setting $k = 0$ in Equation 1.7 and integrating with Equation 1.6, considering that for light $ds^2 = 0$, the comoving distance traversed by light can be determined;

$$r(z) = \int_0^z \frac{dz}{H(z)}. \tag{1.8}$$

The Friedmann Equations can be written as;

$$\left(\frac{\dot{a}}{a}\right)^2 = \frac{8\pi G}{3}\rho - \frac{k}{a^2} + \frac{\Lambda}{3} \tag{1.9}$$

and

$$\frac{\ddot{a}}{a} = -\frac{4\pi G}{3}\left(\rho + \frac{3p}{c^2}\right) + \frac{\Lambda}{3} \tag{1.10}$$

From the Friedmann Equation 1.9, there is a certain density ρ for which the universe would be flat without a cosmological constant, i.e., $k = 0$:

$$\rho_{crit} = \frac{3H^2(z)}{8\pi G} \tag{1.11}$$

The Hubble parameter is time-dependent, so the critical density also varies with cosmic time. A very useful and common definition is the density of all fluids together relative to the critical density, called the density parameter:

$$\Omega_{tot}(t) = \frac{\rho_{TOT}(t)}{\rho_{crit}(t)} \tag{1.12}$$

Using 1.11 and 1.12, we then obtain the Friedmann Equation 1.9 expressed in terms of the density parameters, scale factor, and the Hubble parameter is given by:

$$H^2(a) = H_0^2\left(\Omega_{r_0}\left(\frac{a_0}{a}\right)^4 + \Omega_{m_0}\left(\frac{a_0}{a}\right)^3 + \Omega_{k_0}\left(\frac{a_0}{a}\right)^2 + \Omega_\Lambda\right) \tag{1.13}$$

where:

- H is the Hubble parameter at any time t,
- H_0 is the current value of the Hubble parameter,
- Ω_{r_0}, Ω_{m_0}, Ω_{k_0}, and Ω_Λ are the present-day density parameters for radiation, matter, curvature, and dark energy, respectively,
- a is the scale factor at any time t,
- a_0 is the present-day scale factor, usually normalized to 1.

and therefore we obtain:

$$\Omega_{r_0} + \Omega_{m_0} + \Omega_{k_0} + \Omega_\Lambda = 1 \tag{1.14}$$

1.1.3 Einstein and General Relativity (GR)

Newtonian physics governed all physical laws up until the beginning of the 20th century, successfully explaining many phenomena but faltering with larger speeds, masses, and energies. Einstein's introduction of Special Relativity in 1905, through his Annus Mirabilis papers, challenged the Newtonian view of constant space-time (Einstein, 1905). A decade later, he further revolutionized physics with the introduction of General Relativity (GR) in 1915, proposing that gravity is not a force but the curvature of spacetime caused by mass-energy (Einstein, 1915).

General Relativity is based on the equivalence principle, which states that gravitational and inertial mass are equivalent. This principle led to the prediction of several new phenomena such as the bending of light by gravity, confirmed during the 1919 solar eclipse by Sir Arthur Eddington (Dyson et al., 1920), and the perihelion precession of Mercury's orbit (Verrier, 1859), resolving longstanding astronomical puzzles.

General Relativity has important implications for cosmology. It forms the theoretical framework for understanding diverse cosmic phenomena, including the expansion of the universe as described by the Friedmann-Lemaître-Robertson-Walker(FLRW) metric which we explained in Section 1.1.2, the existence of black holes, and the theoretical prediction of gravitational waves, observed a century later in 2015 by LIGO collaboration (Abbott et al., 2016).

General Relativity (GR) extends the principles of Special Relativity to include gravity. Unlike Newtonian mechanics, GR does not conceptualize gravity as a force but rather as a curvature of spacetime. This concept is articulated through the equivalence principle, which posits that the effects of gravitational attraction are indistinguishable from the effects of acceleration. GR incorporates Lorentz invariance, foundational to Special Relativity, into its framework.

The flat spacetime in GR is mathematically represented using the Minkowski

spacetime metric, where the line element ds is given by:

$$ds^2 = \eta_{\mu\nu} dx^\mu dx^\nu = c^2 dt^2 - (dx^2 + dy^2 + dz^2) \tag{1.15}$$

$$= c^2 dt^2 - dr^2 - r^2 d\theta^2 - r^2 \sin^2(\theta) d\phi^2 \tag{1.16}$$

where (x, y, z) and (r, θ, ϕ) represent Cartesian and spherical coordinates, respectively. This describes spacetime without any curvature due to mass or energy. Therefore, Minkowski metric describes spacetime only in regions where gravitational effects are negligible.

The core of General Relativity is encapsulated in the Einstein field equations:

$$G_{\mu\nu} = \frac{8\pi G}{c^4} T_{\mu\nu} - \Lambda g_{\mu\nu}, \tag{1.17}$$

where $G_{\mu\nu}$ denotes the Einstein tensor that describes spacetime curvature, $T_{\mu\nu}$ represents the energy-momentum tensor that accounts for mass-energy distribution, Λ is the cosmological constant, and $g_{\mu\nu}$ is the metric tensor of spacetime.

These equations suggest that the fabric of the universe is dynamically shaped by its matter-energy content. This could be summarized by John Archibald Wheeler's famous aphorism: "Spacetime tells matter how to move; matter tells spacetime how to curve." This interdependence indicates that the universe's geometry and its temporal evolution are directly influenced by the distribution and properties of matter and energy within it.

The original cosmological constant (Λ) was initially proposed to allow for a static universe since Friedmann equations have no static solutions, but has gained modern relevance in explaining the accelerated expansion of the universe observed in contemporary cosmology as explained in next sections.

Despite its successes, it should be mentioned that General Relativity does not integrate well with quantum mechanics, and research is still ongoing into quantum gravity and theories like string theory that seek to unify gravity with other fundamental forces. The unresolved issues of dark energy and dark matter in contemporary cosmology further suggest that extensions to GR or entirely new theories might be necessary (Joyce et al., 2015).

In summary, General Relativity not only reshaped our understanding of gravity but also established the foundational framework for ongoing exploration of cosmology (Berti et al., 2015).

At this point, it should be explained that Einstein initially hypothesized a 'Cosmological Constant' (Λ), symbolized by the Greek letter Lambda, to represent a universe whose density remains constant over time and space. His motivation was to model a static universe—neither expanding nor contracting. However, when later observations by Hubble revealed that the universe was actually expanding, Einstein allegedly dismissed his cosmological constant as the 'biggest blunder of his life'. Interestingly, Λ can also take other values that imply an expanding and even an accelerating universe, as current observations suggest.

The concept of Λ can be extended to represent 'Dark Energy', a term used to describe the mysterious force driving the universe's accelerated expansion. One of the primary goals of surveys like DES (Dark Energy Survey Collaboration, 2016), DESI (DESI Collaboration et al., 2016b), and Euclid (Laureijs et al., 2011) is to measure the dark energy equation of state, w—the ratio of pressure to density—along with other key cosmological parameters, with a high level of precision. A value of $w = -1$ would indicate that the universe's dark energy density remains constant at any cosmic time, introducing the concept of negative pressure. However, dark energy theories permit w to vary, including over time. This parametrization of w is commonly referred to as the Chevallier-Linder-Polarski (CPL) parametrization (Chevallier & Polarski, 2001, Linder, 2003), which models w as a linear function of the scale factor, a, in the form:

$$w = w_0 + (1 - a)w_a \tag{1.18}$$

where w_0 and w_a are constants. Particularly, for $w_0 = -1$ and $w_a = 0$, the equation simplifies to $w = -1$, which corresponds to a cosmological constant. Furthermore, Equation 1.18 is a robust parametrization but the use of high-order polynomials is problematic. More interestingly, due to the nature of observations for $z \lesssim 1.5$ that lack sufficient accuracy to detect time variations in w, they effectively measure an

averaged w or an equivalent constant w. This is called "The Mirage of w". These topics have been thoroughly explored in Linder (2007). It is also important to note that the DESI Y1 analysis results, for the first time, show a clear preference for the $w_0 - w_a$ evolving dark energy model over ΛCDM. This finding suggests that dark energy might be dynamic rather than a cosmological constant.

1.1.4 Overview of ΛCDM

As discussed in the previous subsections, the ΛCDM model has provided a coherent cosmological framework that aligns with numerous observational tests. Below, Figure 1.2 illustrates the key cosmic events as depicted by the ΛCDM model.

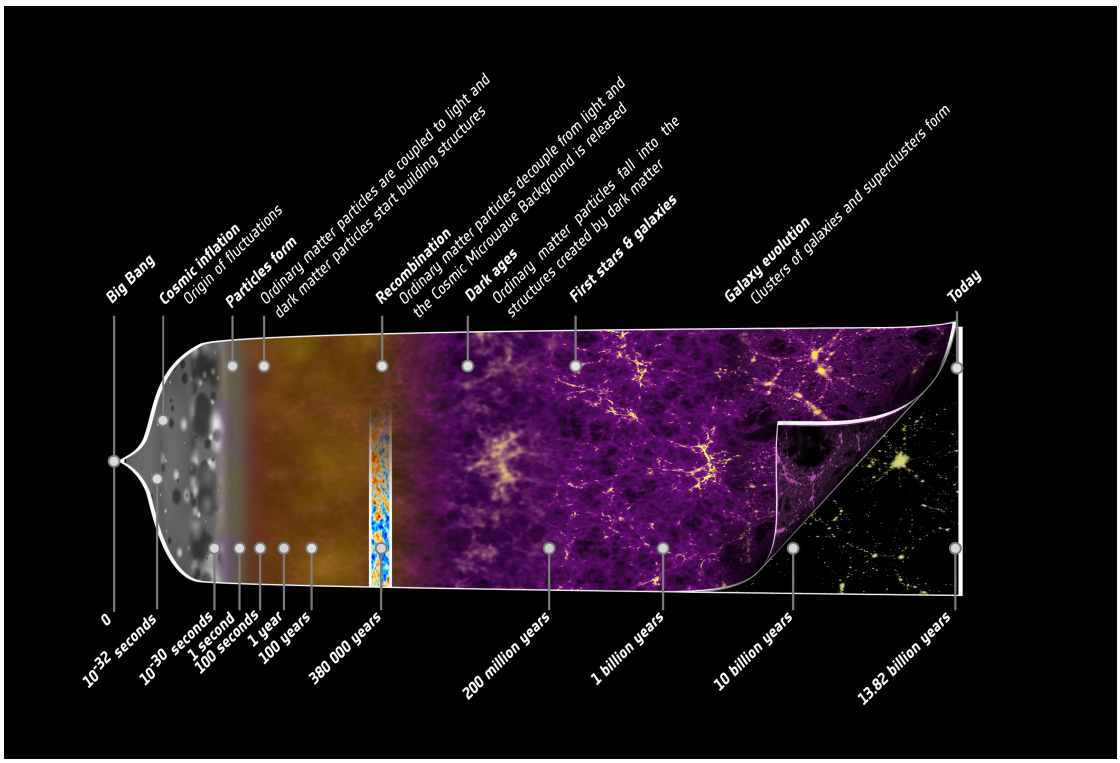

Figure 1.2: Graphical representation of cosmic events across time according to consensus ΛCDM model. Copyright: ESA - C. Carreau

Perhaps one of the most important moments in the history of modern cosmology, and the compelling evidence that led to the concept of "dark energy," emerged in 1998 through the seminal works of Riess et al. (1998) and Perlmutter et al. (1999). Independently, these two groups discovered that the universe is accelerating by observing Type Ia supernovae, which serve as standardizable candles, using

different surveys. This discovery led to the widespread acceptance of dark energy, conceptualized as vacuum energy, within the scientific community. Figure 1.3 illustrates the relationship between supernovae magnitude (distance) and redshift for the Supernova Cosmology Project.

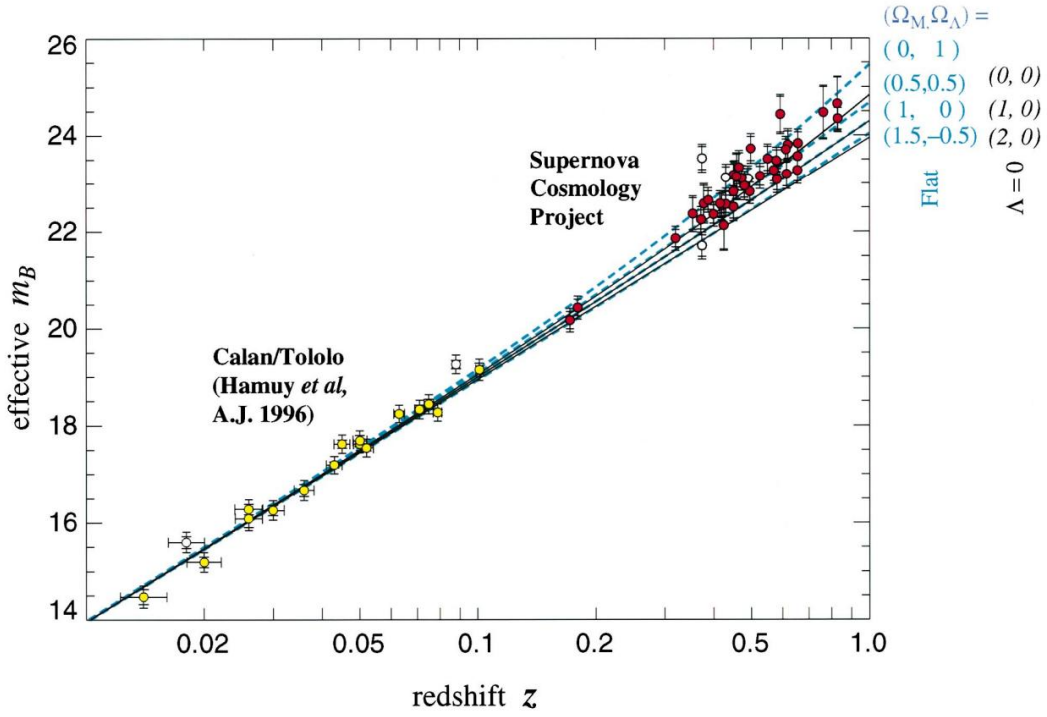

Figure 1.3: Pioneering diagram from Perlmutter et al. (1999) showing the magnitude of Type Ia Supernovae versus their redshift. The best-fit data to high redshift Supernovae indicates that these supernovae are dimmer than expected in consistency with Λ, providing striking evidence for the accelerated expansion of the universe.

Under the assumption of the standard ΛCDM cosmological model, the CMB measurements from the Planck satellite predict a current expansion rate of 67.4 ± 0.5 km s^{-1} Mpc^{-1} (i.e., with better than 1% precision) (Planck Collaboration, 2020)). Consistent results are also obtained from the Atacama Cosmology Telescope (ACT, e.g., Madhavacheril et al. (2024)), and from the South Pole Telescope (SPT, e.g., Balkenhol et al. (2023)).

Furthermore, these predictions of H_0 are also in good agreement with other early Universe results without using any CMB data. It is important to emphasize the word "prediction" here because all of these early measurements predict the current expansion rate H_0 by using 6 parameter standard ΛCDM model.

For instance, BAO data, when combined with the Big Bang Nucleosynthesis (BBN) information using the physical baryon density parameter $\Omega_b h^2$ (Burles & Tytler, 1998, Cooke et al., 2018, Schöneberg et al., 2019), can determine the Hubble constant H_0 by assuming the ΛCDM model. Alternatively, H_0 can be estimated independently of the sound horizon by using the horizon scale at matter-radiation equality, $k_{\rm eq}$ as explored in Philcox et al. (2022). Furthermore, the application of the inverse distance ladder method, which integrates observations from Type Ia supernovae (SN1a) and BAO, has also obtained results consistent with these approaches (Macaulay et al., 2019). These results show the robustness of early Universe methods in determining the value of H_0. In conclusion, all of these early Universe predictions agree well with each other regardless of CMB or sound horizon involvement.

However, the early Universe predictions of H_0 are challenged by the SH0ES collaboration, which employs the local distance ladder with Cepheid calibration of local Type Ia supernovae (Riess et al., 2021, 2019, 2022). They report a value of $H_0 = 73.04 \pm 1.04$ km/s/Mpc, indicating a $4-5\sigma$ tension with other measurements. This so-called 'Hubble Tension' is currently the subject of intense ongoing debate in both theoretical and observational cosmology with no consensus justification (Di Valentino et al., 2021, Khalife et al., 2024, Verde et al., 2023).

1.2 Large Scale Structure

1.2.1 Inflation and Structure Formation

In the very early stages of the universe after the Big Bang, it was extremely hot and filled with a dense plasma. During this time, cosmic inflation caused rapid expansion, leading to a spatially flat geometry on large scales (Liddle & Lyth, 2000). This is called Hot Big Bang and this primordial plasma featured minor irregularities that, driven by gravity, expanded to initiate structural development. The beginnings of this ancient period and the initial conditions for the universe's cosmological history remain subjects of intense ongoing investigation (Vagnozzi & Loeb, 2022).

However, the theory of inflation first proposed by Alan Guth in 1981 (Guth, 1981) offers a solution to two of the biggest problems: the horizon problem and the flatness problem. These are explained in detail below.

The horizon problem arises from the observation that regions of the universe that are far apart have very similar temperatures and other physical properties, despite the fact that they lie outside each other's cosmological horizons due to finite speed of light and therefore should not have been able to exchange information or energy.

The flatness problem is related to the precise balance required in the early universe between the density of the universe and its expansion rate. According to the standard Big Bang model, the density of the universe must have been very close to the critical density to result in the flat universe we observe today. Small deviations from this balance in the early universe would have led to a much different universe, either collapsing back on itself or expanding too rapidly for galaxies to form.

The inflationary paradigm states that the vacuum energy density of the early universe, vastly exceeding present-day levels, governed the Hubble expansion, inducing an exponential increase in the scale factor $a(t) = C \exp\left(\frac{\Lambda}{3}t\right)$.

The expansion therefore can smooth out any initial curvature, resulting in a flat universe, which aligns with current observations.

Moreover, inflation also predicts quantum fluctuations in the early Universe, due to deviations from the vacuum state. These quantum-induced fluctuations essentially cause primordial density perturbations, which are Gaussian in nature. Even before the development of inflationary theory, these primordial perturbations were regarded as likely precursors to the formation of large-scale structures (Liddle & Lyth, 2000, Peebles, 1980).

For this reason, its capacity to forecast a flat universe and offer a structure for the origin of density fluctuations that led to the formation of cosmic structures cements its place in modern cosmological theory.

1.2.2 Gravitational Lensing and Galaxy Bias

One of the important predictions of General Relativity (GR) is that matter bends light, as light follows the geodesics of space-time. When light emitted by galaxies

passes through a mass overdensity, it is bent by the gravitational field of this mass overdensity. The extent of this bending is proportional to the mass of the intervening object.

As a result, the images of galaxies are distorted, and the galaxy may appear in a different location than it actually is. This distortion typically occurs due to a foreground massive cluster or another galaxy (i.e., galaxy-galaxy lensing). While it is difficult to detect this bending caused by less massive objects, it becomes an observable effect when induced by a massive cluster or another galaxy. In cosmology, the galaxies that cause the background galaxies' light to bend are referred to as lenses, and the galaxies whose light is bent are called source galaxies.

Figure 1.4 is an example image of galaxy-galaxy lensing, known as "Cosmic Horseshoe" where a massive Luminous Red Galaxy (LRG) lenses the background blue galaxy and the special alignment creates horseshoe-like image. We explain more about LRG galaxies in the next sections as `redMaGiC` tracers that we use in DES Y3 study are based on LRGs.

Galaxy Bias

It has long been understood that the spatial clustering of observable galaxies does not necessarily mirror the distribution of the universe's total matter. Instead, the galaxy density can be described as a function of the underlying dark matter density. This concept, known as galaxy 'bias,' reflects the relationship between the spatial distribution of galaxies and the underlying dark matter density field. The bias arises from the intricate physics of galaxy formation, which causes the spatial distribution of baryonic matter(i.e galaxies) to deviate from that of dark matter.

This idea was first proposed by Kaiser (1984) and the concept emerged as a solution to the discrepancy observed between the clustering scale lengths of galaxies and rich clusters, suggesting that both cannot be unbiased indicators of underlying total mass field. Furthermore, Kaiser (1984) demonstrated that large galaxy clusters exhibit a significant bias due to their rarity, forming primarily in the highest density regions of the mass distribution, which exceed a certain critical threshold.

One may postulate that the smoothed galaxy density contrast is dependent upon

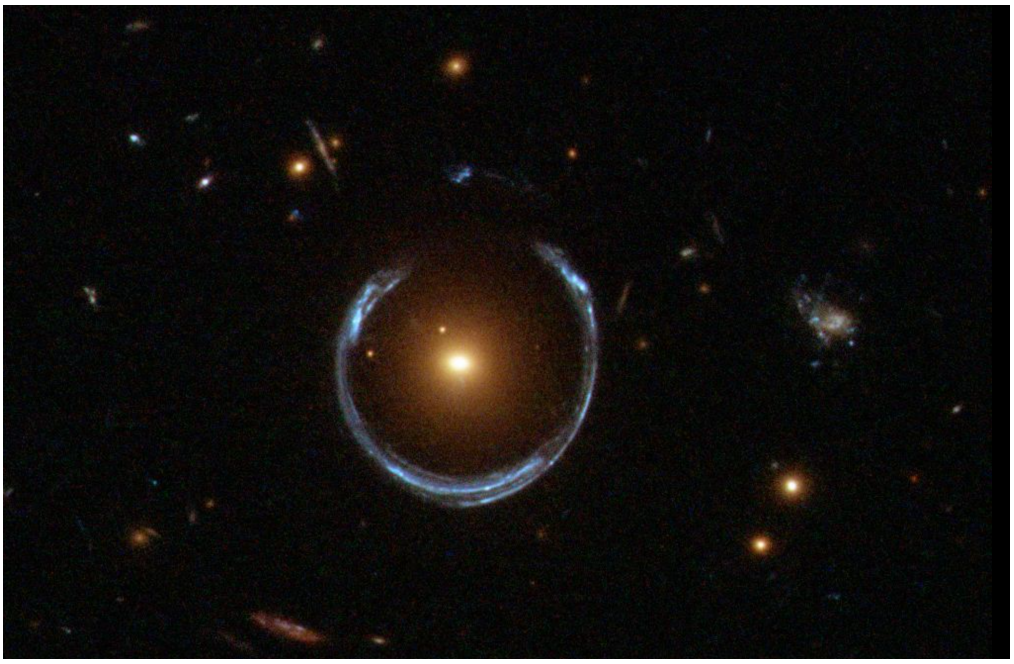

Figure 1.4: The foreground galaxy, LRG 3-757, is known for its exceptional mass, being a hundred times greater than the blue galaxy in the background. These galaxies are aligned in nearly perfect syzygy (line alignment), nearing the formation of an Einstein ring. Although galaxy-galaxy lensing is typically classified as weak lensing, this particular system serves as a perfect example of strong lensing. Copyright: ESA - Hubble

the underlying dark matter density contrast at a given scale:

$$\delta_g = f(\delta), \tag{1.19}$$

where $\delta \equiv (\rho/\bar{\rho}) - 1$, with $\bar{\rho}$ representing the average mass density at the specified scale. Under the assumption that $f(\delta)$ is a linear function of δ, the linear galaxy bias b can be described as the ratio of the average overdensity of galaxies and the average overdensity of the total mass.

$$b = \frac{\delta_g}{\delta}, \tag{1.20}$$

and this ratio can depend on scale and some other galaxy properties.

In modern cosmology, galaxy bias constitutes a fundamental concept. It is well-established that tracers and galaxy classifications possess distinct galaxy biases when mapping the distribution of dark matter (Tegmark et al., 2004, Zhao et al., 2024). This is especially important in cross-correlation studies of voids, which primarily aim to identify regions devoid of dark matter, therefore understanding galaxy bias in voids is an important area of research.

Analyzing the CMB lensing signal from voids provides insights into the underlying matter distribution from the shape of the convergence signal and therefore it can be compared with the theoretical predictions derived from the visible galaxy distribution using linear galaxy bias.

One of the studies that influenced the primary original work of this thesis Raghunathan et al. (2019) tested this assumption and found that the profile doesn't agree with the simple linear galaxy bias (Alam et al., 2017) explained above. Their findings are also in line with Nadathur & Percival (2019).

1.2.3 Dark Matter

The concept of dark matter emerged from astronomical observations that could not be explained by visible baryonic matter alone. In 1933, Fritz Zwicky published the first evidence for dark matter in the Coma galaxy cluster, utilizing the virial theorem

to infer the presence of unseen mass (Zwicky, 1933). Furthermore, Babcock (1939) observed the rotation curve of the Andromeda Nebula (M31) and found that much of its mass must be located at large radii, indicating a discrepancy with visible matter from stars.

In 1959, Kahn & Woltjer (1959) argued that the total mass of the Milky Way and Andromeda galaxies must be much larger than their stellar mass to explain why they are currently approaching each other. This suggested the existence of extended large dark matter halos enveloping galaxies.

Moreover, striking evidence was provided by Ostriker et al. (1974) and Einasto et al. (1974), who demonstrated that massive dark halos are necessary to account for the observed dynamics of galaxies and galaxy clusters (Ostriker & Peebles, 1973).

More importantly, Press & Schechter (1974) developed an analytic model for the growth of cosmic structures from a Gaussian initial density field, known as the Press-Schechter formalism. To test this model, they carried out N-body simulations, and this was the first time numerical experiments were used for the nonlinear structure formation in an expanding universe. In another landmark study, the mass profile of DM halos was shown to follow a simple profile (NFW profile) (Navarro et al., 1996). This is shown in Equation 1.21

$$\rho(r) = \frac{\rho_0}{\left(\frac{r}{r_s}\right)\left(1+\frac{r}{r_s}\right)^2} \tag{1.21}$$

where $\rho(r)$ represents the density at radius r, ρ_0 is the characteristic density scale that sets the overall density of the halo, and r_s is the scale radius marking the transition between the inner and outer regions of the halo based on the isothermal profile.

In addition, observations show that galaxies and clusters of galaxies gravitationally lens background sources as explained in Section 1.2.2. When these lensing effects are interpreted within the context of GR, the amount of lensing appears significantly amplified without assuming the existence of dark matter. The quantity and distribution of dark matter inferred are similar to those required to explain galactic rotation curves. In particular, sub-dark matter halos without any accompanying

galaxies have already been observed (Minor et al., 2021, Vegetti et al., 2010), in addition to some dwarf galaxies that are almost entirely dominated by dark matter (Simon et al., 2011). These observations further strengthen the evidence for invisible, gravitating dark matter halos.

However, although dark matter constitutes a significant portion of the Universe's mass, its fundamental particle nature remains one of the most compelling mysteries in modern physics. The leading candidates for dark matter particles are Weakly Interacting Massive Particles (WIMPs), which are hypothesized to interact via the weak nuclear force and gravity but not electromagnetically (Bertone et al., 2005, Jungman et al., 1996). WIMPs are currently the leading candidates for the particle nature of dark matter, as their potential annihilation processes are expected to produce gamma-ray signatures coming from the dynamical center of the Milky Way and this might have been detected by Fermi-Gamma-Ray Space Telescope (Daylan et al., 2016). Later on, some observations claimed that these excess signals can actually come from milisecond pulsars rather than dark matter annihilation (Gautam et al., 2022). More recently, some authors have investigated the potential of voids to host these annihilation signals in comparison to dark matter halos and have found that voids are very promising candidates, despite their low dark matter content due to their clean nature free from astrophysical sources (Arcari et al., 2022). A comprehensive review of the theoretical development of dark matter and current observational tests can be found in Frenk & White (2012).

On the other hand, some authors have explained the aforementioned galactic rotation curves using Modified Newtonian Dynamics (MOND) (Milgrom, 1983), which is a modification of gravity. Although MOND was initially not widely accepted and failed to explain large-scale phenomena such as the CMB acoustic peaks and relativistic effects like gravitational lensing, interest in the theory increased after Bekenstein (2004) expanded it with a relativistic extension. However, recent observations of binary stars strongly disfavor MOND (Banik et al., 2024). We explore more about modified gravity theories in Section 1.6.2.

In this thesis, we identify cosmic voids to probe regions devoid of dark matter (DM), since DM constitutes a much larger fraction of the total matter content than

baryonic matter and significantly contributes to gravitational lensing effects. We rely on galaxies and their bias relationship to trace the underlying dark matter distribution and to understand the properties of voids in the large-scale structure. Additionally, we cross correlate cosmic voids with the weak lensing mass maps constructed from Dark Energy Survey Y3 dataset in Chapter 3.

1.3 Cosmic Microwave Background (CMB) Radiation

As explained in Section 1.2.1, In the early Universe, the leading theory predicts that the Universe expands exponentially through a process called inflation (Albrecht & Steinhardt, 1982, Guth, 1981, Linde, 1982).

One of the most important discoveries in modern cosmology was the discovery of Cosmic Microwave Background (CMB) radiation. It was first predicted by George Gamow and his students in a series of papers that first appeared in 1948 (Alpher et al., 1948, Alpher & Herman, 1948b,a, 1949) based on the Friedmann equations and hot Big Bang theory. While many papers refer to Alpher et al. (1948) as the first prediction of a blackbody radiation filled within the Universe, the first calculation of the temperature of this radiation appeared in Alpher & Herman (1948b). For more details about the history of the prediction [see, e.g., Peebles (2014)].

Later on, the striking discovery of the CMB came from two radio astronomers Arno Penzias and Robert Wilson in the USA in 1965 (Penzias & Wilson, 1965).

The CMB is observed as an isotropic radiation filling the entire Universe, characterized by a black body spectrum at a temperature of $T_{\rm CMB} = 2.725\,{\rm K}$. The main driver of this was the cooling of the Universe to allow coupling of protons and electrons into forming neutral hydrogen atoms. This allowed photons to stream freely in the Universe.

The recombination process was not an instantaneous event, as it requires a non-negligible duration for the majority of protons and electrons to combine into neutral hydrogen. Nevertheless, when observed from today point, this period appears exceedingly brief relative to the vast distance to the last scattering surface.

One of the most important features of CMB radiation is that it exhibits small temperature fluctuations, which, under adiabatic conditions, also result in density perturbations given by:

$$\frac{\Delta T}{T} = \frac{\Delta \rho_m}{\rho_m} \approx 10^{-5}. \tag{1.22}$$

These minor fluctuations in the initial conditions are fundamental as they lead to the formation of the structures that constitute the cosmic web we observe today. The fluctuation amplitude at a redshift of approximately $z \sim 1100$ (around 400,000 years after inflation) is very tightly constrained by observations of the primary CMB temperature anisotropy power spectrum (Planck Collaboration et al., 2020b). In the following sections, we explain more on these anisotropies and their correlations, which are fundamental observables in modern cosmology.

1.3.1 Temperature Anisotropies

CMB radiation's temperature anisotropies at high redshifts, approximately $z \approx 1100$, provide a rich source of data from the epoch of recombination. This has been extensively studied by some missions such as the Planck satellite (Planck Collaboration et al., 2020b, Tauber et al., 2010), the South Pole Telescope (SPT) (Carlstrom et al., 2011, Ruhl et al., 2004), and the Atacama Cosmology Telescope (ACT) (Fowler et al., 2007).

Analysis of the peak positions and amplitudes in the CMB power spectrum facilitates the estimation of various cosmological parameters, as elaborated in Section 1.3.2

1.3.2 CMB Power Spectrum

The CMB fluctuations are assumed to follow a Gaussian distribution with variance given by the power spectrum $C_\ell = \left\langle \left| a_{\ell m}^{\mathrm{CMB}} \right|^2 \right\rangle$, where the CMB amplitude vector is now defined in terms of spherical harmonics. This represents the distribution of temperature fluctuations in the CMB across different angular scales on the sky.

These temperature fluctuations, observed as tiny variations in the CMB's uniformity, are characterized by multipole moments, denoted by the symbol ℓ. Each

multipole ℓ corresponds to an angular scale $\theta \approx 180^\circ/\ell$, with large ℓ values indicating small angular scales and vice versa. The power spectrum, C_ℓ, quantifies the amplitude of these temperature fluctuations at each multipole ℓ.

The most important feature of CMB temperature power spectrum is that peaks and dips in the power spectrum correspond to physical processes in the early universe, including acoustic oscillations of the photon-baryon fluid right before the recombination happened.

The first peak in the power spectrum reflects the largest acoustic oscillation scale, providing a measure of the universe's curvature, while subsequent peaks are sensitive to the baryon density, dark matter content, and other cosmological parameters (Nolta et al., 2004, Planck 2015 results. XVI., 2015). Figure 1.3.2 shows the temperature power spectrum of the CMB as observed by Planck satellite (Planck Collaboration et al., 2013).

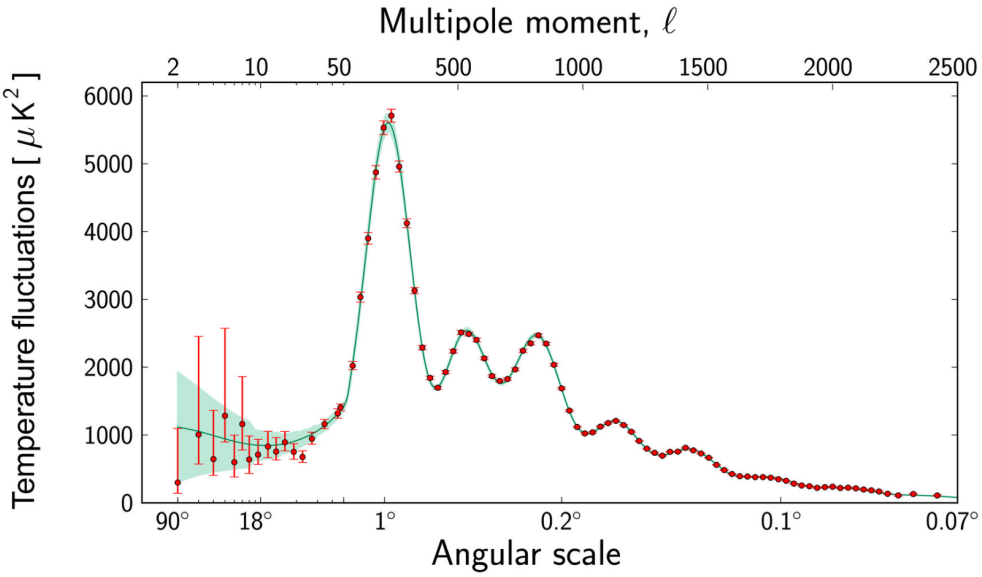

Figure 1.5: The Power Spectrum of the CMB temperature fluctuations as observed from Planck (Planck Collaboration et al., 2013), one of the fundamental observables in modern cosmology.

The precise measurement of the CMB power spectrum by experiments such as WMAP (Wilkinson Microwave Anisotropy Probe) (Dunkley et al., 2009a) and Planck has been instrumental in establishing the standard model of cosmology, known as ΛCDM (Lambda Cold Dark Matter), and in constraining key cosmolog-

ical parameters with unprecedented precision (e.g., Hinshaw et al. (2013), Planck Collaboration et al. (2020a)). These measurements have also provided insights into the early universe's inflationary period, dark energy, and the total matter-energy content of the cosmos.

The continued study of the CMB power spectrum remains a cornerstone of cosmological research, offering a unique window into the universe's history and composition.

1.3.3 CMB Lensing Convergence

As discussed in Section 1.2.2, a new approach in cosmic structure measurement involves using gravitational lensing to directly observe the matter distribution. Although strong gravitational lensing is valuable for examining individual distant objects and small regions of the sky in detail, weak lensing offers a promising method for mapping the large-scale distribution of matter. This can be achieved through weak lensing measurements, which use the distortions in galaxy shapes observed, a technique commonly known as cosmic shear (Kaiser, 1992, Kilbinger, 2015).

However, the CMB offers several key advantages over cosmic shear and other lensing probes of mass. This is because it serves as a single, well-localized source at a precisely determined redshift, and its underlying statistics are well understood, being nearly Gaussian. These features of the CMB make it relatively straightforward to reconstruct maps of the mass or gravitational potential that cause CMB lensing.

CMB lensing is sensitive to the influence of all matter fluctuations along the line of sight from the CMB last-scattering surface at $z \sim 1100$. However, it is most sensitive to matter between $0.5 \lesssim z \lesssim 3$ due to the geometry (Zaldarriaga & Seljak, 1999) with a peak around $z \approx 2$. Visualizing the redshift kernel of CMB lensing and comparing it with state-of-the-art galaxy surveys, especially Euclid (Laureijs et al., 2011) and LSST (Ivezić et al., 2019), can be interesting as shown in Figure 1.6. This broad and well-characterized redshift kernel as shown in Figure 1.6 makes CMB lensing an excellent tool for investigating phenomena such as massive neutrinos, which influence the shape of the matter power spectrum. Although CMB lensing maps do not provide direct information on the redshift dependence of

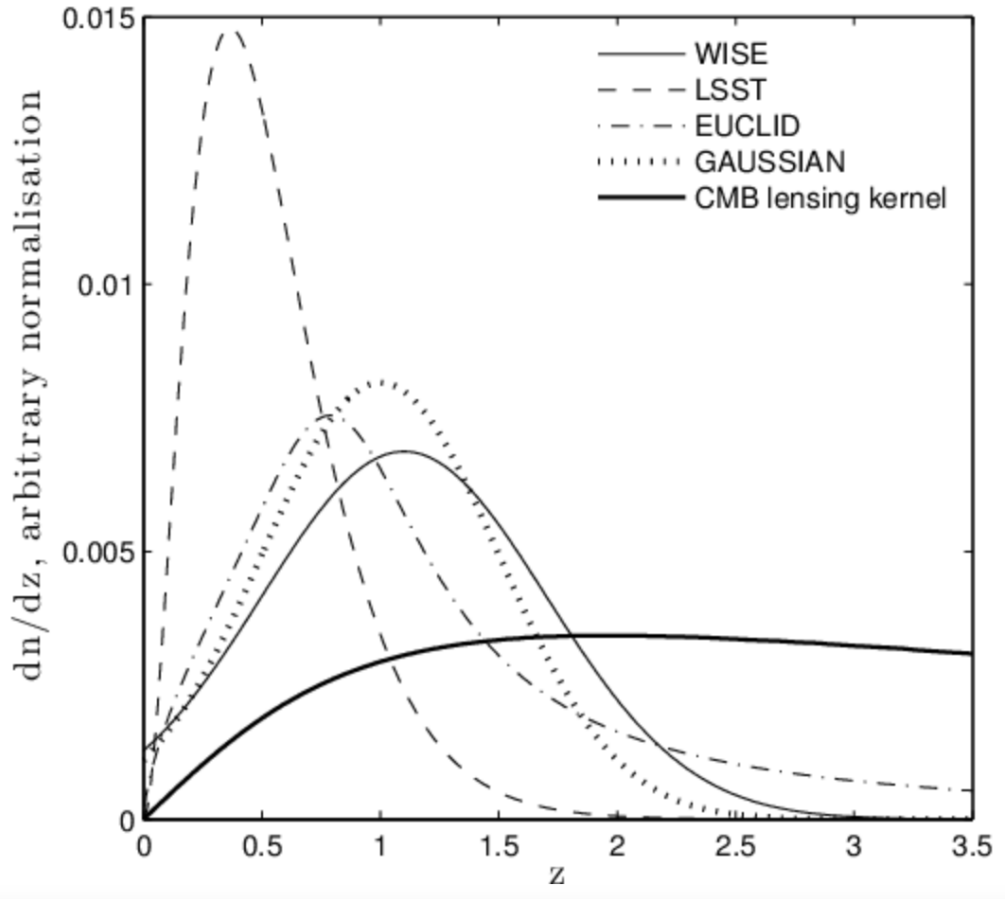

Figure 1.6: Comparison of the CMB lensing kernel with redshift distributions from upcoming galaxy surveys (Pearson & Zahn, 2014). The Gaussian model has $\mu = 1$, $\sigma = 0.5$.

cosmic growth, cross-correlating these maps with other large-scale structure tracers that include redshift information—particularly optical galaxy surveys—can give valuable constraints on dark energy and modified gravity as explored in DES data (Giannantonio et al., 2016, Kirk et al., 2016).

The optimal CMB lensing map for cross-correlation analyses would ideally exhibit a high signal-to-noise ratio (S/N) across all observed angular modes, extensive sky coverage, and substantial overlap with galaxy surveys. The Planck collaboration's lensing map, which achieves the maximum aggregate S/N of any CMB lensing measurement, encompasses nearly the entire sky. However, it exhibits a low S/N per mode, limited to scales smaller than several degrees (Planck Collaboration et al., 2020b). However, ground-based CMB observatories, including the South Pole Telescope (SPT) and the Atacama Cosmology Telescope (ACT), have been utilized to generate lensing maps with enhanced signal-to-noise ratios on smaller scales, albeit over significantly smaller fractions of the sky compared to Planck. See Das et al. (2011), van Engelen et al. (2012) and the recent results in Madhavacheril et al. (2024), Pan et al. (2023). It is also important to note that CMB lensing alone indicates the existence of dark energy with $w = -1$ as shown by Sherwin et al. (2011).

Here we show the Planck CMB lensing map in Figure 1.7.

Quadratic Estimators

To construct the convergence κ map from the CMB, it is useful to obtain both temperature and polarization maps. The seminal work on the quadratic estimator and its theoretical foundation is documented in Hu (2000). Subsequently, this framework was extended to incorporate polarization data by Hu & Okamoto (2002a) and Lewis & Challinor (2006).

The Planck CMB lensing analysis presented in this thesis (Planck Collaboration et al., 2020b) employs the lensing convergence estimates derived by Carron & Lewis (2017), which utilize a slightly modified version of the approach outlined by Okamoto & Hu (2003). This modification enhances the quadratic estimator's efficiency, enabling the rapid generation of minimum-variance (MV) estimators

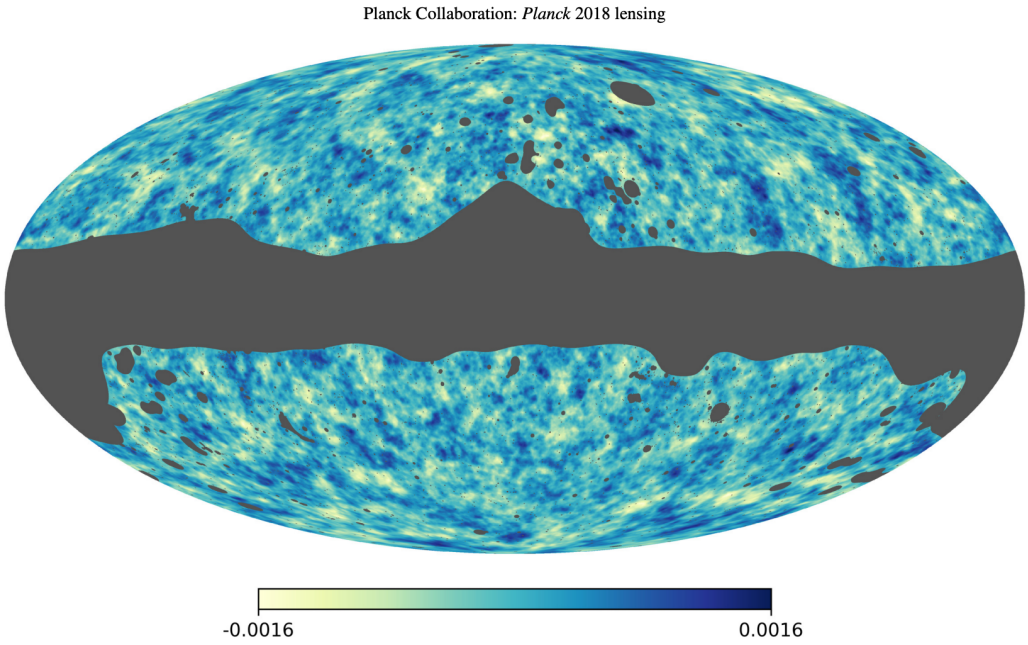

Figure 1.7: The image of constructed HEALPix convergence κ map from Planck Collaboration. The main data product used in Demirbozan et al. (2024) analysis.

directly from filtered maps. This methodology differs from the one used in the Planck Collaboration et al. (2016b) lensing map. While the specifics of these modifications are beyond the scope of this thesis, it is noteworthy that the work by Vielzeuf et al. (2021), to which I have made significant contributions, employs the Planck Collaboration et al. (2016b) lensing map while Demirbozan et al. (2024) uses the CMB lensing map produced by Planck Collaboration et al. (2020b).

A fixed large-scale lensing potential will lens smaller background unlensed CMB anisotropies in a characteristic way. By measuring a large number of these anisotropies it should therefore be possible to extract information about the lensing deflection field. The unlensed CMB field is, of course, unobservable, but its statistics are very well understood. Statistical measures of the lensed CMB fields should therefore be able to constrain the lensing potential. Here we concentrate on reconstruction from the CMB temperature and polarization, and assume the primordial fields are Gaussian and statistically isotropic. A visual representation of this is shown in Figure 1.8.

This lensing potential construction essentially amounts to using correlations between different scales of temperature anisotropies around each lensing mass to

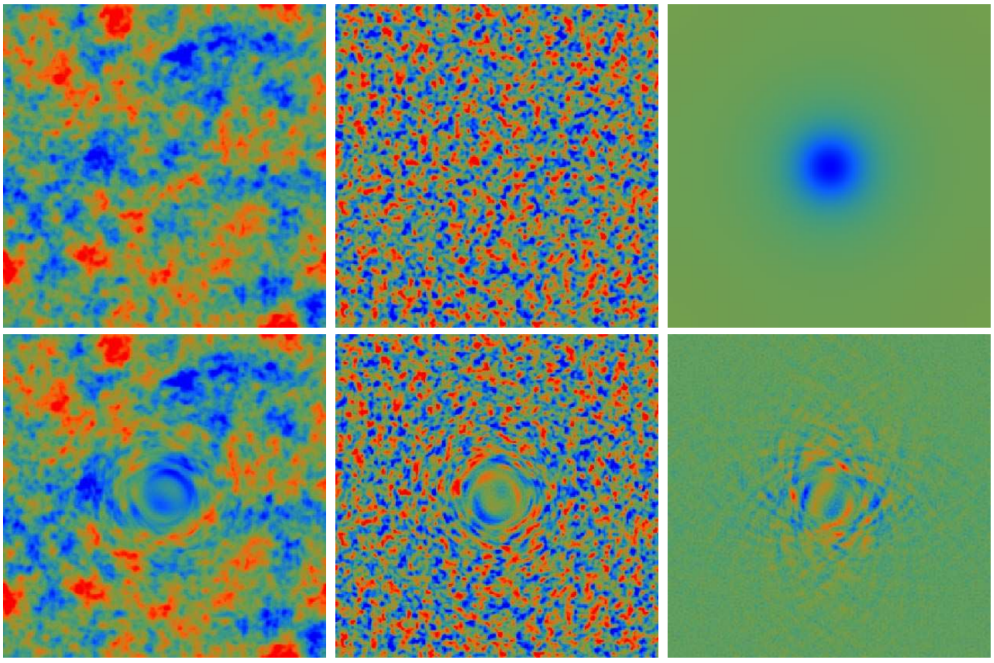

Figure 1.8: This figure taken from (Hu & Okamoto, 2002a) shows the impact of lensing on a 10° x 10° area shown in an exaggerated manner for illustration. At the top, from left to right, are shown: the temperature field before lensing, the E-polarization field before lensing, and a spherically symmetric deflection field. At the bottom, from left to right, the images depict: the temperature field after lensing, the E-polarization field after lensing, and the B-polarization field resulting from lensing. It should be noted that the scales used for the polarization and temperature fields are different by a factor of 10.

constrain the gravitational potential.

For example, diagonal elements of the unlensed CMB multipoles represent the variance of each mode with itself, essentially how much each mode fluctuates independently, while the off-diagonal elements indicate the covariance between different multipoles. This is shown in Equation 1.23, where for unlensed CMB, off-diagonal elements of the multipoles $(\ell, m) \neq (\ell', m')$, we get $\langle \tilde{X}_{\ell m} \tilde{X}^*_{\ell' m'} \rangle = 0$, implying no correaltion between different multipoles.

$$\langle \tilde{X}^{m*}_{l} \tilde{X}^{m'}_{l'} \rangle = \delta_{ll'} \delta_{mm'} \tilde{C}^{XX'}_{l} \tag{1.23}$$

In the context of CMB lensing, these off-diagonal elements can provide crucial information about how mass distributions along the line of sight might correlate different scales of the CMB sky.

Quadratic estimator operates by taking products of pairs of Fourier-transformed CMB temperature (T) and/or polarization (E and B modes) fields.

It is possible to express the lensed (observed) CMB temperature T in the $\hat{n}$ direction as a deviation (remapping) of the un-lensed (emitted) temperature $\tilde{T}$:

$$T(\hat{n}) = \tilde{T}(\hat{n} + \vec{\alpha}(\hat{n})), \tag{1.24}$$

where $\vec{\alpha}(\hat{n})$ is the deflection angle that is used to define a lensing potential ($\Phi(\hat{n})$) via

$$\vec{\alpha}(\hat{n}) = \vec{\nabla}\Phi(\hat{n})$$

(see e.g., Lewis & Challinor (2006), for details). Assuming a flat universe, the CMB lensing potential in a direction $\hat{n}$ is defined as:

$$\Phi(\hat{n}) = -2 \int_0^{x_{\rm cmb}} \frac{d\chi \, (x_{\rm cmb} - \chi)}{x_{\rm cmb} \chi} \Psi(\chi \hat{n}; t), \tag{1.25}$$

where χ is the co-moving distance ($x_{\rm cmb}$ is the co-moving distance to the CMB) and Ψ is the gravitational potential evaluated in the $\hat{n}$ direction and at time $t = \eta_0 - \eta$ where η_0 is the conformal time today. The gravitational potential can then be expressed as a function of the underlying matter density field through the Poisson

equation (see Equation 1.33 which we also explore in the next sections)

The lensing convergence κ, as a main observable, is defined as $\kappa = -\frac{1}{2}\nabla^2\Phi$, which in harmonic space can be related to the lensing potential as

$$\kappa_{LM} = \frac{1}{2}L(L+1)\Phi_{LM} \tag{1.26}$$

where L and M are indices of spherical harmonics of the reconstructed lensing maps. The Planck collaboration released the κ_{LM} coefficients (see Planck Collaboration et al. (2020b), Bartelmann & Schneider (2001) and Lewis & Challinor (2006), for details).

For this reason, large underdensities like voids—with positive gravitational potentials—have negative lensing potentials and imprint a negative convergence (κ) on their locations in the CMB. However, the effect from a single void is so weak that it can only be detected by stacking multiple void locations (i.e., few tens to thousands) on the CMB (Krause et al., 2013).

1.4 N-body Simulations

An N-body simulation is a computational technique used to model and study the dynamical evolution of a system of N particles under the influence of gravity. In modern cosmology, these particles often represent dark matter. The primary goal is to understand how structures in the universe form and evolve over time due to gravitational interactions. The simulation calculates the gravitational forces between all pairs of particles and updates their positions and velocities over discrete time steps. It is important to study complex, non-linear gravitational dynamics that are impossible to solve analytically as Cold Dark Matter (CDM) was widely accepted.

Perhaps one of the pioneering N-body simulations was `Millennium Simulation` produced by Springel et al. (2005). It used 10 billion particles and a 500 Gpc/h box.

Within the scope of this thesis, which is about the cross-correlation between cosmic superstructures and CMB observables, it is important to acknowledge the significance of N-body simulations as a calibration point for measured signals. For

example in Chapter 4, which is derived from Demirbozan et al. (2024), matched filter method is employed and this method heavily relies on simulation templates to construct the optimal filter. However, it is also important to acknowledge the limitations of these simulations. For example, when modeling non-linear effects, some stochastic elements are introduced to represent galaxy formation and cold dark matter framework is assumed. However, if dark matter has non-gravitational interactions and properties such as self-interaction or warmness. Baryonic physics in N-body simulations is often simplified, including aspects like gas dynamics, star formation, and feedback from supernovae or active galactic nuclei. These complexities can lead to deviations from the idealized ΛCDM predictions. Another point is that incorporating alternative cosmological models is challenging for N-body simulations, as they do not easily include new models. Examples of such models include those from string theory (Năstase, 2019), loop quantum gravity (Rovelli, 1998), and novel extensions of the cosmological model, such as Functors of Actions Theories (FAT) (Ntelis & Morris, 2023).

This consideration is essential for the robustness and potential limitations of the simulated voids, as well as their correlation with CMB observations in my research. Nonetheless, given that this thesis predominantly focuses on superstructures (primarily voids) on scales of a few tens of Mpc$/h$, small scale baryonic physics such as gas dynamics, AGN feedback and star formation are not expected to significantly impact the results presented herein. This assumption has also been tested by Schuster et al. (2024), who used both dark matter-only simulations and hydrodynamical simulations that include non-linear baryonic effects. They found good agreement between the two, implying that void studies are relatively free from complicated baryonic effects.

It should be noted that some N-body simulations, such as the Takahashi simulations (Takahashi et al., 2017) employed by Raghunathan et al. (2020), provide more than 100 realizations with the same cosmology. This large number of realizations increases the robustness of the results. However, these simulations include only dark matter (DM) halos without galaxies, and they need to be populated by galaxy tracers. Some previous DES studies (Kovács et al., 2022, Sánchez et al., 2016,

Vielzeuf et al., 2021) selected `redMaGiC` galaxies because of their low redshift errors. For consistency, we also rely on `redMaGiC` galaxies in our analysis, and since MICE has slightly higher resolution than the Takahashi simulation, it is better suited for resolving the halos that host LRGs (`redMaGiC`). Additionally, MICE has been specifically designed to match the properties of DES LRGs, making it an ideal choice for our study. Furthermore, since prior DES studies have used the MICE simulation, we have chosen to use it as well to maintain alignment with those studies (a more detailed explanation of the MICE simulation is provided in the next section). However, we acknowledge that a future study would significantly benefit from using over 100 realizations of Takahashi simulations. We also note that both Takahashi and MICE simulations use cosmological parameters that somewhat differ from those determined by the current Planck cosmology. The implications of these differences for our study are discussed in the following sections.

More recently, machine learning and simulation based inference techniques have been applied to cosmological simulations. One such example is `SIMBIG` simulation where authors use a subset of the Baryon Oscillation Spectroscopic Survey (BOSS) galaxy survey and determine cosmological parameters H_0 and S_8 with improved constraints (Hahn et al., 2024). The field is rapidly evolving and the importance of N-body simulations in modern cosmological research can't be overstated.

1.4.1 MICE N-body Simulation

The MICE (Marenostrum Institut de Ciències de l'Espai) simulation is a N-body simulation created to provide robust mock catalogue for large scale structure surveys. MICE was created using the Marenostrum supercomputer at the Barcelona Supercomputing Center (BSC)[1] by using the code GADGET-2 (Springel, 2005). The technical details of this simulation are given in Crocce et al. (2015), Fosalba et al. (2015).

The MICE simulation is particularly notable for its scale and depth, which includes 70 billion dark matter particles within a comoving volume of 3 Gpc/h, extending up to $z \approx 1.4$. This scale allows for the modeling of cosmic structures

[1] www.bsc.es

from the linear to highly non-linear regimes, making it a great tool to study voids.

Moreover, MICE simulation encompasses a volume 216 times greater than that of the Millenium simulation (Springel et al., 2005), although it contains a comparable number of particles. This larger volume, along with a corresponding increase in particle mass, makes the MICE simulation better suited for statistical analyses on very large scales. However, this advantage comes at the expense of resolution, limiting the ability to examine smaller scales and substructures within galaxy-sized dark matter halos. Since the scope of our study is voids, MICE simulation is a great choice for us.

It is important to note the cosmology used in MICE assumes a flat standard ΛCDM model derived from the five year survey of Wilkinson Microwave Anisotropy Probe (WMAP) (Dunkley et al., 2009b). More specifically, the input fiducial parameters used in MICE are: $\Omega_m = 0.25$, $\Omega_\Lambda = 0.75$, $\Omega_b = 0.044$, $n_s = 0.95$, $\sigma_8 = 0.8$, and $h = 0.7$. While the MICE simulation has been rigorously validated and extensively utilized in various analyses, it is particularly important to highlight the adopted value of $\Omega_m = 0.25$. This choice is somewhat lower than the best-fit value reported by the Planck 2018 results, where $\Omega_m = 0.315$ (Planck Collaboration, 2018). The discrepancy in the matter density parameter can influence the interpretation of the results, so it is important to give more details on this.

For instance, the variation in cosmological parameters such as Ω_m and the Hubble parameter H_0 could potentially alter the strength of the lensing signals we observe. Nevertheless, we operate under the assumption that shifts in Ω_m have an insubstantial effect on our measurements of the lensing signal. This supposition is supported by studies like those by Vielzeuf et al. (2021) and Kovács et al. (2022) which utilize the WebSky simulation (Stein et al., 2020) to demonstrate that changes in Ω_m have a minimal impact on the amplitude of the CMB lensing signal. This is also because it has been shown that the most important parameter affecting void density—and consequently their matter content and convergence (κ)—is the amplitude of matter fluctuations on scales of $8\,h^{-1}$ Mpc, known as σ_8 (Nadathur et al., 2019). Our analysis also includes a robust error analysis, specifically focusing on the uncertainties in the signal measurement of MICE templates, to confirm the

reliability of our results despite the potential variability in Ω_m.

In order to populate dark matter halos with galaxies, MICE uses the Friends of Friends (FoF) algorithm to define dark matter halos and then populates them with galaxies using the Halo Occupation Distribution (HOD) (Benson et al., 2000, Berlind & Weinberg, 2002, Jing et al., 1998, Peacock & Smith, 2000, Seljak, 2000).

For our purpose of creating a Dark Energy Survey Y3-like galaxy sample, we employ the methodology described in Ferrero et al. (2021) to create the Red-sequence Matched-filter Galaxy Catalogue `redMaGiC`, which is a catalog of photometrically selected luminous red galaxies (LRG) based on the red-sequence Matched-filter Probabilistic Percolation (redMaPPer) cluster finder algorithm, as described in Rozo et al. (2016). See Cawthon et al. (2018) for further technical details.

The galaxy selection criteria in the MICE simulation are carefully adjusted to replicate the observational characteristics of the DES Y3 `redMaGiC` sample. This is accomplished by fine-tuning the simulations to produce galaxy redshift distributions, clustering parameters, and color distributions that closely match those observed in the DES Y3 data.

In particular, to populate dark matter halos with galaxies using the HOD method which tells us how many galaxies each dark matter halo has on average, we need to make use of the halo mass profiles, the classification of central and satellite galaxies along with their positions, velocity profiles, and corresponding masses and luminosities. This requires two separate function to be written: one for central galaxies and one for satellite galaxies. Since our focus is on large scale information, following the methodology of Ferrero et al. (2021), Tinker et al. (2012), Zheng et al. (2007), central and satellite galaxies are placed and their velocities and luminosities are assigned in the following way:

The number of **central galaxies** in a dark matter halo of mass $M_{\rm halo}$ is given by:

$$N_{\rm cen} = f_{\rm cen}^{\rm max} \times \frac{1}{2}\left[1 + {\rm erf}\left(\frac{\log M_{\rm halo} - \log M_{\rm min}}{\sigma_{\log M}}\right)\right] \tag{1.27}$$

where:

- $f_{\rm cen}^{\rm max}$ is the maximum fraction of halos that can host a central galaxy.

- $M_{\rm halo}$ is the halo mass.
- $M_{\rm min}$ is the minimum halo mass required to host a central galaxy.
- $\sigma_{\log M}$ represents the scatter of the halo mass.

Equation 1.27 is modeled by the error function $\mathrm{erf}(x)$, where halos with masses much larger than $M_{\rm min}$ almost certainly host a central galaxy ($N_{\rm cen} \approx f_{\rm cen}^{\rm max}$), while those with much smaller masses are unlikely to host one.

For **satellite galaxies**, the number of satellites in a dark matter halo is proportional to a power of the halo mass:

$$N_{\rm sat} = N_{\rm cen} \left(\frac{M_{\rm halo}}{M_1} \right)^{\alpha} \tag{1.28}$$

where:

- $N_{\rm cen}$ ensures that satellite galaxies are only assigned to halos that host a central galaxy.
- M_1 is the characteristic halo mass where, on average, a halo hosts one satellite galaxy.
- α is the power-law slope controlling the increase in the number of satellite galaxies with halo mass.

All this process is repeated in very thin redshift cells and the parameters are calculated for each shell to match $n(z)$ between MICE and DES Y3. After the numbers of central and satellite galaxies are determined, positions and velocities to the satellite galaxies are assigned in the following way:

- **Positions**: Satellites are placed according to a triaxial NFW profile. Inputs include the halo's position, mass, and redshift, resulting in satellite coordinates (x, y, z).
- **Velocities**: Velocities are assigned using a Gaussian distribution based on the halo's velocity, mass, and redshift, yielding velocity components (V_x, V_y, V_z).

After this step, a luminosity selection is applied. To assign luminosities, halo abundance matching (HAM) techniques are used (Kravtsov et al., 2018):

$$\log(l_p) = \log(M_{\rm halo}) + \varphi_{\rm LM} \cdot G_{\mu=0,\sigma=1} \tag{1.29}$$

where G is standard Gaussian distribution and l_p is modeled in arbitrary scales. The luminosity scatter parameter ($\varphi_{\rm LM}$) here adjusted carefully to select the galaxies that match the observations, specifically the $n(z)$ distribution that match DES Y3 `redMaGiC` galaxies in our case. This technique facilitates matching the abundance and redshift distribution of DES Y3 `redMaGiC` galaxies with those in the MICE simulation by selecting the most luminous galaxies.

Consequently, the resulting MICE `redMaGiC` catalogue reproduces the $n(z)$ redshift distribution of the galaxies observed in the DES Y3 `redMaGiC` dataset. This match is very important as any mismatch here will result in very different void catalogues being produced and therefore can affect the final measurements.

At this point, it is also important to note that we use the updated version of `redMaGiC` called v0.5.1. This is a different approach than used in Kovács et al. (2022) and it is one of the main factors of the difference in results with respect to Demirbozan et al. (2024). The main changes are about the galaxy color/color covariance and more robust estimation of redshifts, resulting in a different redshift distibutions. Further details about the `redMaGiC` algorithm and corresponding plots can be found in Section 1.5.2.

MICE CMB Lensing Map

Both in Vielzeuf et al. (2021) and Demirbozan et al. (2024), we utilize the MICE CMB lensing map. This map is constructed using the "Onion Universe" technique, as detailed in Fosalba et al. (2008). This technique effectively simulates the tomographic structure of photometric surveys by segmenting the 3D lightcone into 2D all-sky maps with respect to the observer. This approach was among the pioneering methods for deriving CMB lensing maps from N-body simulations, paralleled by similar efforts in other studies (Carbone et al., 2009, Das & Bode, 2008). This

map is provided in HEALPix format with `Nside` = 2048, but since our analysis in both Vielzeuf et al. (2021) and Demirbozan et al. (2024) deals with degree-scale variations, this map is downgraded to `Nside` = 512 and both studies perform all the analysis with this resolution. Figure 1.9 shows this MICE CMB lensing map without any alteration.

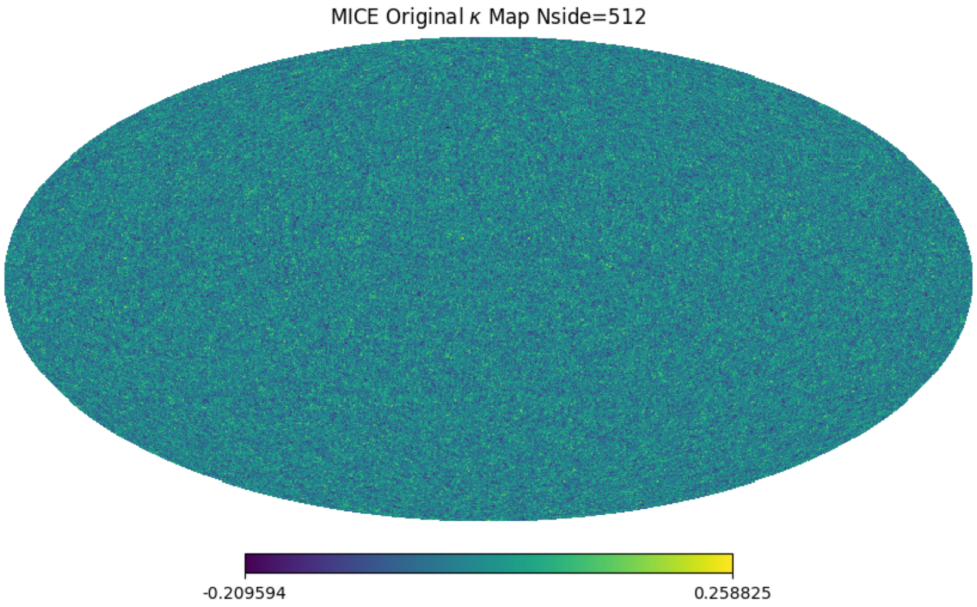

Figure 1.9: Original MICE CMB lensing map without any filtering or alteration shown in `Nside` = 512 in HEALPix format.

1.5 The Dark Energy Survey

1.5.1 Overview and Instrument

At lower redshifts ($z \lesssim 2$), as discussed in previous sections, testing cosmological models can be effectively conducted through studies of the universe's large-scale structure, gravitational history, and dynamics. Meeting the precision requirements necessary to complement CMB experiments necessitates the analysis of increasingly detailed and extensive catalogs of the large-scale structure. In pursuit of these objectives, the Dark Energy Survey was planned.

Initiated after years of meticulous planning and supported by a significant investment of approximately $100 million, the primary focus of the Dark Energy Survey

(DES) has been to probe dark matter and dark energy (Offer & Lahav, 2023). These components are crucial for understanding the mechanisms behind the universe's accelerating expansion. Apart from dark matter and dark energy, the objectives of DES include evaluating alternative gravitational theories through detailed investigations of large-scale cosmic structures, cluster counts, weak gravitational lensing, and Type Ia supernovae. The extensive dataset generated by DES can also be used to explore a broad range of other astrophysical phenomena (Dark Energy Survey Collaboration, 2016).

DES uses the 570-megapixel DECam, a sophisticated camera mounted on the 4-meter Blanco telescope at Cerro Telolo Inter-American Observatory (CTIO) in Chile. This advanced instrument's focal plane comprises 62 2K x 4K CCD modules, each with a resolution of 0.27"/pixel, configured in a hexagonal pattern to fit within the approximately 2.2-degree diameter field of view. Additionally, it includes 12 smaller 2K x 2K CCDs dedicated to guiding, focusing, and alignment (Honscheid & DePoy, 2008). This camera has been the key element in capturing detailed images across 5000 square degrees of the sky in five optical and near - infrared (grizY) bands, to measure the photometry of millions of galaxies. By its completion, DES has compiled an extensive catalog comprising over 200 million galaxies in the South Galactic Cap to 24th magnitude with photometric redshifts and 100 million stars (Pandey et al., 2022).

At the time of writing this thesis, DES has provided some remarkable contributions to cosmological constraints, including a precise 2.1% measurement of the Baryon Acoustic Oscillations (BAO) (DES Collaboration, 2024b). This measurement stands out as the most accurate angular BAO determination at any redshift obtained from photometric surveys, only to be surpassed by main DESI Y1 results.

Moreover, DES has executed in-depth cosmic shear analyses through weak gravitational lensing by accurately measuring and correlating the shapes of more than 100 million galaxies (Amon et al., 2022, Gatti et al., 2021, Secco et al., 2022) in addition to advanced galaxy clustering measurements (Porredon et al., 2022). Most notably, DES has integrated analyses of galaxy bias, weak lensing, and galaxy clustering to impose robust constraints on cosmological parameters (Abbott et al., 2022,

Pandey et al., 2022). This integration involves the combination of three two-point correlation functions (3×2pt): (i) cosmic shear using 100 million source galaxies, (ii) galaxy clustering, and (iii) the cross-correlation of source galaxy shear with lens galaxy positions, known as galaxy-galaxy lensing.

DES was also remarkably successful in combining its data with external CMB observations from SPT to obtain cosmological parameters with external tracers (Abbott et al., 2019, 2023) and more recently Bocquet et al. (2024). The Type Ia supernova (SN) observations of DES have imposed the tightest constrain on cosmology by any SN data set to date as of the writing of this thesis (DES Collaboration, 2024a, Vincenzi et al., 2024) as well as confirming cosmological time dilation (White et al., 2024) as predicted by GR. This time dilation is also confirmed using quasar variability (Lewis & Brewer, 2023). In the context of this research on cosmic voids and their interactions with the CMB lensing, DES provides an invaluable dataset.

1.5.2 Redshift Estimation and `redMaGiC` Tracers

Given that photometric redshifts are employed instead of spectroscopic redshifts, the resulting redshifts inherently contain uncertainties. It is well established that Luminous Red Galaxies (LRGs) exhibit lower redshift errors because of their distinctive position within the galaxy color-color space. Due to their significant luminosity, LRGs are detectable at considerable redshifts even with comparatively short exposure times. This feature of LRGs have been known from early data release of SDSS as reported in Stoughton et al. (2002).

As large-scale surveys such as the DES increasingly rely on photometric redshifts, Rozo et al. (2016) introduced a novel selection method for LRGs based on the earlier *redMaPPer* galaxy cluster finding algorithm (Rykoff et al., 2014) The *redMaPPer* algorithm integrates spectroscopic data of galaxy clusters with photometric observations to calibrate the red sequence of galaxies as a function of redshift. This calibration serves as a photometric base, which is then used to identify galaxies as "red" by determining whether this empirical base accurately describes the galaxy's observed colors.

Therefore, red-sequence Matched-filter Galaxy Catalog (`redMaGiC`) tracers, as

detailed by Rozo et al. (2016), aim to achieve a sample with minimized photometric redshift errors. Figure 1.10 demonstrates the effectiveness of `redMaGiC` tracers in approximating spectroscopic redshifts, particularly in comparison to CMASS galaxies (Ross et al., 2011). Due to their low photometric redshift errors, `redMaGiC` tracers have been employed in all DES void analyses. In particular, Sánchez et al. (2016) showed a strong correlation between the 2D voids defined by spectroscopic and photometric redshifts.

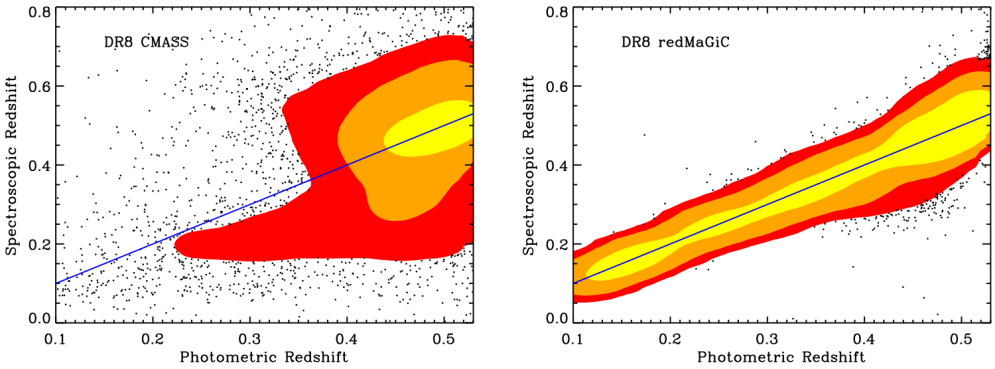

Figure 1.10: Comparison of photometric redshifts from `redMaGiC` tracers with spectroscopic redshifts as referenced in Rozo et al. (2016) Left: A graph comparing spectroscopic and photometric redshifts for CMASS galaxies using SDSS photometric data. The colored contours indicate regions containing 68%, 95%, and 99% of the data. A similar plot is shown for `redMaGiC` galaxies. The good agreement between spec-z and photo-z galaxies from `redMaGiC` galaxies is evident.

It is crucial to acknowledge that the `redMaGiC` algorithm has undergone multiple revisions, each with distinct versions. The application of these different versions within the MICE simulation framework has introduced challenges, leading to inaccuracies and unrealistic redshift distributions. In my primary study Demirbozan et al. (2024), we used the updated v0.5.1 `redMaGiC` version, which demonstrated a precise alignment with the expected redshift distribution, thereby mitigating these issues. This is the main reason for the difference with the results of Kovács et al. (2022), which will be discussed in the following chapters.

1.6 Cosmic Voids

From the inception of large-scale structure surveys, astronomers have observed that the distribution of galaxies in the Universe is not uniform, but instead forms complex structures including walls, filaments, clusters, and voids (Bond et al., 1996, Davis et al., 1985, Gregory & Thompson, 1978, Kirshner et al., 1981). These observations reveal that walls and filaments accumulate mass from the surrounding vast underdense voids, which constitute the majority of late time Universe's volume (Padilla et al., 2005, Platen et al., 2007). Since voids occupy most of the volume of the late-time Universe, their interiors are less prone to non-linear matter fluctuations. As a result, they are dominated by dark energy. Furthermore, neutrino mass fraction is high in void environments (Cai et al., 2015).

Therefore, voids can be used to constrain neutrino masses, as it has been shown that massive neutrinos at the linear level modify the matter-radiation equality time and the growth of matter perturbations, and therefore the evolution of voids (Lesgourgues et al., 2013, Lesgourgues & Pastor, 2006). It is assumed that voids would be smaller and less underdense in a massive neutrino universe (Massara et al., 2015). Kreisch et al. 2019 also showed that void statistical properties are significantly affected by neutrino masses, with the number of small voids increasing and the number of large voids decreasing as the neutrino mass increases. More recently Vielzeuf et al. (2023) claimed that void-CMB lensing cross-correlation is an important observable to probe neutrino mass and this is especially important as in this thesis, we explore the CMB lensing signal of voids. The void size function also depends on cosmological parameters after extensive calibration with simulations, as explored by Contarini et al. (2022) and Verza et al. (2019).

The consensus is that voids expand and get larger over cosmic time, with outflows emptying the matter inside (Baushev, 2021, Krause et al., 2013, Patiri et al., 2012, Paz et al., 2013, van de Weygaert et al., 2016). However, recently Vallés-Pérez et al. 2021 argued that voids can also accrete matter over time from neighboring filaments and clusters. They used hydrodynamical simulations and an elliptical definition of voids that are different from most conventional watershed voids.

In the consensus ΛCDM cosmological model, dark energy drives cosmic acceleration. Due to their low matter content, voids become dominated by dark energy at earlier times, making them highly sensitive to the nature of dark energy (Lee & Park, 2009, Pisani et al., 2015). For instance, the ellipticity of voids is sensitive to the dark energy equation of state (Bos et al., 2012). Therefore, they are one of the promising tools of the next decade of observational cosmology (Moresco et al., 2022).

In recent years, galaxies in voids have gained attention. In particular, Beygu et al. (2017) and Domínguez-Gómez et al. (2023) showed that void galaxies are generally smaller and less massive late-type systems with active yet slower star formation histories compared to those in denser environments. The low-density void environment primarily limits their stellar mass and size, resulting in distinct structural characteristics and evolutionary paths. This void environment fosters sustained but subdued growth, leading to galaxies that are predominantly star-forming, morphologically simpler, bluer and evolve more gradually than their counterparts in high density environments (Curtis et al., 2024).

Throughout this thesis, various void-finding algorithms are used to identify and analyze cosmic voids. Among these, some are based on the `ZOBOV` watershed algorithm (Neyrinck, 2008), such as `VIDE` (Sutter et al., 2015b). The REVOLVER algorithm (Nadathur et al., 2019) employs two distinct void-finding methods: one based on `ZOBOV`, and the other on a 3D particle-mesh grid approach called `Voxel` which are the primary void samples analyzed in my main study (Demirbozan et al., 2024). Additionally, we make use of a different void definition called "2D" which is defined on tomographic redshift slices (Sánchez et al., 2016).

Each of these void finders has been used in different aspects of void analysis within the DES Y3 dataset. In the corresponding chapter on DES Y3 results, we will provide a detailed explanation of these void finders, along with their respective results and figures. However, an overview of each method is provided here to establish a foundational understanding.

`VIDE` voids, in particular, have been extensively utilized in various DES void studies (Fang et al., 2019, Pollina et al., 2019, Vielzeuf et al., 2021). See Hamaus

et al. (2020) for a detailed analysis and references therein.

1.6.1 Void Finders Overview

In this section, I detail the group of void finders utilized throughout this thesis. A substantial part of my contributions to Chapter 2 (Vielzeuf et al., 2021) involves the use of `VIDE` voids. For Chapter 3, my focus primarily lies on 2D voids, while my main project Chapter 4 (Demirbozan et al., 2024) uses both `Voxel` voids and 2D voids. Although `VIDE` and `Voxel` voids play crucial roles in my research, ZOBOV emerges as the primary algorithm employed in both the REVOLVER and `VIDE` frameworks. Consequently, I will provide a detailed description of the ZOBOV algorithm, emphasizing its importance and application in the void finders utilized.

`ZOBOV` Void Finder

ZOBOV (ZOnes Bordering On Voidness) is an algorithm that identifies density depressions within a set of points without relying on any free parameters or shape assumptions. It is largely based on the earlier dark-matter-halo finder VOBOZ (VOronoi Bound Zones), which was nearly "parameter-free" (Neyrinck et al., 2005). ZOBOV is quite similar to earlier Watershed Void Finder (WVF) (Platen et al., 2007), as both algorithms use tessellation methods to measure densities and apply the 'watershed' concept, defining voids in a manner analogous to basins in a density field. However, while WVF has some advanced mathematical techniques to smooth the particle density before defining voids, ZOBOV directly analyzes raw, discrete tracer data.

ZOBOV uses the Voronoi Tessellation Field Estimator (VTFE) technique to reconstruct the tracer density field from a discrete tracer particle distribution. This method enables the identification of local minima within the field and the surrounding watershed basins, which collectively form a non-overlapping set of density depressions, or voids. Furthermore, the ZOBOV algorithm operates without any assumptions regarding the geometrical shapes of voids to be identified, thereby capturing the authentic topological characteristics of underdensities within the galactic

distribution.

The whole process can be briefly summarized in a following way:

1. **Density Estimation:** Calculate the density for each tracer galaxy using Voronoi tessellation, where the density at each point is inversely proportional to the volume of its Voronoi cell.

2. **Local Minima Identification:** Identify local minima (i.e largest Voronoi cell in the density field). These are points where the density is lower than at all adjacent Voronoi cells. We call these zones basins.

3. **Zones:** Use a watershed algorithm to expand zones from each local minimum by accreting neighboring Voronoi cells with increasing densities until reaching a saddle point or density ridge. Conceptually, this can be visualized as a flooding process where water fills up from the lowest points (the local minima) and begins to spill over into adjacent lower areas. Each cell that is filled becomes part of the zone.

4. **Saddle Point Evaluation:** Assess the significance of saddle points (density ridges) between zones. If a saddle point is not significantly high in density compared to adjacent zones, the zones are merged [See below].

5. **Merge Zones into Voids:** Combine zones into larger voids based on the significance testing of their connecting saddle points.

6. **Catalog Voids:** Finalize and catalog the identified voids, documenting their properties such as size and boundary definitions.

During this process, ZOBOV merges neighboring voids based on the watershed principle, creating a hierarchical structure of voids and subvoids. This process is illustrated in Figure 1.11. The resulting hierarchy and void size distribution are highly dependent on the input parameters controlling the merging process. For example, the merging process can result in the entire simulation box or Universe encompassed within a single large void. In contrast, if no merging occurs, initial

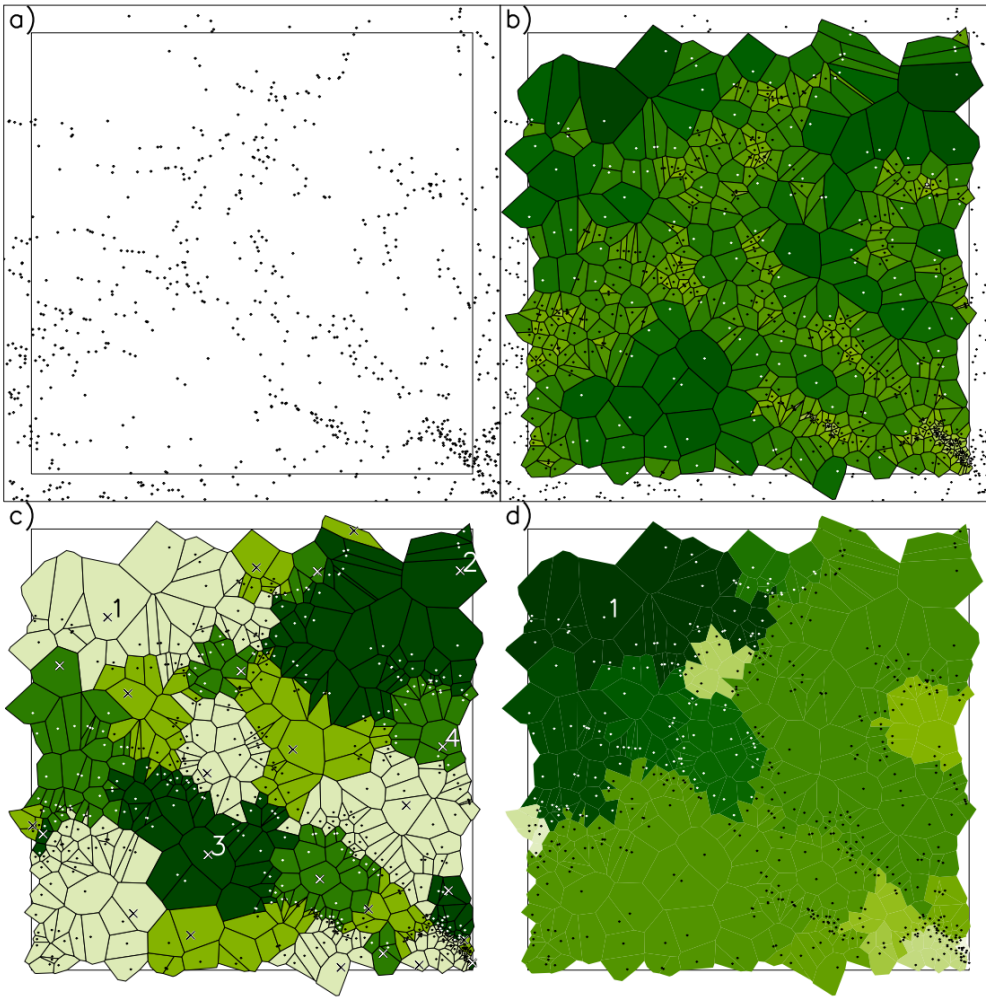

Figure 1.11: This figure illustrates a 2-D visualization of the ZOBOV algorithm as shown in Neyrinck (2008). The figure clearly summarizes the Voronoi tessellation process, wherein the largest Voronoi cell represents the density minima, and the adjacent zoning is distinctly observable. In real application, this is done in 3D.

voids are preserved. Hence, the criteria governing the merging process are of paramount significance.

However, the criteria for the regulation of void merging are, regrettably, inherently subjective, and various methodologies have been proposed within the existing body of literature. For instance, Neyrinck (2008) proposes utilizing the ratio of the lowest VTFE-reconstructed tracer number density at the void boundary to the minimum VTFE density at its core—compared to the analogous ratio for spurious voids in Poisson noise—as a criterion for delineating the 'most probable extent' of voids. Another approach involves halting void growth through merging when the minimum VTFE density along the watershed ridge separating it from a shallower potential subvoid ($n_{\rm link}$) exceeds a predefined threshold. The REVOLVER algorithm adopts the ZOBOV method for one of its void outputs; however, it does not perform any basin merging for either ZOBOV-based or `Voxel` based voids. In Chapter 4 of this thesis, we exclusively use `Voxel`-based voids produced by REVOLVER.

On the other hand, the `VIDE` void-finding toolkit (Sutter et al., 2015b) employs the ZOBOV algorithm and establishes this threshold at 0.2 times the average tracer density n. However, this selection of 0.2 is not strongly supported by theoretical reasoning. These issues are thoroughly investigated in Nadathur & Hotchkiss (2015b) and below we further discuss this point within `VIDE` algorithm.

Regarding the definition of the radius, ZOBOV offers an estimation known as the `effective spherical radius`. Despite the fact that voids have arbitrary shapes and typically deviate significantly from spherical symmetry, it is practical to characterize an effective spherical radius through the following equation:

$$R_v = \left(\frac{3V}{4\pi}\right)^{1/3} \tag{1.30}$$

Here, V denotes the total volume of the void, constituted by the cumulative volume of all individual Voronoi cells.

Regarding the determination of the void center, Neyrinck (2008) does not advocate a definitive approach. The prevailing method, supported by several authors (e.g Lavaux & Wandelt (2012), Nadathur & Hotchkiss (2014), Sutter et al. (2012, 2014)),

identifies the void center as the Voronoi volume-weighted mean of the positions of the mass tracers within the void. This approach emphasizes the influence of larger Voronoi cells, which correspond to regions of lower density, thereby enhancing the representativeness of the void center in reflecting underdense regions. However, it remains ambiguous whether this approach accurately identifies the region exhibiting the maximum deficit of mass.

This is because, due to the extremely low-density conditions within the interior of a void, the Voronoi cells often exhibit significant elongation. Consequently, the particles within these cells are typically positioned at considerable distances from their geometric centers. This spatial arrangement renders the particle position within each cell an inaccurate representation of the cell's actual location. Moreover, watershed voids encompass a substantial number of member particles, often several hundreds, with the majority situated within the denser walls and filaments outside the voids. The interplay of these factors results in the barycenter of the void being approximately symmetrically located relative to the dense void walls, yet markedly distant from the region of minimum density. For this reason, there is a more detailed discussion below about `VIDE`.

At this point, it is also important to mention that a principal outcome derived from the ZOBOV algorithm is the correlation between void size and the minima of void density as explored in Nadathur & Hotchkiss (2015a). This relationship can be accurately described as larger voids generally exhibit lower density minima. This is an inherent attribute of the ZOBOV algorithm, maintaining consistency irrespective of the tracers used for void identification, whether they are simulated dark matter particles, halos, or galaxies. Furthermore, this trait is expected to be a universal feature in all watershed void-finding algorithms. The primary conclusion from these observations is that the watershed voids do not represent a uniform population with consistent density contrasts across different sizes. This observation directly challenges the foundational assumptions of the theoretical model proposed by Sheth & van de Weygaert (2004)

Overall, the ZOBOV algorithm boasts paramount significance within large-scale structure studies and has profoundly influenced numerous subsequent void finders.

`VIDE` Algorithm

The `VIDE` toolkit, or Void IDentification and Examination toolkit, is an open-source Python/C++ code that primarily derives from the ZOBOV algorithm, as explained before. While `VIDE` also shares many similarities with the ZOBOV-based REVOLVER voids, there are notable differences. We illustrate an example of `VIDE` void in Figure 1.12.

One key distinction is the implementation of the watershed ridge merging threshold in `VIDE`, set to 0.2 times the average tracer density n. This threshold's dependency on the minimal number density of tracers along void boundaries presents challenges. Specifically, when applied to diverse galaxy tracer samples, such as QSO, ELG, or LRG, each with distinct biases, the same threshold value corresponds to significantly different dark matter (DM) densities. This variance results in disparate physical criteria for void merging across these tracer samples. Consequently, based on the results from Nadathur (2016), Nadathur & Hotchkiss (2015a,b), Nadathur et al. (2017), REVOLVER does not merge any zones and identifies each zone as a separate void. This approach applies to both ZOBOV-based REVOLVER voids and `Voxel` voids produced by the REVOLVER algorithm.

Another distinction is the definition of "void center". `VIDE` defines void center as barycentre (volume-weighted center) of all the Voronoi cells in the void in the following manner:

$$X_v = \frac{1}{\sum_i V_i} \sum_i X_i V_i, \tag{1.31}$$

where X_i and V_i are the positions and Voronoi volumes of each tracer particle i, respectively. However, Nadathur (2016), Nadathur & Hotchkiss (2015a), Nadathur & Percival (2019) showed that the definition of the void center is not actually very accurate to trace dark-matter halos. Conversely, REVOLVER defines the void center as the center of the maximal sphere that is entirely devoid of galaxies, which can be structured within the void, although REVOLVER also provides barycentre definition. These definitions of void centers have been extensively examined in (Nadathur & Percival, 2019), showing that the barycentre method diminishes the signal-to-noise ratio of redshift-space distortion (RSD) measurements. It should

be noted that maximal sphere fitting definition is the primary center definition of REVOLVER, and `Voxel` voids also use this definition. In this thesis, since we cross-correlate the identified void centers with CMB lensing, the definition of void center has substantial importance.

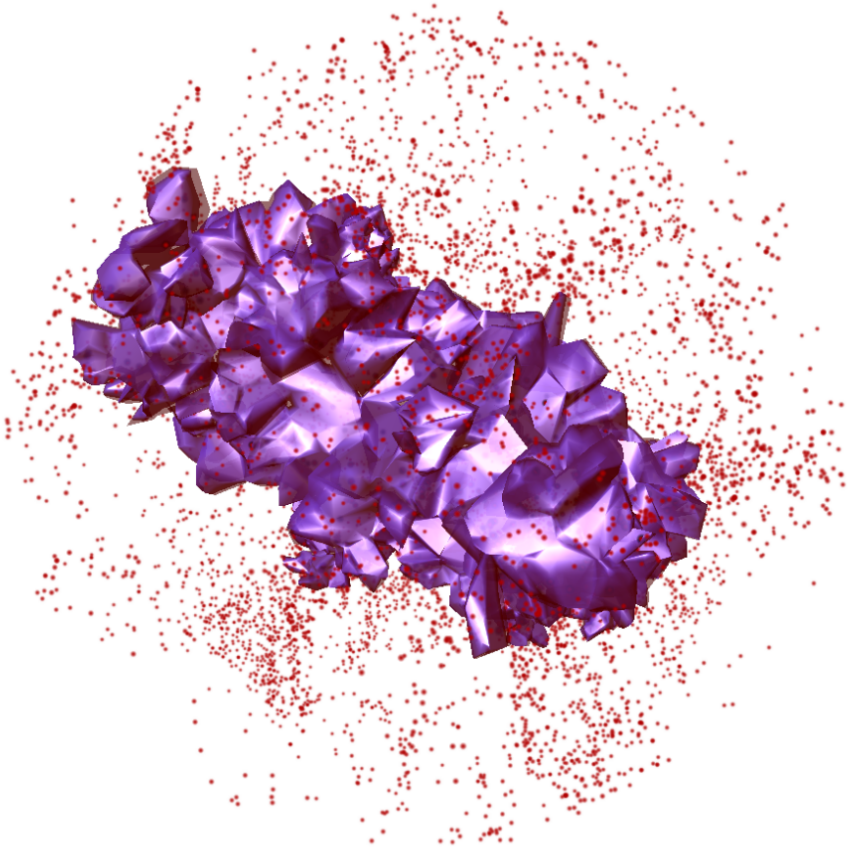

Figure 1.12: This figure from Sutter et al. (2015b) shows the underlying tracer density and purple void as found by the `VIDE` algorithm.

`Voxel` Algorithm

Most of my research, as described in Demirbozan et al. (2024), employs `Voxel` voids. The fundamental objective of the `Voxel` algorithm is to develop a void-finding mechanism capable of accommodating complex survey footprints characterized by irregular geometries and holes more efficiently than other 2D and ZOBOV-based algorithms. This is primarily because ZOBOV-based algorithms typically have to exclude a significant number of identified voids due to boundary contamination

issues.

Consequently, the `Voxel` algorithm employs a particle-mesh interpolation technique to ascertain the density field with enhanced accuracy. This methodology situates tracers within a three-dimensional grid comprised of cells (termed voxels), where the grid dimensionality is based upon the average number density of galaxy tracers, denoted as $\bar{n}$. Here, the side length of each voxel, $a_{\rm vox}$, is determined by the equation $a_{\rm vox} = 0.5 \left(\frac{4\pi\bar{n}}{3}\right)^{-1/3}$, with the density within each voxel being directly proportional to the count of tracers it contains. Subsequently, the density field is normalized using values obtained from the survey's random catalog, which incorporates the survey's window function and corrects for selection biases. This characteristic of `Voxel` voids distinguishes them from other detection algorithms by efficiently using the complex geometry of the survey data through this normalization process.

Furthermore, this interpolation is not only computationally straightforward, but also operates much faster than other density estimation methodologies, like `VIDE` and ZOBOV, scaling linearly with the number of tracers.

Upon estimating the density field, a Gaussian filter with a smoothing length $r_s = \bar{n}^{-1/3}$ is employed, identifying voids as loci of local minima within this refined density distribution. To determine the dimensions and boundaries of each void, a watershed algorithm iteratively incorporates adjacent voxels until a critical juncture is reached, where the density of the subsequent cell is inferior to that of the preceding one. This step is identical to the methodology in ZOBOV: contiguous voxels exhibiting increasing overdensity are assimilated into the basin, ceasing this process when the subsequent voxel exhibits a lower density than its predecessor. Each resultant basin is thus identified as a Voxel void.

The center of a `Voxel` void is intrinsically determined by the center of the voxel exhibiting the minimum density among all voxels within it. Given the localized nature of this center determination, it exhibits a enhanced sensitivity to minor perturbations in the density field. Nonetheless, such sensitivity appears to have negligible impact on the overall statistical characteristics of `Voxel` voids.

`Voxel` voids are also irregularly shaped voids similar to `VIDE`. Therefore, `Voxel` void radius is also calculated in the same way as in ZOBOV so that each identified

void is assigned an effective radius, R_v, calculated using the formula:

$$R_v = \left(\frac{3}{4\pi} N_{\rm vox} V_{\rm vox}\right)^{\frac{1}{3}},$$

where $N_{\rm vox}$ represents the number of voxels that constitute the void, and $V_{\rm vox}$ is the volume of an individual voxel.

While numerous investigations have employed `Voxel` voids, predominantly for void-galaxy cross-correlation analyses, their potential imprints on CMB lensing remain unexplored (Massara et al., 2022, Mauland et al., 2023, Radinović et al., 2024).

2D Algorithm

In this section, I will provide a brief overview of the 2D void finder algorithm, which has been used in Demirbozan et al. (2024), Jeffrey et al. (2021), Vielzeuf et al. (2021), where I have significant contributions. The main definition of 2D finders comes from Sánchez et al. (2016), which applied 2D void finding in DES-Science Verification (SV) data and measured weak lensing of galaxies around voids with 4.4σ significance. The 2D void finder operates on tomographic redshift slices by adopting a fixed comoving space value, typically set at 100Mpc/h. This selection aligns with the objective of Sánchez et al. (2016) to maintain the redshift slice thickness at twice the mean photometric redshift scatter 50Mpc/h of the `redMaGiC` galaxies used in that study. The findings of Sánchez et al. (2016) demonstrate that a minimum redshift slice thickness of 100Mpc/h is essential to ensure a satisfactory concordance between spectroscopic and photometric redshift voids in simulations. However, in practice one can increase this redshift thickness according to their optimal choices and the objectives of their study. As will be elaborated upon in subsequent chapters about the DESI Legacy Survey void project, it is noteworthy that the redshift slice thickness may indeed be considerably substantial, potentially extending from $z = 0.2$ to $z = 0.4$ or beyond.

After defining the tomographic slices, the whole slice is projected as a single bin to create the galaxy tracer density map. This is usually done with Healpix map

Nside=512 resolution and the density contrast map is created with respect to the mean density $\delta = \frac{n_{slice}}{\overline{n}_{slice}} - 1$ where $\overline{n}_{slice}$ is the mean density of the slice.

At this point, another void-finding parameter (the Gaussian smoothing scale) is applied to the tracer density contrast map to define density minima. To facilitate lensing analyses, it was shown in previous DES analyses that a σ = 10Mpc/h smoothing of the maps allows a robust detection of voids which carry most of the lensing signal. Therefore, a σ = 10Mpc/h was used as a galaxy density map smoothing parameter. However, Vielzeuf et al. (2021) used 20Mpc/h as well to test the effect of this smoothing scale. In general to identify larger voids this smoothing scale should be increased. As a note, we use 20Mpc/h in both Demirbozan et al. (2024) and Kovács et al. (2022).

After this step, a third parameter is the minimum central under-density of a pixel in smoothed density maps that is considered as a void centre. Voids with at least 30% under-density with respect to the n_{slice} in their centres were selected to ensure that too shallow and potentially spurious voids are excluded. It is also important to note that Hang et al. (2021) employs a slightly modified value in this context. By plotting the density contrast map and fitting a log-normal distribution, they select the least dense 10% or 5% of the identified potential void centres.

The void radius R_v is determined using an algorithm that incrementally increases the radius of annuli around void centers until the mean galaxy density n_{slice} is achieved. Figure 1.13 illustrates the identified voids using this method.

Furthermore, it is noteworthy that the size of 2D voids generally exceeds those of 3D voids (such as `VIDE` and `REVOLVER` voids), and their average lensing potential fluctuations are higher. This 2D algorithm identifies an astounding 10 times more voids compared to the REVOLVER algorithm when applied to the same tracers. In addition, the algorithm identifies structures that are elongated along the line of sight, rendering them particularly suitable for applications in gravitational lensing detection and Integrated Sachs-Wolfe (ISW) effect studies. It is particularly interesting to note that most of the excess ISW signal studies discussed in 1.7.2 use these 2D void types.

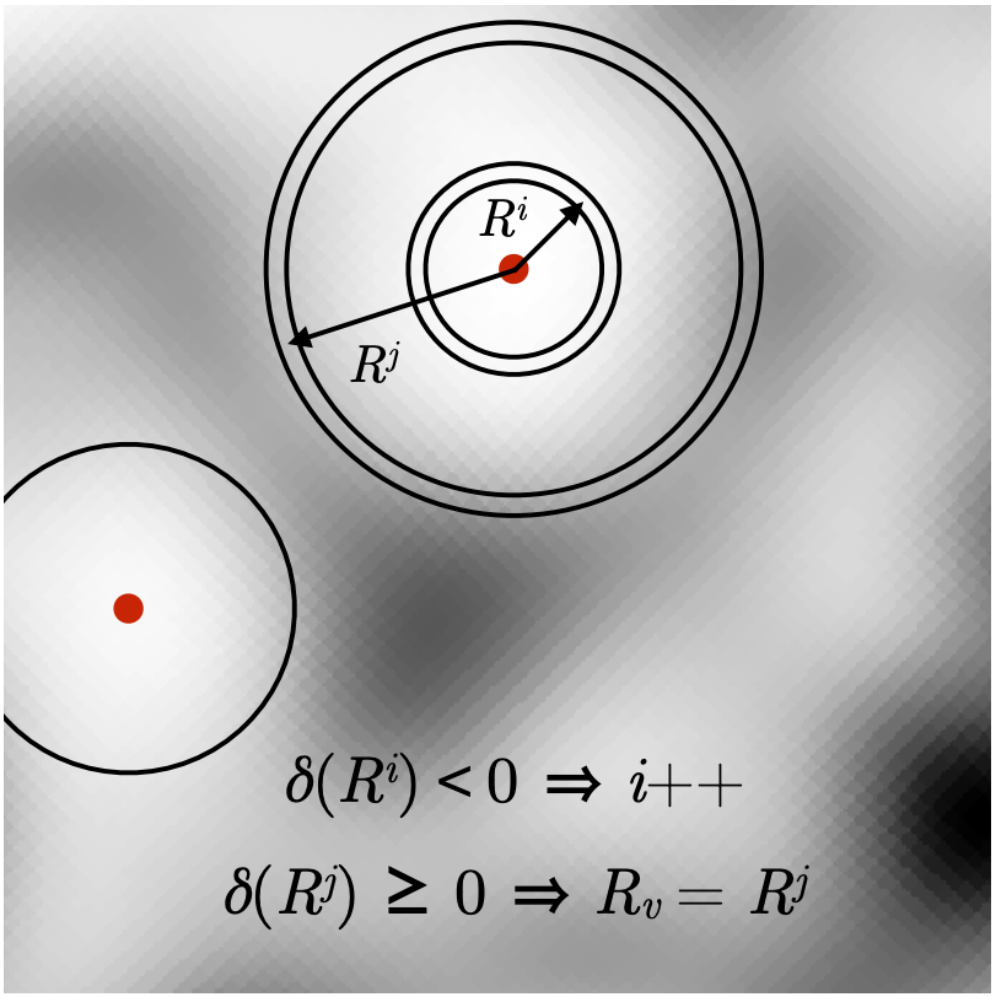

Figure 1.13: Visualization from Sánchez et al. (2016) shows the circular morphology of the detected voids. The background gray-scaled field represents the smoothed galaxy field within a redshift slice. The two solid (red) dots signify the locations of two void centers. For the upper void, a circular shell with radius R_i is shown. Given the density contrast $\delta(R_i) < 0$, the algorithm proceeds to evaluate progressively larger shells, extending to radius R_j where $\delta(R_j) > 0$. The void radius is consequently defined as $R_v = R_j$.

1.6.2 Modified Gravity and Voids

The concept of modifying Einstein's General Relativity arises from the need to explain dark matter and dark energy on cosmological scales and to resolve inconsistencies with quantum physics on quantum scales (Carlip, 2001, Clifton et al., 2012). This usually involves replacing Ricci scalar with $f(R)$ function in the Einstein-Hilbert action introducing an additional scalar field that acts as a fifth force. It is given by

$$S_{\mathrm{EH}} = \int \sqrt{-g}\left(\frac{1}{2\kappa}R + \mathcal{L}_m\right) d^4x,$$

where R is the Ricci scalar representing the curvature of spacetime, g is the determinant of the metric tensor $g_{\mu\nu}$, $\kappa = 8\pi G$ with G being the gravitational constant, and $\mathcal{L}_m$ denotes the matter Lagrangian density. In $f(R)$ gravity theories, this action is generalized by replacing the Ricci scalar R with an arbitrary function of R, leading to the modified action

$$S_{f(R)} = \int \sqrt{-g}\left(\frac{1}{2\kappa}f(R) + \mathcal{L}_m\right) d^4x.$$

This modification allows for more complex gravitational dynamics and is able to explain cosmic acceleration without dark energy. By choosing appropriate forms of $f(R)$, these theories can produce late-time accelerated expansion and offer alternative insights into the behavior of the universe on large scales. In literature, $f(R)$ theories of gravity dominates most of the attention of MG theories.

However, due to the precise agreement of GR with gravitational tests within the Solar System (Bertotti et al., 2003, Will, 2014), any alterations to GR must also align with these established results. Consequently, modifications like the fifth force must be effectively suppressed within the Solar System or smaller scales. One method to achieve this suppression is through screening mechanisms that render the fifth force significant primarily in underdense environments (Brax, 2013, Paillas et al., 2019).

Therefore, one of the potential regions in the Universe where deviation from GR can be observed is actually cosmic voids with their very low matter content. This is because these large underdense regions diminish the effectiveness of screening

mechanisms. In high-density environments, screening mechanisms, such as the Vainshtein mechanism (Vainshtein, 1972) or Chameleon mechanism (Brax, 2013, Khoury & Weltman, 2004), erase the signatures of Modified Gravity (MG) theories and align observations with GR predictions. However, in the low-density environments of voids, these mechanisms are less effective, allowing MG signatures to persist. Consequently, voids may exhibit deviations from GR with greater clarity compared to more densely populated areas of the universe (Davies et al., 2019). Furthermore, the shape and distribution of voids can vary under different gravitational theories. For instance, the Hu–Sawicki f(R) model (Hu & Sawicki, 2007) (screened by Chameleon mechanism (Khoury & Weltman, 2004)) of MG predicts that void walls are higher compared to those predicted by GR, providing a method to distinguish between these theories based on observational data of voids' structural features (Cai et al., 2015, Clifton et al., 2012, Hamaus et al., 2016, Perico et al., 2019).

Another notable example of a model using a screened fifth force is the normal branch of the Dvali-Gabadadze-Porrati (nDGP) braneworld scenarios (Dvali et al., 2000) with extra-dimensional gravity. Within the nDGP model, the fifth force is screened via Vainshtein screening (Vainshtein, 1972), which is less effective in areas distant from strong gravitational potentials, such as voids. Therefore, the most observable impacts of the fifth force are expected to be most pronounced in cosmic voids.

For example, voids in nDGP model and general modified gravity models are more under-dense as compared to ΛCDM voids due to the action of the fifth force that arises in these models, which leads to a faster evacuation of matter from voids (Cautun et al., 2018, Paillas et al., 2019).

This feature of nDGP and modified gravity models can be observed through the weak lensing of voids. This makes voids particularly good candidates for observing the effects of MG theories, which predict different lensing effects than GR (Braden et al., 2021, Voivodic et al., 2016, Wen et al., 2024). For example, CMB lensing signal of voids would be stronger than usual in the case of nDGP voids due to a more underdense environment of these voids, whereas a massive neutrino cosmology

would cause denser voids and their CMB lensing imprint would be weaker than expected (Vielzeuf et al., 2023). This is because voids are sensitive to neutrino mass fraction due to their underdense nature (Baker et al., 2018, Clampitt et al., 2013).

Another interesting feature of f(R) models, as discussed in De Felice & Tsujikawa (2010), is their prediction of a different strength of the ISW effect compared to the standard ΛCDM model. In particular, the evolution of the effective gravitational potential Φ_{eff} differs during the accelerated epoch, thereby providing a means to test the viability of f(R) gravity models as alternatives to ΛCDM model.

1.7 Tensions of ΛCDM and the Excess ISW Measurement from Voids

1.7.1 Integrated Sachs-Wolfe Effect

As discussed in Section 1.3, the CMB contains profound cosmological insights, primarily from its primary anisotropies. However, the CMB also offers valuable information from secondary anisotropies, which develop as CMB photons travel from the last scattering surface to their detection on Earth. Unlike CMB lensing, the integrated Sachs-Wolfe effect (ISW) results from the energy change of photons as they pass through evolving gravitational potentials during their extensive journey and was first proposed by Sachs & Wolfe (1967). Although this thesis has focused on CMB lensing, the techniques and methods used here are also effective for detecting the Integrated Sachs-Wolfe effect (ISW). Thus, a discussion of the ISW effect is provided.

As CMB photons traverse an overdense region in a universe undergoing accelerated expansion, the energy they gain while entering the potential well of the region is not fully compensated by the energy they lose upon exiting the now shallower potential of the region. This results in overdense regions appearing as hot spots in the CMB. Conversely, underdense regions, or voids, appear as cold spots because the photon loses more energy climbing out of the potential hill than it gains descending into it. Therefore, it is sensitive to time-derivative of the gravitational potential.

This is illustrated in Figure 1.14 and Figure 1.15.

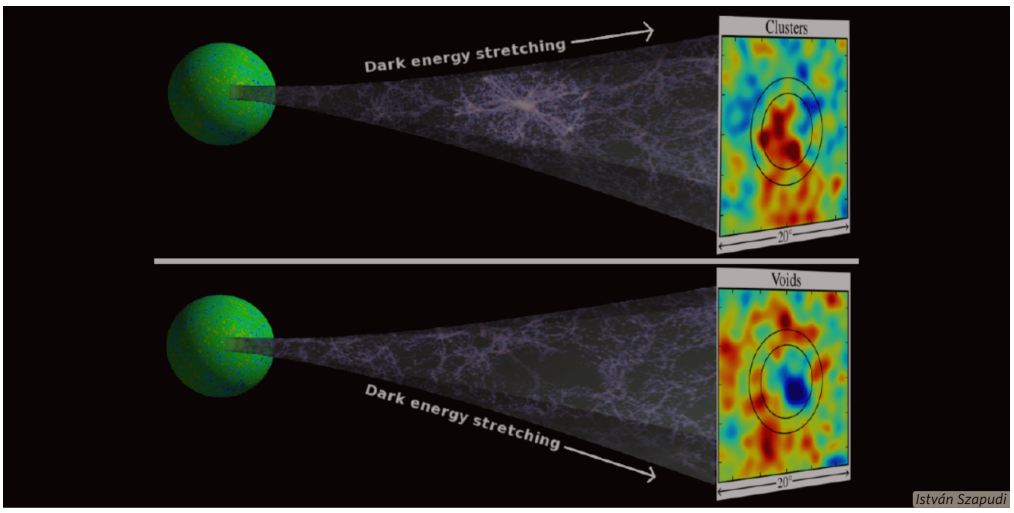

Figure 1.14: Illustration of the ISW effect in accelerating ΛCDM universe. The resulting image shows "hotter" CMB photons from overdensities and "colder" photons from voids. Credit: Istvan Szapudi

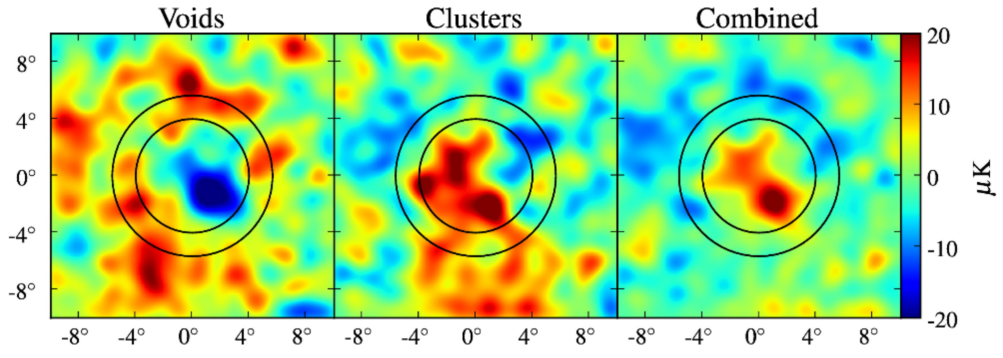

Figure 1.15: Visualization of stacked ISW signal coming from superclusters and voids as taken from (Granett et al., 2008).

In a universe with matter density $\Omega_m = 1$ and no dark energy, density perturbations δ grow proportionally with the scale factor $a = (1+z)^{-1}$. Thus, to linear order, the gravitational potential Φ, which is proportional to $-\delta/a$, remains constant. However, in a ΛCDM universe with dark energy, the scale factor a increases more rapidly than the linear growth of density perturbations, causing the gravitational potential Φ to decrease over time. Then,

$$\frac{\Delta T(\hat{n})}{T_{\rm CMB}} = -\frac{2}{c^2}\int_0^{t_{\rm LS}} \dot{\Phi}(\hat{n}, t)\, dt \tag{1.32}$$

where $T_{\rm CMB} = 2.725\,\mathrm{K}$ represents the mean temperature of the CMB at redshift $z = 0$, t signifies the look-back time , $\dot{\Phi}$ represents the rate of change of the gravitational potential along the path of the photon and $t_{\rm LS}$ is the time to the last scattering surface.

The ISW effect is of significant interest because the condition $\dot{\Phi} \neq 0$ arises exclusively within the context of linear theory during the era of late-time dark energy dominance. As a result, detecting the ISW effect provides a powerful observational direct probe of dark energy and acceleration. The gravitational potential, Φ, is intrinsically connected to the matter density perturbation, δ, via the Poisson equation:

$$\nabla^2\Phi = \frac{3H_0^2\Omega_m}{2a}\delta, \tag{1.33}$$

where δ is the fractional perturbation in the matter density and $a(t)$ is the dimensionless scale factor.

The initial identification of the ISW effect was facilitated by the comprehensive CMB maps produced by the Wilkinson Microwave Anisotropy Probe (WMAP). Among the pioneering investigations that successfully detected the ISW effect are the work of Boughn & Crittenden (2005), Fosalba & Gaztañaga (2004), Fosalba et al. (2003).

Following this breakthrough, numerous studies have focused on measuring and refining the ISW effect through correlations with various tracer catalogs. These research efforts are well-documented in the academic literature, reflecting ongoing improvements in the precision of ISW measurements (Afshordi et al., 2004, Francis & Peacock, 2010, Rassat et al., 2007).

The ISW effect also includes contributions from non-linear gravitational effects, commonly referred to as the Rees-Sciama (RS) effect (Rees & Sciama, 1968). The Rees-Sciama effect, which arises from the gravitational evolution of structures, contributes to the ISW signal, but its impact is relatively minor, accounting for no more than 10% of the total strength of the ISW signal (Cai et al., 2010).

Unlike the ISW effect, which predominantly occurs in scenarios where the expansion rate changes significantly like in dark energy dominated era of ΛCDM,

the Rees-Sciama effect is more pronounced in highly non-linear regimes of structure formation. This effect is expected to be most significant in regions with rapidly evolving massive structures like clusters of galaxies or large voids. The time variation in the gravitational potential due to this evolution leads to an additional redshift or blueshift in the CMB photons, altering their energy slightly as they traverse these potentials.

Voids, characterized by their underdense nature, hold significant promise for ISW studies due to their relative isolation from non-linear effects and minimal gravitational contamination (Schuster et al., 2024). As the largest density depressions in the universe, voids dominate the angular scales relevant to observe the ISW effect in the CMB power spectrum. This makes them particularly valuable for probing the dynamics of dark energy and the ISW effect.

Under the linear growth approximation, density fluctuations evolve as:

$$\delta(\mathbf{r}, z) = D(z)\delta(\mathbf{r}), \tag{1.34}$$

where $D(z)$ is the linear growth factor with normalization $D(0) = 1$.

From a combination of Equation 1.33 and Equation 1.34 one can obtain;

$$\dot{\Phi} = -H(z)\,[1 - f(z)]\,\Phi, \tag{1.35}$$

where $f = \frac{d\ln D}{d\ln a}$ is the linear growth rate of structure.

Therefore, the Equation 1.32 for the ISW effect can be rewritten as:

$$\frac{\Delta T_{\rm ISW}}{T}(\hat{n}) = -2\int_0^{z_{\rm LS}} a\,[1 - f(z)]\,\Phi(\hat{n}, z)\,dz. \tag{1.36}$$

This equation demonstrates that the strength of the ISW effect depends on the gravitational potential, which is more pronounced in large-scale structures at lower redshifts.

1.7.2 Excess ISW Signal Claims from Voids

One of the biggest motivation of this thesis was the claim of ISW excess signals coming from super large voids (Kovács et al., 2019). The methodology used in this study is very similar to the methodology used to detect CMB lensing signals from DES Y1 voids (Vielzeuf et al., 2021). Figure 1.16 shows the main result of Kovács et al. (2019).

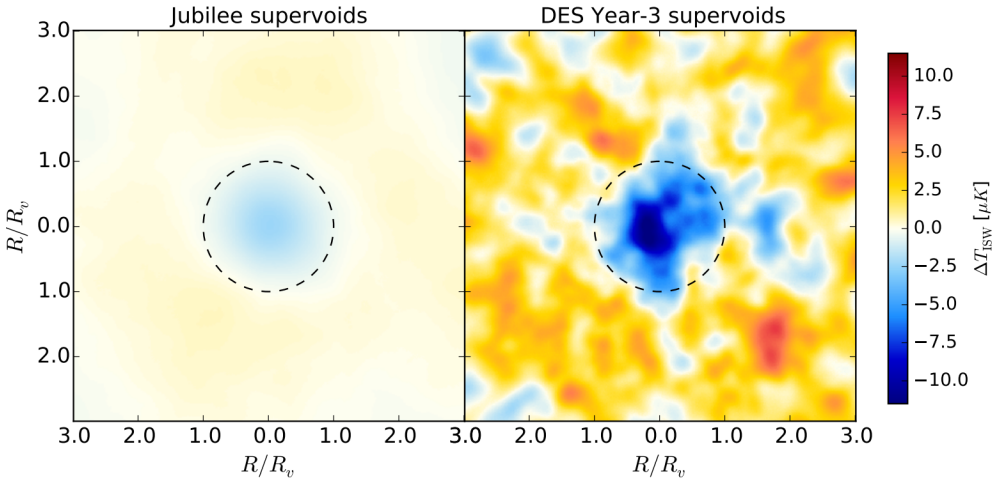

Figure 1.16: This figure presents stacked CMB temperature cutouts centered on positions of very large voids, taken from Kovács et al. (2019). This study utilized the DES Y3 data and Jubilee simulation for ΛCDM calibration, focusing specifically on very large voids. The analysis involved rescaling the void cutouts to normalize their radii (R/R_v).

Furthermore, there is also a claim of sign-changing ISW detected from eBOSS quasars (Kovács et al., 2022). The authors have investigated high-z eBOSS voids ($z = 1$ to $z = 2.2$) in tomographic redshift bins and claim a sign-changing ISW signal for these redshift ranges, which is itself a 2–3, σ discrepancy with ΛCDM.. However, other studies have also investigated the ISW signals of voids, and have found good agreement with ΛCDM expectations (Bahr-Kalus et al., 2022, Dong et al., 2021, Hang et al., 2021, Nadathur & Crittenden, 2016).

There are also some studies that provide theoretical motivations from particle physics for an enhanced ISW effect, such as Hlozek et al. (2015), where the authors investigate the impact of ultralight axions (ULAs). Moreover, Wang & Mena (2024) investigated the tomographic nature of the ISW effect using only CMB data and they

found a good agreement with ΛCDM, but some 2σ deviation at redshift $z = 500$. The study highlighted the need to investigate ISW both tomographically in time and also in space. Ilić et al. (2013) also used stacking methodology to detect the ISW signals as in Granett et al. (2008). Furthermore, the ISW effect has been shown to correlate with thermal SZ effect and this measurement can be used to constrain properties of diffuse gas (Ibitoye et al., 2024). Kovács et al. (2020) attempted a common explanation to the Hubble tension and the claimed ISW anomalies by voids. However, such a study would need to alter the late time expansion history of the Universe and this was shown to be not possible (Alestas & Perivolaropoulos, 2021, Cai et al., 2022, Khalife et al., 2024).

1.7.3 The Cold Spot in the CMB

The discovery of the Cold Spot, an unusually cold area in the CMB has intrigued cosmologists since its initial observation (Cruz et al., 2006), resulting in many studies aimed at unraveling its origins. This discovery was made using a technique that applies Spherical Mexican Hat Wavelet (SMHW) wave functions and this anomalous region has spurred various hypotheses regarding its cosmological implications.

Initial investigations, such as those by Smith & Huterer (2010), explored the possibility of a supervoid in the NVSS (NRAO VLA Sky Survey) aligned with the Cold Spot, potentially explaining the anomaly through the ISW effect. However, these studies found no substantial evidence to support the presence of such a void. This finding was later confirmed by (Mackenzie et al., 2017).

Furthermore, the Cold Spot hypothesis was extensively investigated by Nadathur et al. (2014) and was shown that it is the size of the Cold Spot, its most anomalous feature rather than its temperature depression and also showed that it is impossible to have such a huge void to cause CS in ΛCDM.

Conversely, Kovács et al. (2021) claims that the observed excess ISW signals align with the Cold Spot due to a large supervoid, challenging the conventional ΛCDM model. According to their analysis, such a CS-supervoid connection would necessitate an ISW-void signal enhancement by a factor of 5 to 7 as claimed by Kovács et al. (2019). In other words, the Cold Spot can be attributed to a supervoid

only if the amplitude of ISW signals generally exhibits an excess that is 5 to 7 times greater than the expectations of ΛCDM. This conclusion aligns with the findings presented by Kovács et al. (2019).

Building on these results, recent work by Owusu et al. (2023) has further examined the likelihood of a large void causing the Cold Spot through the ISW effect. Their findings suggest that the existence of such a huge void would be inconsistent with observations from CMB lensing, thereby challenging the void hypothesis and highlighting the need for alternative explanations.

It is important to note that other studies, such as those by Nadathur & Crittenden (2016) and Hang et al. (2021), using data from the BOSS and DESI Imaging DR8 surveys, respectively, have examined ISW-void signals without uncovering any deviations from ΛCDM predictions. Specifically, Hang et al. (2021) employed the same void definition and Gaussian filtering techniques as Kovács et al. (2019) and Kovács et al. (2022), yet found that the amplitude of the detected ISW signal was minimal, aligning well with ΛCDM expectations. This ongoing debate shows the need for further research to resolve these discrepancies.

1.8 Motivation

As highlighted in previous chapters, modern cosmology is transitioning into a data-driven epoch and it creates a way to test for new physics beyond the ΛCDM model. Significant tensions regarding the fundamental parameters of ΛCDM, along with debates surrounding cosmic voids, the ISW effect, and the Cold Spot, are prompting a critical reassessment of this standard cosmological model. While the ΛCDM model has been remarkably successful, it relies on the enigmatic components of dark matter and dark energy, whose natures remain mysterious. Consequently, it is important to rigorously test the ΛCDM predictions. As upcoming surveys will gather more LSS data and more sensitive CMB data, it is increasingly important to develop techniques for their cross-analysis. Voids are gaining attention and have been used in many recent publications. It is predicted that with the sensitivity of upcoming surveys, voids will be even more useful in obtaining cosmological

information. Their low-density environment, without contamination by small-scale baryonic physics, and their ability to evade screening mechanisms make them ideal for studies of dark energy and modified gravity. Additionally, their weak lensing imprint and ISW effect information can be very useful in testing ΛCDM predictions. In this thesis, we explore this potential by analyzing the CMB lensing imprints of superstructures as a test of ΛCDM model.

Chapter 2

Measuring the CMB Lensing Signal of Voids in the DES Y1 Dataset with Template Fitting Method

In this chapter, the majority of the material is derived from the published paper (Vielzeuf et al., 2021), to which I have made significant contributions. My work primarily involved the utilization of `VIDE` voids and debugging the analysis code, thereby substantially contributing to the main results. We employed the DES Y1 dataset, covering $1,300\,\mathrm{deg}^2$, which is considerably smaller than the DES Y3 footprint of $4,200\,\mathrm{deg}^2$. At the time of writing this paper, the only published research on the Cosmic Microwave Background (CMB) lensing imprint of voids was by Cai et al. (2017). In this study, two main void-finding methods are used: the 2D and 3D `VIDE`, and a template fitting method that involved rescaling the CMB cutouts and applying Gaussian filtering to the CMB maps. The main results show good agreement with ΛCDM expectations albeit lower detection significance as compared to other studies shown in this thesis.

2.1 2D and VIDE void identification in DES Y1 dataset and MICE simulation

2.1.1 2D voids in DES Y1 dataset

We run our 2D void finder using two different redMaGiC samples as tracers. The redMaGiC high-luminosity sample applies a stronger cut in luminosity ($L > 1.5L_*$) which offers higher precision in photometric redshift. On the other hand, the redMaGiC high-density sample has a more relaxed luminosity cut ($L > 0.5L_*$), resulting in an increased galaxy density. We then further probe systematic effects by running the void finder on these two rather different samples using two different initial Gaussian smoothing scales, namely 10 Mpc/h and 20 Mpc/h.

We compare the void catalogues in terms of three characteristic parameters of voids: distribution in physical size (r_v), distribution of mean density ($\bar{\delta}$) and distribution in central void density ($\delta_{1/4}$). We observe the following properties:

- Comparing the different resulting catalogues, a higher number of voids is detected when the tracer density is lower (redMaGiC high-luminosity sample). Sutter et al. (2014) found a different behaviour for VIDE voids in simulations. Shot noise appears to drive these effects. In particular, a higher number of pixels are identified as 2D void centre candidates when the tracer density is lower, and the mean density might be reached more frequently, splitting voids up.

- A larger smoothing scale decreases the total number of voids for both tracer densities, as the role of shot noise is reduced.

- The mean void radius is shifted towards larger values for larger smoothings, as smaller voids merge into larger encompassing voids.

- Small smoothing scales result in a larger fraction of deep voids, given the same tracer density. This feature is also related to shot noise properties.

When testing mask effects, we found that the voids identified using redMaGiC tracers in the MICE octant have different properties compared to void properties of DES

Y1-like survey patches inside the octant. We therefore decided to use the same mask as in the DES Y1 cosmological analysis (Elvin-Poole et al., 2018) as this guarantees faithful comparison to the observed data. We consider two rotated positions of the Y1 mask with some overlap that is unavoidable inside the octant. Therefore, as a consistency test, we will study two MICE Y1-like void catalogues (MICE 1 and MICE 2; see Table 2.1 for more details).

2.1.2 VIDE voids in DES Y1 dataset

Aiming at a different catalogue of voids from the same data set, we also run the VIDE void finder on the MICE redMaGiC photo-z catalogue in the full octant, focusing on the high density sample of galaxies.

We find a total of 36115 voids using this 3-dimensional algorithm. The VIDE algorithm provides various output parameters to characterise the voids. We judge that the most important parameters for our CMB lensing study are the effective radius ($r_v^{\rm eff}$), density contrast (r), and the TreeLevel (for details see e.g. Neyrinck, 2008, Sutter et al., 2015a).

Unlike for 2D voids, we find no significant difference in VIDE void properties (such as radius, central underdensity, and redshift distribution) when using Y1-like mask patches or a full octant mask in MICE. This agrees with the findings of Pollina et al. (2019). We therefore consider all voids in the MICE octant for our stacking tests, i.e. a factor of ~ 5 more voids than in a Y1 patch (see also Table 2.1 for void number count comparisons).

In our empirical tests, we found that a $r_v^{\rm eff} > 35$ Mpc/h limit in radius effectively removes small voids that tend to live in overdense environments.The positive central κ imprint of these small voids decreases the negative stacked κ signal inside the void radius, bringing the signal closer to zero thus harder to detect. We also found that an additional cut that removes the least significant voids below the 1σ extremeness level ($r > 1.22$) (Neyrinck, 2008) is helpful to eliminate voids with less negative central imprints and remaining larger voids with positive central imprints. While these choices are subject to further optimisation, we use them in the present analysis in order to test a different definition using a robust and clean VIDE sub-sample.

High luminosity (HL)			
Smoothing	DES Y1	MICE 1	MICE 2
10 Mpc/h	1218	1158	1219
20 Mpc/h	411	364	400
High density (HD)			
Smoothing	DES Y1	MICE 1	MICE 2
10 Mpc/h	427	421	420
20 Mpc/h	122	85	106
`VIDE`	DES Y1	MICE	
All	7383	36115	
Pruned	239	1687	

Table 2.1: We list the numbers of 2D voids identified in two Y1-like MICE patches vs. in DES Y1 data. We also provide void number counts for `VIDE` voids for the full MICE octant and for the DES Y1 data set, with and without pruning cuts that we consider in our measurements.

Finally, we apply a cut with TreeLevel = 0 to only keep voids which are highest in the hierarchy, i.e. do not overlap with sub-voids. These three conditions result in a set of voids that is a very conservative subset of the full catalogue. However, such a pruned catalogue with clean expected CMB κ imprints is sufficient for providing an alternative for our main analysis with 2D voids.

2.2 Simulated cross-correlation analyses

2.2.1 Stacking κ maps on void positions

The CMB lensing imprint of single voids is impossible to detect (see e.g. Krause et al., 2013). We therefore apply an averaging method using cutouts of the CMB map at void positions (see e.g. Kovács et al., 2017, and reference therein). This stacking procedure can be described with the following steps:

- we define a catalogue of voids. We also select subgroups in radius and density bins to probe their specific imprint type.

- we re-scale the angular size of voids to measure distances in dimensionless R/R_v units where R_v is the void radius. We use a patch size enclosing 5 re-scaled void radii to possibly detect the lensing imprint of void surroundings,

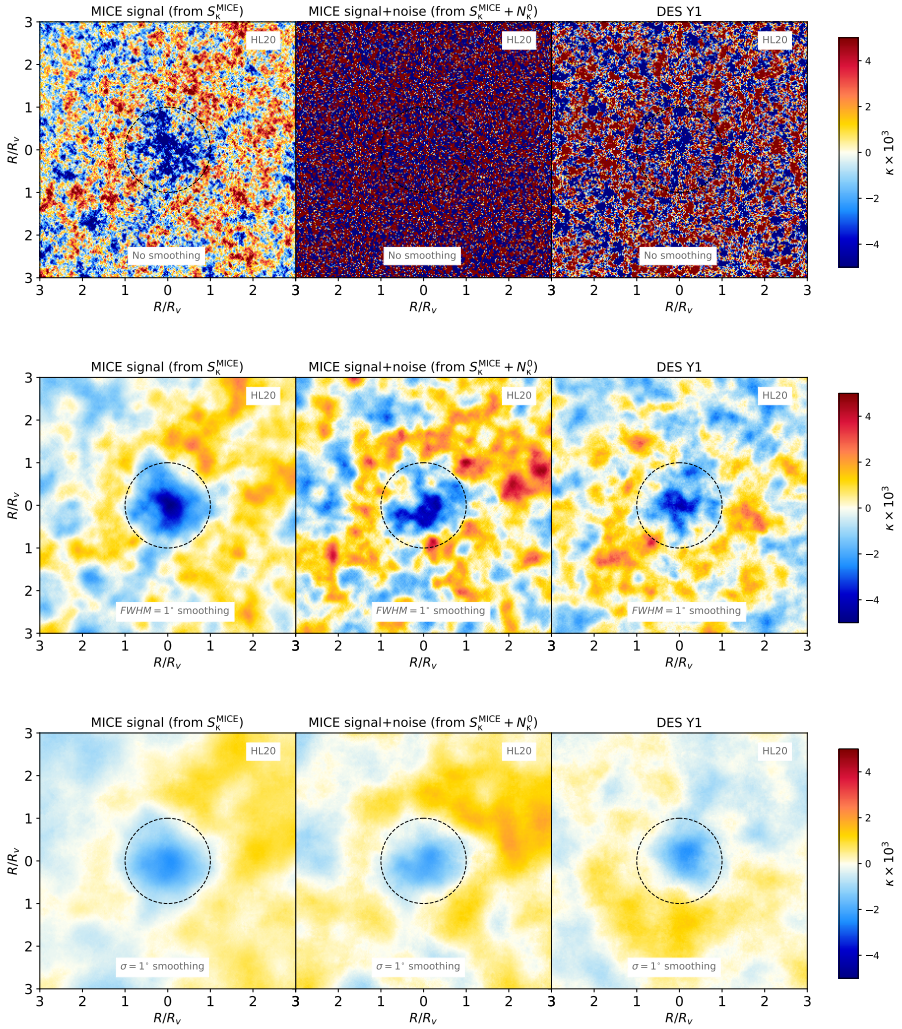

Figure 2.1: Simulated signal-only stacked κ images from MICE (left) in comparison to noise-added versions (centre) and observed DES Y1 stacked results (right) for the HL20 version of 2D voids. All versions of our results are displayed without smoothing (top) and with $FWHM = 1^\circ$ (middle) or $\sigma = 1^\circ$ (bottom) Gaussian smoothings. The re-scaled void radius $R/R_v = 1$ is marked by the dashed circles. We identify important trends with changing smoothing scales but overall report good consistency between data and simulations.

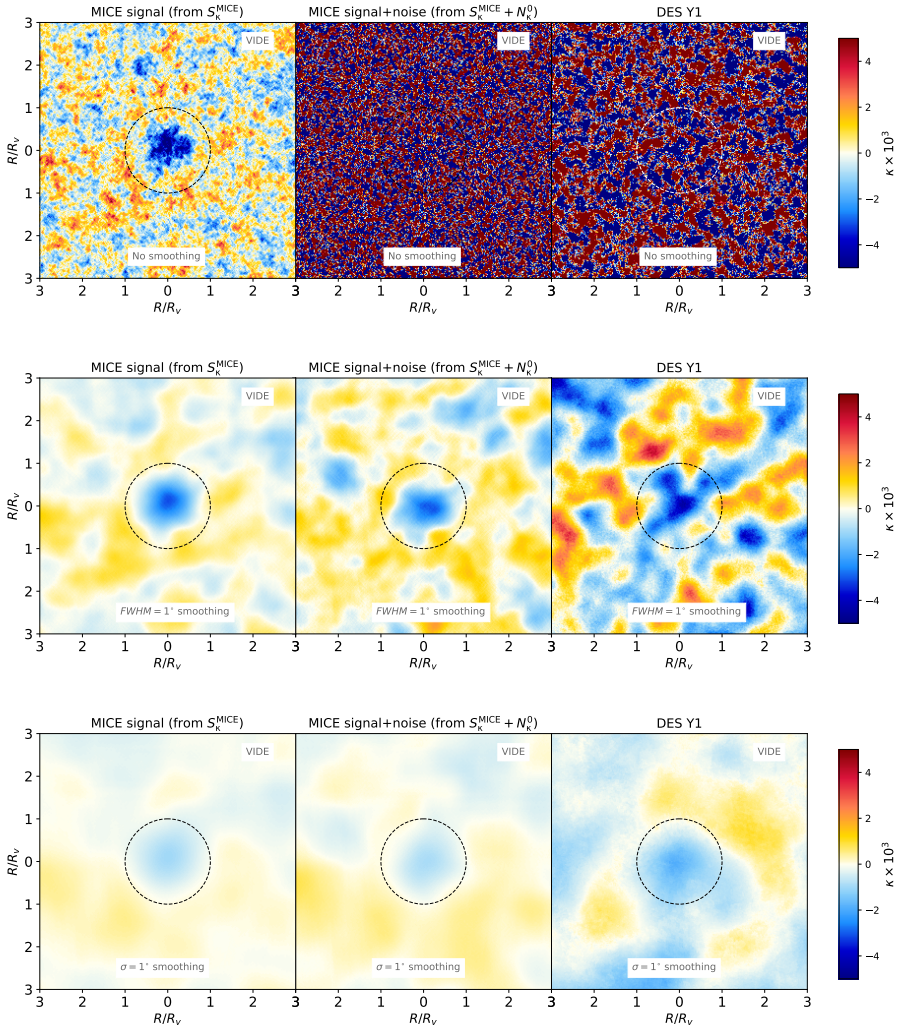

Figure 2.2: Same as Figure 2.1 except we replace the 2D void sample with `VIDE` voids.

such as matter overdensities around voids, i.e. compensation walls (Hamaus et al., 2014).

- we probe the effect of a Gaussian smoothing on the noise properties of the stacked images using different filter sizes applied to the CMB convergence map (not in the re-scaled images).

- we stack using three different strategies: without smoothing; using a full width at half maximum value $FWHM = 1^\circ$; and with a standard deviation $\sigma = 1^\circ$ (equivalent to $FWHM = 2.355^\circ$) to reduce the noise of the measurement. A more optimized analysis could use filters matching the shape of the expected signal to maximize S/N (see Nadathur & Crittenden, 2016, for a similar analysis).

- we found that $FWHM = 1^\circ$ is a good compromise as it efficiently removes fluctuations from very small scales (compared to the typical void size) but it practically preserves the signal itself (see Figure 2.1 and Figure 2.2 for details).

- we cut out the re-scaled patches of the CMB convergence map centred at the void centre position using `healpix` tools (Górski et al., 2005). This allows us to have the same number of pixels by varying the resolution of the images according to the particular void angular size.

- we then stack all patches and measure the average signal in different concentric radius bins around the void centre.

As we use full-sky MICE κ maps but only consider smaller DES Y1-like patches, we also measure the mean κ values in the masked area and remove this bias from the profiles to account for possible large-scale fluctuations that a DES Y1-like survey is affected by. From the *Planck* data, we also remove the mean κ value measured in the DES Y1 footprint. We do not apply any other filtering in the stacking procedure such as exclusion of large-scale modes up to $\ell < 10$ (see Cai et al., 2017, for related results).

2.2.2 Simulated analyses with noise in the κ map

An important source of the measurement uncertainties are the random instrumental noise in the *Planck* data. In order to model observational conditions, we generate 1000 *Planck*-like noise map realisations using the noise power spectra released by the *Planck* team (Planck Collaboration et al., 2020b). We first check how the detectable signal fluctuates around the true signal without rotating the MICE lensing map ($S_\kappa^{\rm MICE}$) in alignment with void positions. In this test we add simulated noise contribution maps (N_κ^i) to the same non-rotated MICE κ (signal-only) map in 1000 random realisations. We find significant fluctuations in the signal in the presence of *Planck*-like noise but no evidence for biases when considering noisy data. Figure 2.1 shows how the signal-only ($S_\kappa^{\rm MICE}$) and noise-added ($S_\kappa^{\rm MICE} + N_\kappa^0$) MICE images compare for a given noise realisation in the case of 2D voids.

We note, however, that the total error of the stacking measurement also has a contribution from random fluctuations in the stacked signal map itself. This sub-dominant contribution is about half the magnitude of the instrumental κ noise based on comparisons of fluctuations in random stacking measurements using the signal-only MICE map $S_\kappa^{\rm MICE}$ or N_κ^i noise maps. This second error is, at least in part, due to the complicated overlap structure of voids themselves along the line-of-sight, overlap with their neighbour voids in the same redshift slice, and also the limited number of available voids in a DES Y1 observational setup. These result in imperfect imprints compared to a hypothetical mean signal of several isolated voids.

Then, to account for both the above sources of error in the void-κ cross-correlation measurement, we first create 1000 noise-added $S_\kappa^{\rm MICE} + N_\kappa^i$ maps. In this case, we randomly rotate $S_\kappa^{\rm MICE}$ and estimate the measurement errors with 1000 runs (void positions and the $S_\kappa^{\rm MICE}$ map are not aligned). However, as the rotated MICE maps may overlap in our 1000 random rotations affecting the estimation of the covariance, we consider an alternative strategy to estimate the measurement errors. We measure the power spectrum of the noiseless full-sky MICE κ map $S_\kappa^{\rm MICE}$ using the `anafast` routine of `healpix`. Then, given the same power spectrum, we create 1000 random map realisations using `synfast`. We then add our N_κ^i noise map realisations to these different S_κ^i MICE-like lensing map realisations, and thus

eliminate the possible correlations between random realisations due to rotation of the MICE map. Finally, we stack the 1000 noisy random maps on void positions, and, as in the MICE and DES Y1 measurements of the imprint signals, we also remove the mean κ map value inside the DES Y1 survey mask area. Our additional tests show that the removal of this monopole κ bias term reduces the overall errors on the A lensing amplitude by about 10%.

We note that while simulated and observed void catalogues are in good agreement (see Figure A.1), we use the observed DES Y1 void catalogues for the estimation of the errors to ensure that the overlap structure or any other correlation between voids is fully realistic. We find that the above error estimation methods give consistent results, but the second `synfast`-based method provides a few per cent larger error bars. This is intuitively expected, since slightly more randomness is added to the stacking process by using independent κ maps instead of rotation of a single one. We therefore consider these more conservative `synfast`-based errors in our covariance estimation process.

For all void catalogues, we repeat all measurements for our three different κ smoothing strategies: no smoothing, and two Gaussian smoothings with $FWHM = 1^\circ$ and $\sigma = 1^\circ$. Figure 2.1 demonstrates how different smoothings of the κ maps affect the results. In Figure 2.1 we also preview the results from stacking measurements using a DES Y1 2D void catalogue to show the reasonable agreement between noise-added simulations and observed data. Other versions of the void catalogue showed consistent results. Figure 2.2 presents our findings on alternative `VIDE` void catalogues in MICE and in DES Y1. We find imprints comparable to 2D void results for our very conservative subset.

2.2.3 Amplitude fitting

In our DES Y1 analysis we wish to perform a template fitting algorithm using the simulated radial κ profiles extracted from MICE stacking analyses. As a measure of the signal-to-noise (S/N) of simulated and observed signals given the measurement errors and their covariance, we aim to constrain an amplitude A (and its error σ_A) as a ratio of DES Y1 and MICE signals using the full profile up to $R/R_v = 5$ in

16 radial bins. We expect $A = 1$ if the DES Y1 and MICE ΛCDM results are in close agreement and we aim to test this hypothesis. In the DES Y1 analysis, we fix the shape of the stacked convergence profile to that calibrated from the MICE simulation. See e.g. Kovács et al. (2019) for a similar analysis with DES voids.

As detailed above, we estimate the covariance using 1000 different *Planck*-like noise simulations (that dominate the measurement errors), and we also add a randomly generated CMB lensing map with MICE-like power spectrum to estimate the full error. We then invert the covariance matrix and correct our estimates by multiplying with the Anderson-Hartlap factor $\alpha = (N_{\rm randoms} - N_{\rm bins} - 2)/(N_{\rm randoms} - 1)$ (Hartlap et al., 2007). Given our measurement configuration, this serves as a small ($\approx 2\%$) correction.

To constrain the A amplitude, we then evaluate a statistic

$$\chi^2 = \sum_{ij} (\kappa_i^{\rm DES} - A\kappa_i^{\rm MICE}) C_{ij}^{-1} (\kappa_j^{\rm DES} - A\kappa_j^{\rm MICE}) \tag{2.1}$$

where κ_i is the mean lensing signal in the radius bin i, and C is the covariance matrix defined above. We perform such a χ^2 minimization for all void catalogue versions and smoothing strategies using the corresponding data vectors and covariances.

2.2.4 Optimization of the measurement

The imprint of voids on the CMB lensing maps depends on their properties. Nadathur et al. (2017) showed that simulated cosmic voids, identified with the `ZOBOV` methodology (similar to `VIDE`), trace the peaks of the underlying gravitational potential differently given different density, size, and environment (see also Cai et al., 2017)]. They reported that voids can be grouped based on a combined density-radius observable to have distinct lensing profiles. In particular, they found that the combination of all sub-populations gives an average profile that is closer to zero at all scales, i.e. harder to detect. For instance, stacked κ images of voids-in-voids are less negative in their centre, while voids-in-clouds show a more pronounced compensation. The overall significance of the measurement can therefore be improved if the distinct imprints of different void types are measured separately and a combined sig-

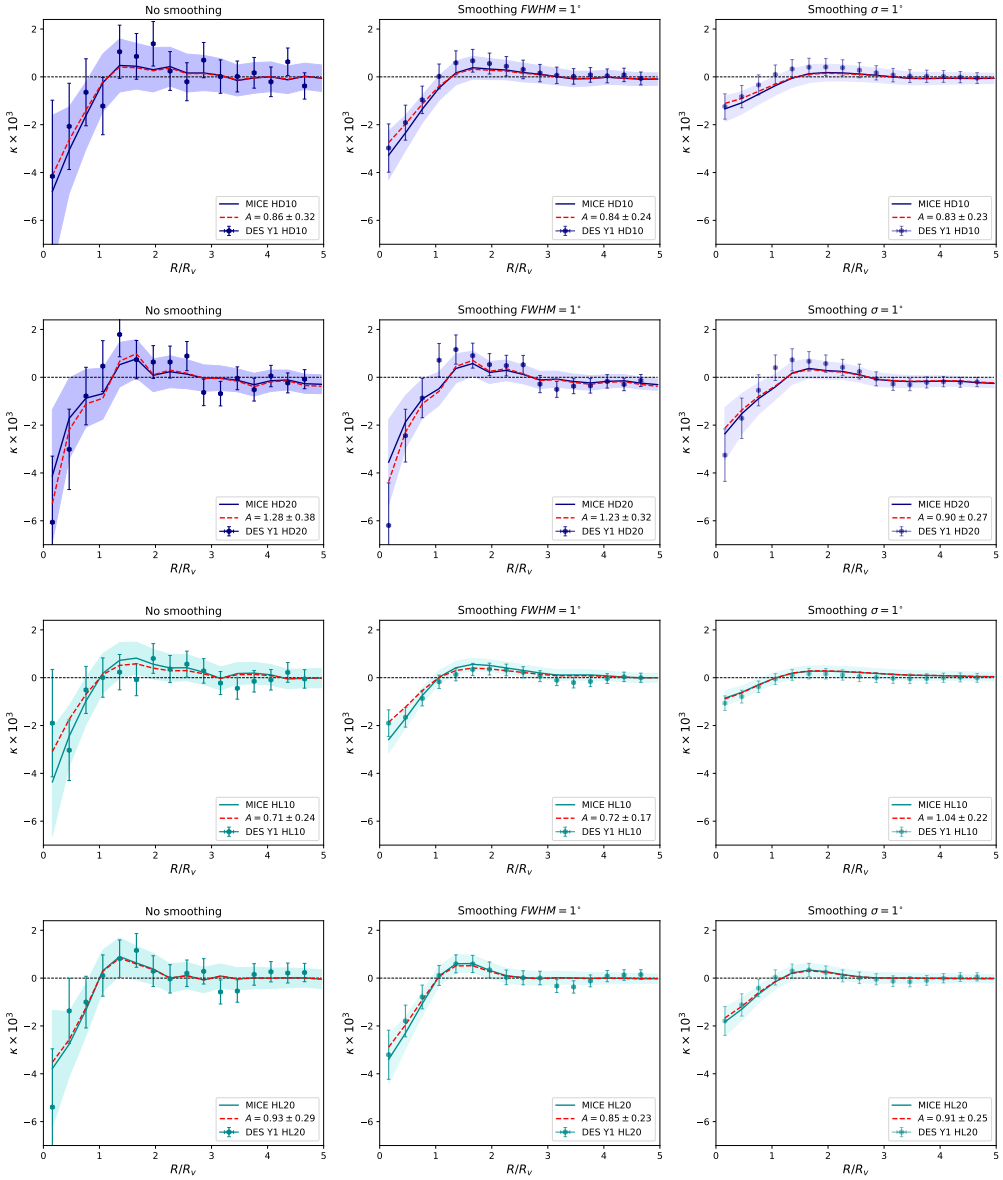

Figure 2.3: Comparison of the radial κ imprint profiles of 2D voids in the MICE simulation and in DES Y1 data. We show results based on all three κ map smoothing strategies, including no smoothing (left), $FWHM$= 1° smoothing (middle), and σ = 1° smoothing (right). For completeness, we present the imprints for all 2D void catalogue versions including HD10, HD20, HL10, and HL20 from top to bottom. Dashed red profiles mark the best fitting MICE templates considering the DES measurements adn the band represents 1σ error bars.

nificance analysis is performed. These findings appear to be robust against changing the galaxy tracer sample but have not yet been tested in photo-z void studies. We thus cannot blindly follow these pruning strategies in our methodology.

2D voids

While 2D voids are different in their nature to 3D voids, we aim to explore the possible optimisation of the void catalogue by pruning in a similar manner. We therefore perform the stacking measurement for subsets of our 2D void catalogues for both tracer densities and two different initial density smoothing scales.

The S/N is first measured in stacked images using individual bins in void radius and underdensity, indicating how sub-classes of voids contribute to the total detection significance. Similarly, we also stack cumulatively, i.e. gradually making use of all the voids in the sample by adding more and more voids from bins of r_v and $\bar{\delta}$, indicating which portion of the radius-ordered and density-ordered data provides the highest detection significance. We make the following observations based on these optimisation efforts:

- medium size voids of radii 40 Mpc/h $< r_v <$ 80 Mpc/h account for most of the observable lensing signal. The magnitude of their lensing imprint is the highest and they are the most numerous subgroup in the void catalogue which results in smaller uncertainties.

- splitting the void catalogue based on the mean underdensity in voids, we find that voids with $-0.2 < \bar{\delta} < -0.1$ carry most of the observable signal. These are rather shallow void structures but they are the most numerous which naturally result in higher statistical precision in the stacking measurements.

- while approximately two thirds of the S/N is contained inside the void radius ($R/R_v < 1$) and in the close surroundings ($1 < R/R_v < 2$), measuring the cumulative S/N up to ($R/R_v = 5$) does increase the detectability and provides a way to test convergence to zero signal at large radii.

- the highest S/N is achieved by stacking all voids, even if some voids are expected to contribute with less pronounced signal and higher noise at small

scales (see Kovács et al., 2017, for a counter-example in the case of ISW imprints).

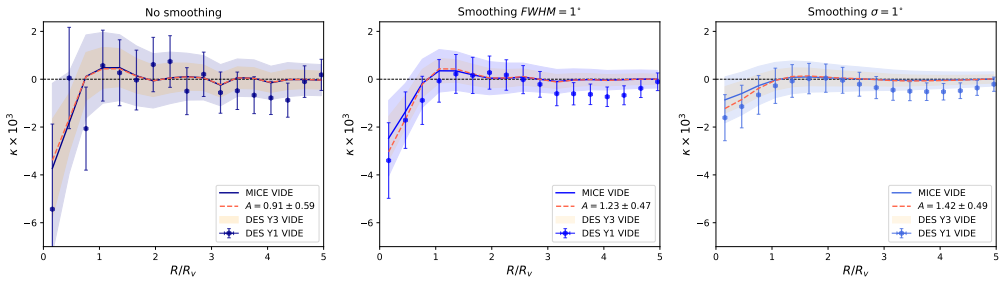

Figure 2.4: We compare the radial κ imprint profiles of VIDE voids in the MICE simulation and in DES Y1 data. We show results based on all three κ map smoothing strategies. Dashed red profiles mark the best fitting MICE templates to the DES measurements. We also mark the expected errors for the Year-3 DES data set that we wish to use in the future to extend this analysis (orange shaded areas around the MICE signals).

In terms of different tracer density and smoothing, the highest S/N is found when using the high luminosity catalogue with 10 Mpc/h smoothing (HL10)(The details of this catalogue is explained in Section 2.1.1). We note that such a result is not unexpected, given the wider redshift range and the larger fraction of deep voids in the HL sample (see Figure A.1).

We estimate $S/N = 4.2$ for the case of no κ map smoothing, while we find an even higher $S/N = 5.9$ and $S/N = 4.6$ for Gaussian smoothings using $FWHM = 1^\circ$ and $\sigma = 1^\circ$, respectively. We use S/N and A/σ_A interchangeably to refer to the signal-to-noise throughout the paper. We consider a DES Y1 measurement configuration and resulting errors and a MICE ΛCDM signal ($A = 1$) of the simulated 2D voids.

Nevertheless, all measurement configurations show moderately significant $S/N \gtrsim 3$ CMB lensing signals for voids in a survey such as DES Y1, and thus we will measure the corresponding observed lensing imprint of all DES void catalogues and smoothing versions. See again Figure 2.1 for details.

We note that the main results above are based on the full void sample with a variety of redshifts in $0.2 < z < 0.7$. For completeness, we also performed a simple redshift binning test for voids of size 20 Mpc/h $< r_v <$ 70 Mpc/h. We found no clear evidence for redshift evolution in their CMB lensing profile.

VIDE voids

Because in this paper we consider VIDE voids as a consistency test, we do not formally optimise the signal-to-noise for the VIDE void sample. Relatedly, we do not have a single recipe for pruning parameters in the presence of photo-z errors for 3D voids. Nevertheless, as explained in Section 3.3.2, we apply various pruning cuts in order to ensure a detectable CMB lensing signal in the MICE simulation and therefore also in DES Y1 data (see Figure 2.2). These cuts result in 1687 VIDE voids in the MICE octant to be used in the stacking measurement, and 239 voids in the DES Y1 redMaGiC high density data. We present a comparison with 2D void types in Table 2.1, finding good consistency in void number counts.

Overall, we find $S/N = 1.7$ for the case of no κ map smoothing, while $S/N = 2.1$ and $S/N = 2.0$ for Gaussian smoothings using $FWHM = 1^\circ$ and $\sigma = 1^\circ$, respectively. In these tests, we again consider a MICE ΛCDM imprint signal ($A = 1$) and a DES Y1 measurement configuration and resulting errors (σ_A) of the simulated VIDE voids.

We note that our pruning cuts in fact remove most of the voids from the original catalogue; thus the VIDE catalogue may promise higher S/N with further optimisation. However, for our purposes of studying a sample complementary to the 2D void analysis the sample defined above is adequate. We leave the optimisation of VIDE catalogues for CMB lensing measurements for future work, including tests of VIDE voids in high luminosity tracer catalogues that appear more promising for the 2D void definition.

2.3 Results from observations: DES Y1 × *Planck*

We measure the stacked imprint of DES Y1 voids with the same methodology and parameters as in the case of the MICE mock. Together with the MICE results, the stacked κ images of the DES Y1 void catalogues are shown in Figures 2.1 and 2.2 for 2D and VIDE voids, respectively. We find good consistency between simulations and observations for all void definitions, smoothing strategy, and tracer density.

We then use the stacked images to calculate a radial κ imprint profile in order to

No smoothing					
Catalogue	`VIDE`	HD10	HD20	HL10	HL20
MICE	1.69	3.12	2.63	4.16	3.45
DES Y1	1.54	2.68	3.40	2.94	3.15
FWHM$= 1^\circ$ **smoothing**					
Catalogue	`VIDE`	HD10	HD20	HL10	HL20
MICE	2.12	4.16	3.12	5.88	4.35
DES Y1	2.61	3.46	3.80	4.13	3.70
$\sigma = 1^\circ$ **smoothing**					
Catalogue	`VIDE`	HD10	HD20	HL10	HL20
MICE	2.04	4.34	3.70	4.55	4.00
DES Y1	2.89	3.55	3.38	4.74	3.62

Table 2.2: Signal-to-noise ratios (A/σ_A) are listed for all measurement configurations using MICE and DES Y1 signals. We compare three different smoothing strategies and five void catalogue versions.

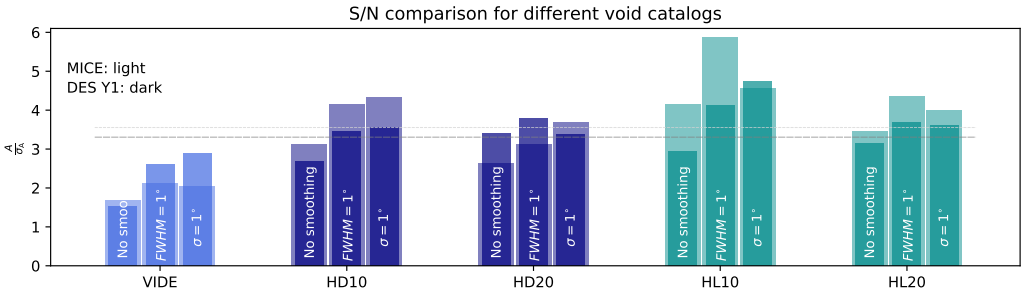

Figure 2.5: We provide a detailed comparison of measurement significance in the form of A/σ_A. The conservative `VIDE` sample also provides useful consistency tests in agreement with our 2D analyses. The dashed horizontal lines mark the mean of the DES Y1 (dark) and the MICE (light) significances with values 3.31 and 3.55, respectively.

quantify the results, relying on the noise analysis we introduced above. We present these results below and provide a detailed description of our constraints on the A amplitude of DES Y1 and MICE void lensing profiles.

2.3.1 2D voids

We continue our data analysis with the DES Y1 2D void catalogues that promised higher S/N in our MICE analysis, where, recall, we forecasted $S/N \approx 5$ for the high luminosity catalogue.

We compare the stacked images of the κ imprints in the high luminosity catalogue

with 20 Mpc/h smoothing in the galaxy density map in Figure 2.1 as a representative example of all 2D void results. A visual inspection shows good agreement between MICE and DES Y1 κ imprints both in the centres and surroundings of the voids. We find consistency for all κ smoothing strategies and report that similar conclusions can be drawn from stacked images from other void catalogue versions (see also Figure 2.2).

We then also measure the azimuthally averaged radial imprint profile in the stacked images to quantify the results. We present the results in Figure 2.3 for all four 2D void catalogue versions HD10, HD20, HL10, and HL20. The shaded blue regions mark 1σ errors computed with 1000 random realisations of the stacking measurement on the MICE κ map with *Planck*-like noise included, while the error bars around DES Y1 measurements show the same uncertainties for the DES data (by construction, we use the same covariance estimation methodology for MICE and DES data as explained in Section 2.2.2). We observe a good general agreement in the sign and the shape of the observed and simulated profiles: negative κ values in the interior of voids plus an extended range of positive convergence in the surroundings. We note that the approximate convergence of the profiles to zero signal at large distance from the void centre is an important null test which proves that our method is not affected by significant additive biases.

We provide the S/N ratios for all catalogue versions and analysis techniques in Table 2.2 and amplitudes with errors in Table 2.3. We observe clear trends in the results, including a natural decrease of both errors and the signal itself if larger Gaussian κ smoothing scales are applied to the CMB map. We see no evidence for significant excess signals or a lack of signal compared to simulations.

As demonstrated in detail in Figure 2.3 for the case of 2D voids, the less promising DES Y1 void catalogue versions tend to robustly show signal-to-noise ratios of at least $S/N \approx 3$. This is in good agreement with the mean of all MICE signal-to-noise estimates $S/N \approx 3.5$. We compare these mean S/N values to individual estimates in Figure 2.5. We find that the DES Y1 constraints on the A amplitude typically favor values slightly lower than $A = 1$, often with $A \approx 0.8$, and this reduces the significance of our detections.

In particular, the highest signal-to-noise is expected for the HL10 sample with $FWHM = 1^\circ$ smoothing (based on the MICE analysis) with $S/N \approx 5.88$. Using the DES Y1 catalogue we constrain $A \approx 0.72 \pm 0.17$ and $S/N \approx 4.13$, i.e. slightly lower than expected. In another promising configuration with the HL10 sample with $\sigma = 1^\circ$ smoothing, we find $A \approx 1.04 \pm 0.22$ and $S/N \approx 4.74$, i.e. slightly higher than expected. Nevertheless we conclude that these results are consistent with expectations from MICE both in terms of amplitude and significance.

We note that our estimates of the stacked CMB κ profile in the MICE mock are in good agreement with the simulated profile shapes and central amplitudes reported by Cai et al. (2017) and Nadathur et al. (2017) even though they used different void definitions and tracer catalogues.

2.3.2 VIDE voids

In Figure 2.4, we present the profile measurement results for VIDE voids for all three smoothing strategies. The profiles with error bars again indicate the signal-to-noise of the visually compelling imprints seen in the stacked images. We conclude that an $FWHM = 1^\circ$ smoothing offers the best chance to detect a signal. The detection reaches $S/N = 2.6$ with $A \approx 1.23 \pm 0.47$, given the DES Y1 survey setup, in good agreement with our predictions from the MICE mock (see more detailed comparisons of expected and measured S/N in Figure 2.5). We find that the best-fit amplitudes are all consistent with the expectation $A = 1$ from the MICE simulation.

As a forecast, in Figure 2.4 we over-plot the expected error bars for the upcoming DES Y3 dataset that will offer a better chance to measure the void CMB lensing signal of DES voids even with a conservatively pruned VIDE catalogue. We expect roughly two times smaller error bars given the approximately four times larger survey area. This translates to an expected $S/N \approx 4.5$ detection for identically selected but more numerous DES Y3 VIDE voids.

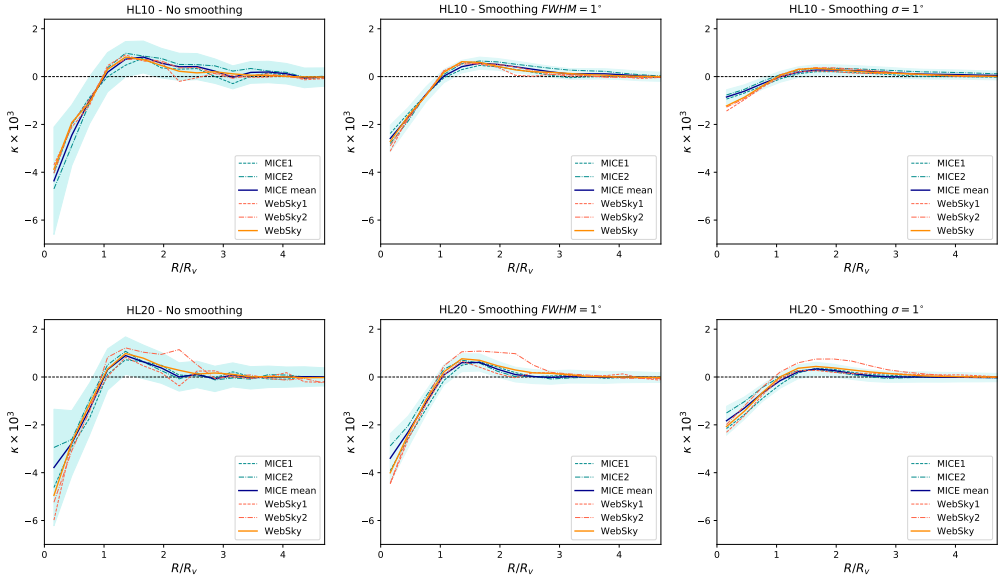

Figure 2.6: Comparisons of stacked imprints of simulated voids using HL10 (top row) and HL20 (bottom row) void finder setups for the three different smoothing strategies we analyze in the paper. Dashed profiles show the stacked imprints in different DES Y1-like patches for the MICE (blue) and WebSky (red) simulations. Solid blue lines represent our baseline estimation of the expected signal as the mean of the signals from the two individual MICE patches. The solid orange profiles mark the more precise full sky estimate of the stacked signal for WebSky data. Changes due to different input cosmologies and field-to-field variations are comparable and are within the errors of our DES Y1 measurements.

No smoothing				
VIDE	HD10	HD20	HL10	HL20
0.91 ± 0.59	0.86 ± 0.32	1.28 ± 0.38	0.71 ± 0.24	0.93 ± 0.29
***FWHM*= 1° smoothing**				
VIDE	HD10	HD20	HL10	HL20
1.23 ± 0.47	0.84 ± 0.24	1.23 ± 0.32	0.72 ± 0.17	0.85 ± 0.23
σ = 1° smoothing				
VIDE	HD10	HD20	HL10	HL20
1.42 ± 0.49	0.83 ± 0.23	0.90 ± 0.27	1.04 ± 0.22	0.91 ± 0.25

Table 2.3: Similar to Table 2, but here amplitudes (A) and their errors (σ_A) are listed for all measurement configurations for DES Y1 signals. In the case of MICE, amplitudes are all $A = 1$ by definition, while the uncertainties are identical.

2.3.3 Testing the role of the input cosmology

In preceding section, we argued that the MICE cosmological parameters with $\Omega_m = 0.25$, $\sigma_8 = 0.8$, and $h = 0.7$ may represent a sufficiently accurate description of the DES Y1 data set that we use in this study, as opposed to the best-fit *Planck* cosmology (Planck Collaboration et al., 2020a) with $\Omega_m \approx 0.315 \pm 0.007$, $\sigma_8 \approx 0.811 \pm 0.006$, and $h = 0.674 \pm 0.005$.

We nevertheless intended to test the shape and the amplitude of the stacked signal of voids in a simulated data set based on the *Planck* 2018. Therefore, we analysed the publicly available[1] WebSky simulation (Stein et al., 2020) package. The WebSky data set provides a light-cone halo catalogue and, among other data products, a corresponding CMB lensing κ map. An important difference is that while the MICE simulation provides realistic mock *galaxy* catalogues that mimic the observed DES Y1 data, the WebSky simulation offers dark matter halo catalogues. In order to make this halo catalogue to be as DES-like as possible, we set the same redshift range and applied a simple halo mass cut to approximately model the population of luminous red galaxies that were used as tracers of voids in our analysis. LRGs are expected to reside in halos of mass $\sim 10^{13} - 10^{14} h^{-1} M_\odot$ (see e.g. Zheng et al., 2009) that is above the mass resolution of the WebSky halo mock catalogue with $\sim 10^{12} h^{-1} M_\odot$. We therefore applied a simple halo mass cut with $M > 10^{13.5} h^{-1} M_\odot$ to define an LRG-like population. In particular, this selection cut is intended to model the high luminosity sample that we compare to the WebSky results below. We also added Gaussian photo-z errors with a `redMaGiClike` $\sigma_z/(1+z) \approx 0.02$ scatter to the simulated WebSky spec-z coordinates to create realistic observational conditions.

We first identified 19,729, and 8,784 voids in the full-sky WebSky simulation data for our usual 10 Mpc/h and 20 Mpc/h initial Gaussian smoothing scales, respectively. We then decided to apply the same DES Y1-like mask to the full sky WebSky data set in order to test how the signal may fluctuate when measured from the full data set as opposed to smaller patches. We note that in fact we used two of these DES Y1-like survey patches in the MICE octant to estimate our signal as

[1] https://mocks.cita.utoronto.ca/data/websky/

their mean and therefore we can also compare the field-to-field fluctuations in the MICE simulation. Therefore, this set of results facilitates a comparison of not just possible differences in the lensing imprint from changes in cosmology, but also a characterisation of simple field-to-field variations in a given cosmology, either MICE or WebSky. With the HL10 setup, we identified 839 and 874 voids in WebSky data with a DES Y1-like mask applied in two cases, and 361 and 380 voids for HL20. The number of voids is somewhat lower compared to our MICE results, but given the lack of realistic `redMaGiC` galaxy mock in the case of WebSky data, such differences are not unexpected, and the results can still be compared meaningfully.

For completeness, we tested all of our different smoothing strategies applied to both the CMB κ map and the galaxy density field given high luminosity (HL) data that promises better precision according to our MICE results and that we intend to model with our pruned WebSky halo catalogue. We present these results in Figure 2.6. We found that, given our measurements errors from the DES Y1 $\times$ *Planck* configuration, differences in the profile from changes in input cosmology are comparable to field-to-field variations if individual DES Y1-like patches are considered either in MICE or in WebSky simulations. We therefore conclude that while in principle changes in cosmological parameters such as Ω_m, σ_8, and H_0 may affect void lensing imprints in the CMB, our current measurements of this signal lack the precision to be sensitive to such small changes in these parameters.

2.4 Discussion & Conclusions

The main objective of this work was to study cosmic voids identified in Dark Energy Survey galaxy samples, culled from the first year of observations. We relied on the `redMaGiC` sample of luminous red galaxies of exquisite photometric redshift accuracy to robustly identify cosmic voids in photometric data. We then aimed to cross-correlate these cosmic voids with lensing maps of the Cosmic Microwave Background using a stacking methodology.

Such a signal has already been detected by Cai et al. (2017) with a significance of 3.2σ. They stacked patches of the publicly available lensing convergence map of the

Planck satellite on positions of voids identified in the BOSS footprint. In general, we followed their methodology but we put more emphasis on simulation analyses to detect a signal with DES data, given different galaxy tracer density and void finding methods. In particular, we used simulated DES-like `redMaGiC` galaxy catalogues together with a simulated lensing convergence map from the MICE *Grand Challenge* N-body simulation to test our ability to detect the CMB lensing imprint of cosmic voids.

We constrained the ratio of the observed and expected lensing systems, which we called A. We first analysed the signal-to-noise corresponding to the CMB κ profile of MICE `redMaGiC` voids. We considered different void populations including 2D voids and `VIDE` voids in 3D. We varied the galaxy density and also the initial smoothing scale applied to the density field to find the centres of the 2D voids (see Sánchez et al., 2016, for details). These parameters affect the significance of the measurement as the total number of voids, mean void size, underdensity in void interiors, and their depth in their centres are all affected by these choices and hence so is the resulting lensing signal and noise.

We then comprehensively searched for the best combination of parameters that guarantees the best chance to detect a signal with observed DES data. We concluded that the lower tracer density of the higher luminosity `redMaGiC` galaxy catalogue is preferable to achieve a higher signal-to-noise for both 10 Mpc/h and 20 Mpc/h initial Gaussian smoothing.

We tested the prospects of using sub-classes of voids instead of the full sample, but concluded that stacking all voids is preferable for the best measurement configuration with DES Y1 data.

We also tested the importance of post-processing in the MICE κ map. We experimentally verified that Gaussian smoothing of scales $FWHM = 1^\circ$ and $\sigma = 1^\circ$ reduce the size of the small-scale fluctuations in the lensing map while preserving most of the signal. For completeness, we created stacked images for all smoothing versions and provided a detailed comparison of the results. In the MICE analysis, we found that the best measurement configurations to detect a stacked signal are achieved when considering a 2D void catalogue with high luminosity tracers and 10

Mpc/h initial density smoothing (HL10), exceeding $S/N \approx 5$ for given κ smoothing strategies.

We then identified voids in the observed DES Y1 `redMaGiC` catalogue and compared their properties with MICE voids. In general, we found a good agreement when comparing observed 2D and `VIDE` void catalogues with both DES Y1-like MICE mocks that we used for predictions. We repeated the simulated stacking analyses using the observed *Planck* CMB lensing map. The signal-to-noise is typically slightly lower than expected from MICE, due to a trend of lower amplitudes at the level of $A \approx 0.8$ in some of the cases. Nevertheless, given the measurement errors, we detected a stacked signal of voids with amplitudes consistent with $A \approx 1$.

Overall, we robustly detected imprints at the 3σ significance level with most of our analysis choices, reaching $S/N \approx 4$ in the best predicted measurement configurations using DES Y1 high luminosity `redMaGiC` data. We found that `VIDE` voids provided similar imprints in the CMB lensing maps, albeit at consistently lower S/N than 2D voids. This finding, however, is not unexpected given the conservative cuts we apply to select our `VIDE` sample. We leave the possible further improvements in the `VIDE` analysis for future work.

Using the WebSky simulation, we also tested how changes in cosmological parameters might affect our results. We found that differences that arise from field-to-field variations in the signal in DES Y1-like patches, and differences due to input cosmology are comparable to each other and are within errors throughout the full imprint profile. Therefore, the level of the precision offered by a DES Y1-like data set combined with the *Planck* CMB κ map is not sufficient for such precision tests. Increased galaxy survey window and a more numerous catalogue of voids, or better precision in the reconstruction of the CMB lensing fluctuations may increase the precision of these measurements in the near future.

Regarding the previously reported excess ISW signal in DES void samples compared to ΛCDM simulations, however, we conclude that the excess in the CMB temperature maps at void locations has no counterpart in the *Planck* CMB lensing map. This finding does not necessarily invalidate the ISW tension. First, Cai et al. (2017) also reported excess ISW signals using BOSS data, but found a stacked κ

signal in good agreement with ΛCDM simulations. Second, no detailed simulation work has jointly estimated the ISW and CMB lensing signal of voids in some alternative cosmologies. It is yet to be analysed if the excess ISW signal should always be imprinted in the corresponding CMB κ map. Such simulation analyses could potentially exclude the coexistence of an enhanced ISW signal and a ΛCDM-like CMB κ imprint, pointing towards some exotic systematic effect that results in an ISW-like excess in *Planck* temperature data aligned with the biggest voids in both BOSS and DES data.

Our goal for the future is to create a bigger catalogue of voids, and potentially superclusters, using galaxy catalogues from three years of observed DES data (DES Y3). Furthermore, joint analyses of CMB lensing and galaxy shear statistics may constrain modified gravity models (see e.g. Baker et al., 2018, Cautun et al., 2018).

In the near future, beyond a better understanding of the methodologies, new simulations and new cosmic web decomposition data from experiments such as the Dark Energy Spectroscopic Instrument (DESI) (Levi et al., 2013) and the Euclid mission (Amendola et al., 2013) will further constrain the lensing and ISW signals of cosmic voids.

.

Chapter 3

Cross Correlation of DES Y3 Weak Lensing Mass Maps with Voids

This chapter is mostly derived from Gatti et al. (2021), where we used voids to cross-correlate with weak lensing mass maps created from the DES Y3 dataset. As explained below, there are different methods for creating mass maps by assuming various Bayesian priors. My main contribution was to use the stacking method, as explained in Chapter 2, and to derive the errors using the Jackknife method by treating each void as a Jackknife bin, rather than using simulations. By doing so, we demonstrate the consistency of different mass map creation methods.

3.1 Mass Map Construction

One of the main goals of large-scale structure surveys such as DES is to measure weak lensing (for a detailed literature review of weak lensing see Bartelmann & Schneider, 2001, Mandelbaum, 2018). By measuring the slight deformations in galaxy shapes caused by the mass distribution between the observed galaxies and ourselves as observers (cosmic shear), we can impose stringent constraints on the cosmological model that describes the Universe and its associated parameters. This is because of the tidal field of matter inhomogeneities along the line of sight. Hence, cosmic shear can be used to characterize the nature of dark energy by examining distant galaxies, across different epochs in the history of the Universe (Huterer,

2002).

Therefore, weak lensing can be used to construct mass maps (convergence maps). These maps contain not only the distribution of dark matter but also the locational attributes of its tracers, including galaxies, galaxy clusters, and cosmic voids.

The cumulative mass encountered along a line of sight is weighted by lensing efficacy, which typically peaks at the midpoint between the source and the observer. One of the key advantages of constructing mass maps is that convergence is a scalar field, making it easier to manipulate and model compared to a shear field, which more directly aligns with actual observations. Additionally, convergence maps preserve the phase information of the mass distribution. This phase information has the spatial arrangement of mass and make it easy to extract higher-order statistics beyond the basic two-point correlation function or power spectrum.

There are some different mass map techniques in the literature, however, the majority of these techniques rely on the foundational approach pioneered by Kaiser & Squires (1993) where authors show an analytical method to convert shear measurements into convergence and this method (KS) has been used in various cosmological analyses, as documented in multiple studies (Chang et al., 2015, Chang et al., 2018, Liu et al., 2015, Oguri et al., 2018, Vikram et al., 2015).

Therefore in this section, we describe the mass map techniques and the void cross-correlation technique to validate these four different weak lensing mass map techniques.

3.1.1 Mass Map Inference

An ideal complex shear field, γ, defined on the full celestial sphere relates to the convergence field, κ, for a given source redshift distribution. This ideal shear field is full-sky, sampled everywhere, and noise-free. Inferring the unknown convergence field from ellipticity measurements of a finite set of source galaxies in the presence of survey masks and galaxy *shape noise* (discussed below) is the challenge of mass mapping.

The real and imaginary parts of the shear γ are relative to a chosen two dimensional coordinate system. In weak lensing, the observed ellipticity (Bartelmann &

Schneider (2001)) of a galaxy $\epsilon_{\rm obs}$ is related to the reduced shear g plus the intrinsic ellipticity of the source galaxy $\epsilon_{\rm s}$ through

$$\begin{aligned} \epsilon_{\rm obs} &\approx g + \epsilon_{\rm s}, \\ \text{where } \; g &= \frac{\gamma}{1-\kappa} \; . \end{aligned} \tag{3.1}$$

In the weak lensing limit, the reduced shear is approximately the true shear, $g \approx \gamma$. This allows an observed shear to be defined, $\gamma_{\rm obs} = \epsilon_{\rm obs}$; this can be interpreted as a noisy measurement of the true shear that has been degraded by shape noise (caused by the unknown intrinsic ellipticities $\epsilon_{\rm s}$ of the observed galaxies):

$$\gamma_{\rm obs} \approx \gamma + \epsilon_{\rm s} \; . \tag{3.2}$$

The shape noise is larger than the lensing signal by a factor of $\mathcal{O}(100)$ per galaxy. It is therefore a dominant source of noise.

In a Bayesian framework we consider the posterior distribution of the convergence κ conditional on the observed shear γ (here we have dropped the subscript $_{\rm obs}$ for brevity) and on the model $\mathcal{M}$:

$$p(\kappa|\gamma, \mathcal{M}) = \frac{p(\gamma|\kappa, \mathcal{M}) \; p(\kappa|\mathcal{M})}{p(\gamma|\mathcal{M})} \; , \tag{3.3}$$

where $p(\gamma|\kappa, \mathcal{M})$ is the likelihood (encoding the noise model), $p(\kappa|\mathcal{M})$ is the prior, and $p(\gamma|\mathcal{M})$ is the Bayesian evidence.

We formulate all reconstructed convergence κ maps as the most probable maps (given our observed data and assumptions); this is the peak of the posterior i.e. the *maximum a posteriori* estimate. From equation 3.3 we see that the *maximum a posteriori* estimate is given by

$$\hat{\boldsymbol{\kappa}} = \arg\max_{\boldsymbol{\kappa}} \; \log p(\boldsymbol{\gamma}|\boldsymbol{\kappa}, \mathcal{M}) + \log p(\boldsymbol{\kappa}|\mathcal{M}) \; , \tag{3.4}$$

where $\mathcal{M}$ is our model (which in our case changes depending on the chosen prior distribution). Here, the elements of the vectors $\boldsymbol{\kappa}$ and $\boldsymbol{\gamma}$ are the pixel values of a

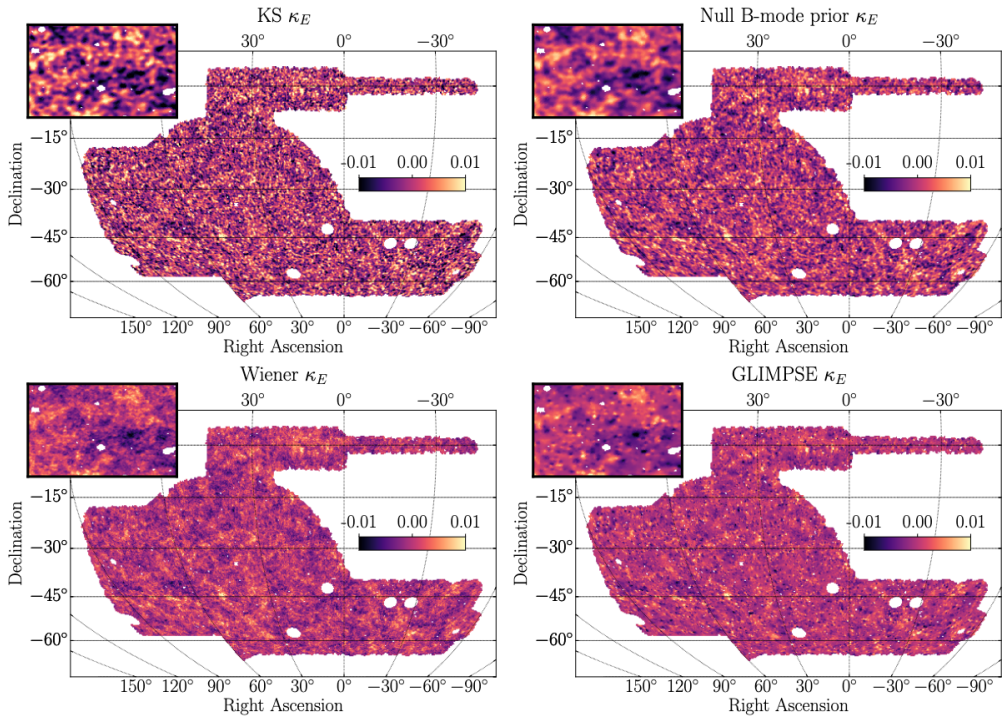

Figure 3.1: Figure taken from Gatti et al. (2021) shows DES Y3 weak lensing mass maps, derived from the official DES Y3 shear catalog and generated using various map-making techniques. Top left: KS E-mode map. Top right: E-mode map created with the null B-mode prior method. Bottom left: E-mode Wiener filter map. Bottom right: E-mode Glimpse map. The maps in the top panels have been smoothed to 10 arcminutes, whereas the maps in the bottom panels have not undergone any additional smoothing.

pixelized convergence map and the observed shear field, respectively.

Figure 3.1 shows the expected differences in maps constructed using various algorithms, primarily due to their different prior choices. They illustrate the advantages and disadvantages of each method in different scientific contexts. We focus on four widely-used methods that encompass the most popular approaches: the Kaiser-Squires (KS) method, the null B-mode prior method, the Gaussian prior (Wiener filtering), and the halo-model sparsity prior called GLIMPSE. Below, we provide an overview of each of these methods. Since the detailed processes of mass map making are beyond the scope of this thesis, we concentrate on the main similarities and differences among these methods. For further details, see Gatti et al. (2021).

3.1.2 Mass Map Making Methods

While the main focus and contribution in this thesis is on cross-correlating cosmic voids with these mass maps, understanding the differences in map-making methods helps in interpreting the results.

Kaiser Squires (KS) method is based on analytical solution proposed by Kaiser & Squires (1993). This is straightforward, direct inversion technique with no assumptions (uniform prior), making it easy to implement but highly sensitive to noise and masked areas, often producing spurious B-modes near edges.

Null B-Mode method, however, enforces a prior that eliminates B-modes, which are not expected in weak lensing, providing better noise and edge artifact suppression compared to KS, though it still benefits from some smoothing.

Wiener Filter method assumes a Gaussian prior, and usually good at recovering large-scale structures while effectively suppressing noise, though it may smooth out fine details on small scales.

Glimpse (Sparsity Prior) approach assumes that the mass map is sparse in a wavelet basis, meaning it consists of a few significant, quasi-spherical structures, like dark matter halos. Therefore, this method is ideal for reconstructing sharp, small-scale features like dark matter halos in contrast to Wiener method, while minimizing noise without overly smoothing the map.

3.2 Cross Correlation with Voids

To assess the robustness of different mass maps with respect to true galaxy underdensities and to understand how each method differs from the others, we cross-correlate the mass maps with DES Y3 voids by stacking galaxy void positions on the created mass maps. In order to do so, we rely on a similar method outlined before in Vielzeuf et al. (2021), with the exception that we use Jackknife-based error estimates instead of simulations. It should also be mentioned that `REVOLVER`(Nadathur et al., 2019) voids used in this study are ZOBOV-based voids in contrast to `Voxel` based voids.

Cosmic void imprints

Cosmic voids are an increasingly favoured cosmic probe and have now already been successfully used to extract cosmological information (for a recent overview see Pisani et al., 2019). We expect these large lower-density regions in the cosmic web to display a typical imprinting in the convergence signal when cross-correlated with weak lensing mass maps (for previous results from DES Y1 data see Chang et al., 2018).

We create a catalogue of so-called '2D voids' (Sánchez et al., 2016) from the DES Y3 `redMaGiC` (Rozo et al., 2016) photometric redshift data set by searching for projected underdensities in tomographic slices of the galaxy catalogue. On average, these tunnel-like voids correspond to density minima that are compensated by an overdense zone in their surroundings. With this simple approach, we detect 3, 222 voids in the DES Y3 data set, which are larger on average, although also less underdense, than most voids from other void finders (see e.g. Fang et al., 2019). They certainly are useful tools in void lensing studies (Davies et al., 2018) and they have been widely used in previous DES analyses (see e.g. Fang et al., 2019, Kovács, 2018, Kovács et al., 2019, Vielzeuf et al., 2021).

The lensing imprint of typical individual voids is expected to be undetectable (Amendola et al., 1999). Therefore, after selecting our void sample, we follow a stacking method to measure the mean signal of all voids (see e.g. Vielzeuf et al., 2021). Knowing the angular size of voids, we re-scale the local mass map patches around the void centres. In such re-scaled units, we then extract convergence κ patches five times the $R/R_v = 1$ void radius, stack them to increase signal-to-noise, and measure radial profiles from the average κ patch. Without a large set of simulations to estimate covariance of the void profile statistic, we estimate uncertainty using a void-by-void jackknife method (see e.g. Sánchez et al., 2016). We then correct these re-sampling based uncertainties with reference to previous DES Y1 void analysis results that used more accurate Monte Carlo simulations (Vielzeuf et al., 2021).

Fig. 3.2 shows the measured profiles using the DES voids. As anticipated, we detect a negative convergence signal within the void radius ($R/R_v < 1$) and a sur-

rounding ring ($1 < R/R_v < 3$) of positive convergence signal (due to compensating mass around voids). We note that different mass map versions show consistent signals (within the quoted uncertainties). While these void lensing results remain open to much further quantitative work, there is certainly clear detection of correlations between underdensities of galaxies and matter; this will motivate further studies using DES Y3. We finally remark that the typical convergence signal associated with local underdensities can be affected by the void definition and selection. We explore alternative void samples extracted from DES Y3 data in Section 3.3.

Line-of-sight underdensities

Posing a slightly different question, we also examine the distribution of galaxies in a line-of-sight aligned with the most negative fluctuations in the DES Y3 mass maps. We call these *voids in lensing maps* or *voles* (see e.g. Davies et al., 2018). We use a slightly modified version of the 2D void finder algorithm to identify them in the DES mass maps. We apply a Gaussian smoothing of 2 deg in order to intentionally select relatively deep and extended voles.

Following the previous DES Year 1 (Y1) analyses (Chang et al., 2018), the `redMaGiC` galaxy position catalogue is projected into two-dimensional slices of 100 h^{-1} Mpc along the line-of-sight. This thickness corresponds to the approximate photo-z errors of the `redMaGiC` galaxies that allows the robust identification of voids (see Sánchez et al., 2016, for details). At redshifts $0.1 < z < 0.7$, galaxy density contrasts are measured in 15 tomographic slices aligned with voles. Galaxies are counted within an aperture of 2 deg of the void centre, which approximately corresponds to the full angular size of voles. The measured density contrasts at the different redshifts are used to reconstruct the radial density profile aligned with the given vole. Fig. 3.4 shows the line-of-sight galaxy density aligned with a significant vole at $(\mathrm{RA}, \mathrm{Dec}) \approx (41.2°, -12.2°)$ in the KS map.

We find an extended underdensity that is consistent with a super-void with radius $R_\mathrm{v} \approx 250\ h^{-1}$ Mpc (assuming simple Gaussian void profiles as in Finelli et al. 2016). This super-void, similar to the biggest underdensity found in the preceding DES Y1 analysis (Chang et al., 2018), will have smaller-scale substructures that are

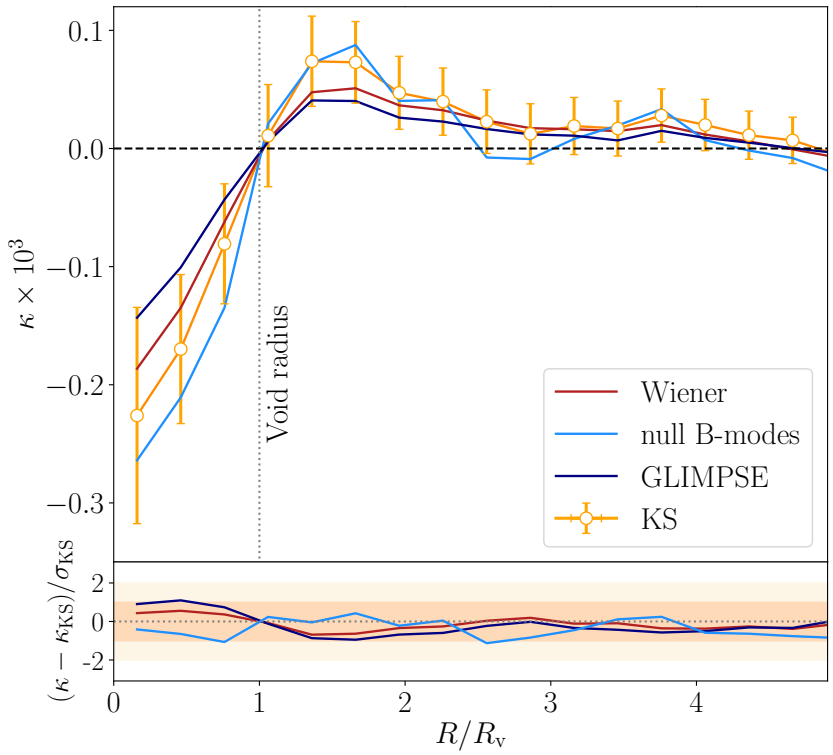

Figure 3.2: *Top panel:* Void imprints on the DES mass maps. *Bottom panel:* Differences of signals measured from different mass maps, relative to the KS results and errors (shaded ranges are 1σ and 2σ about the KS signal).

inaccessible using `redMaGiC` photometric redshift data. Nevertheless, such a super-void is comparable to the largest known underdensities in the local Universe, and these objects are of great interest in cosmology (see e.g. Shimakawa et al., 2021). Their integrated Sachs-Wolfe imprint has already been studied using DES Y3 data to probe dark energy (for details see Kovács et al., 2019).

3.3 Alternative Samples of Voids

We considered alternative catalogues of voids to test how the mass map imprints may depend on the void definition and selection.

`VIDE`[1] (Sutter et al., 2015b) is a watershed void finder based on `ZOBOV` (Neyrinck, 2008) that has been widely employed for various void studies (see e.g. Hamaus et al.,

[1]https://bitbucket.org/cosmicvoids/

2020, and references therein). It has already been successfully used to study voids in the DES Y1 data (Fang et al., 2019, Pollina et al., 2019).

VIDE's default centre is the volume-weighted barycentre, which does not generally coincide with the density minimum inside the void due to non-spherical void geometry. Instead, the barycentre preserves information about the void boundary. Therefore, a different kind of imprint signal is expected when correlated with convergence maps, with more pronounced positive rings rather than negative centres (for a comprehensive study on the κ signal associated with voids see Cautun et al., 2016). In the DES Y3 redMaGiC data, VIDE detected 12,841 voids. We then halved this catalogue using the *compensation* of voids to further increase and isolate the expected signal from the boundary zone, expecting to see an enhanced positive convergence κ imprint from these over-compensated voids.

We are also interested in detecting the most pronounced negative κ signals associated with a specific subclass of large and deep voids that are *under*-compensated. As a third option, we thus used the public[2] void finder algorithm REVOLVER (Nadathur et al., 2019, 2018), also based on the ZOBOV algorithm.

A proxy for the gravitational potential (and thus for the convergence field) at the positions of voids can be defined as

$$\lambda_v \equiv \overline{\delta}_g \left(\frac{R_{\rm eff}}{1\ h^{-1}{\rm Mpc}} \right)^{1.2} , \tag{3.5}$$

using the average galaxy density contrast $\overline{\delta}_g = \frac{1}{V} \int_V \delta_g \, {\rm d}^3\mathbf{x}$ and the effective spherical radius, $R_{\rm eff} = \left(\frac{3}{4\pi} V \right)^{1/3}$, where the volume V is the total volume of the void (for further details see Nadathur & Crittenden, 2016, Nadathur et al., 2017). Raghunathan et al. (2020) showed that different values of the λ_v parameter indicate different (CMB) lensing imprints, including signals with either positive or negative sign, aligned with the void centre[3]. Following this, we keep only 7,782 of the most under-compensated voids defined by the lowest λ_v values. Leaving more detailed analyses for future work, we note that a subclass of voids with high λ_v values would also correspond to over-compensated voids such as our VIDE sample.

[2] https://github.com/seshnadathur/REVOLVER/

[3] REVOLVER voids may also be defined using barycentres.

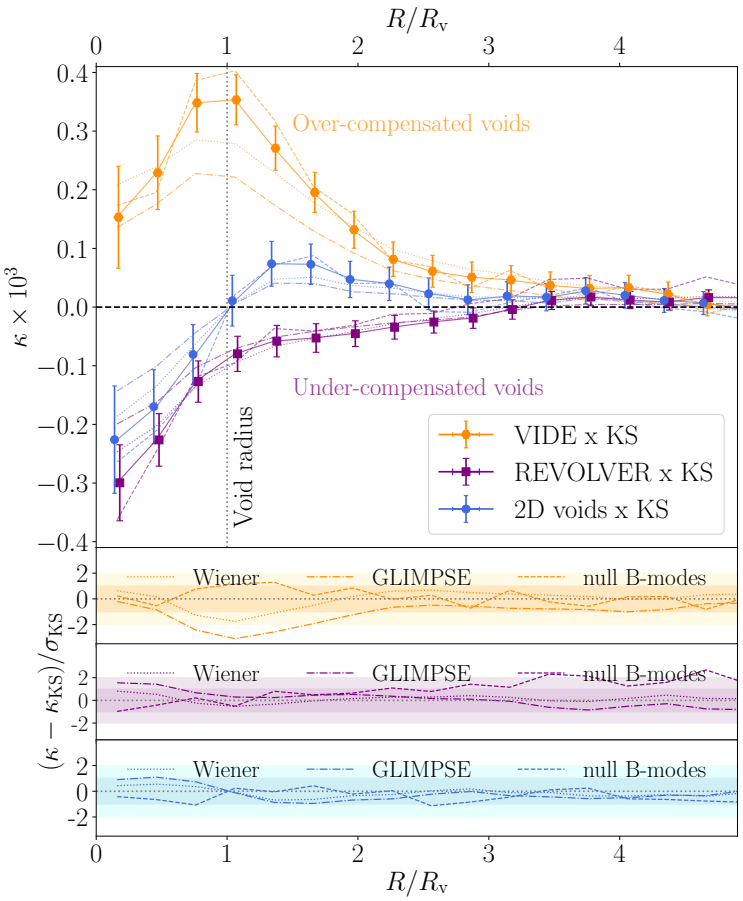

Figure 3.3: *Top panel:* Different mass map imprints of different types of voids. *Bottom panel:* Differences in signals measured from different mass map reconstructions, relative to the KS results and errors (shaded ranges are 1σ and 2σ around the KS results).

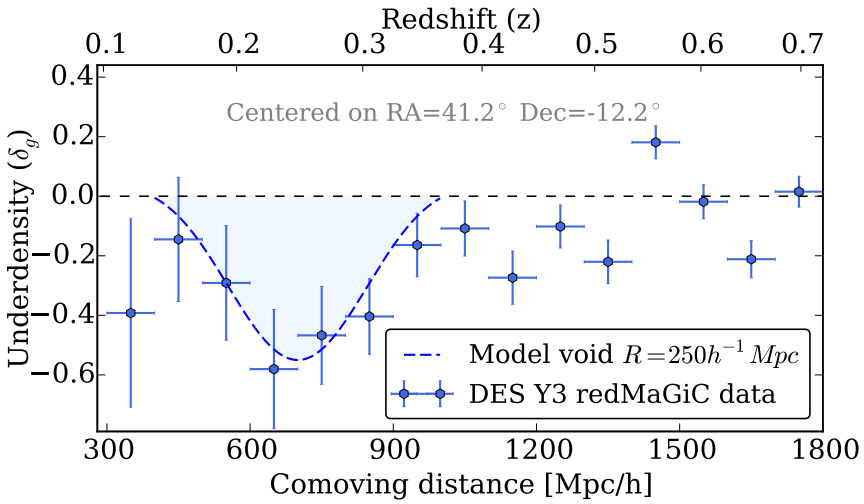

Figure 3.4: The line-of-sight density of `redMaGiC` galaxies aligned with a significant "vole" in the KS mass map. At low redshifts, we find evidence for an extended system of underdensities.

Fig. 3.3 shows the measured profiles of our `REVOLVER`, `VIDE`, and 2D void analyses given the uncertainties. As anticipated based on the differences in the nature of the voids we selected, we detected qualitatively different signals in each case:

- the `VIDE` voids show a relative depression in convergence at the void centre compared to the pronounced peak at the void boundary, matching our expectations.
- the `REVOLVER` voids we selected are associated with strong negative κ imprints that in fact extend far beyond the void radius, indicating surrounding voids on average.
- 2D voids combine the advantages of the other finders. They excel in marking the actual radius of voids in the mass map profiles, with reduced central and wall amplitudes.

We thus report that all three void types we consider show consistent signals when mass maps are varied for a given void sample. We leave more detailed analysis for future work.

Chapter 4

Measuring the CMB Lensing Signal of Voids in the DES Y3 Dataset with Matched Filtering Approach

This chapter of the thesis is primarily based on my peer-reviewed published work Demirbozan et al. (2024), titled "*The Gravitational Lensing Imprints of DES Y3 Superstructures on the CMB: A Matched Filtering Approach*".

4.1 Introduction

Early large-scale galaxy surveys have revealed that the Universe's structure forms a cosmic web, featuring dense filaments and galaxy clusters alongside under-dense regions known as cosmic voids (Peebles, 1980). As observational data has expanded, these vast regions, primarily devoid of matter and dark matter, have gained heightened attention (e.g., see Hamaus et al., 2016, Kovács et al., 2022, Nadathur et al., 2019, Nadathur et al., 2020a, Raghunathan et al., 2019, Vielzeuf et al., 2021, Woodfinden et al., 2023).

In particular, cosmic voids have proven to be useful tools for advancing cosmological studies. They offer a means to constrain the Neutrino mass sum (Kreisch et al., 2019, Lesgourgues et al., 2013, Lesgourgues & Pastor, 2006, Massara et al., 2015, Vielzeuf et al., 2023, Villaescusa-Navarro et al., 2013). Additionally, their

abundance and density profiles aid in distinguishing Modified Gravity models from General Relativity (GR), with voids' ability to bypass screening mechanisms in high-density environments being particularly noteworthy (Khoury & Weltman, 2004, Li et al., 2012, Martino & Sheth, 2009, Pisani et al., 2019, Vainshtein, 1972).

As a result, voids offer an environment that is sensitive to physics beyond the standard model of cosmology. They are sensitive to many effects, such as the growth rate of cosmic structure and redshift space distortions (Hamaus et al., 2017, 2016, Nadathur et al., 2020b, Woodfinden et al., 2022, 2023), Alcock-Paczynski distortions (Hamaus et al., 2016, Lavaux & Wandelt, 2012, Nadathur et al., 2019), weak gravitational lensing (Clampitt & Jain, 2015, Fang et al., 2019, Melchior et al., 2014, Raghunathan et al., 2019, Sánchez et al., 2016), baryon acoustic oscillations (Kitaura et al., 2016), and the integrated Sachs-Wolfe effect (Granett et al., 2008, Kovács et al., 2022, Kovács et al., 2019, Nadathur & Crittenden, 2016, Sachs & Wolfe, 1967).

The large-scale structure of the Universe can influence the observed cosmic microwave background (CMB) and imprint secondary anisotropies. For instance, weak secondary CMB anisotropies, shaped by the evolving low-z structure, provide key observational tests for dark energy. In particular, Kovács et al. 2022, Kovács et al. 2019 have shown an excess ISW signal from large voids that deviates from the predictions of the ΛCDM model. These findings have intensified interest in CMB lensing signal of voids, as this offers an alternative test of these secondary anisotropies.

Several recent works (e.g. Ade et al., 2019, Schmittfull & Seljak, 2018, Tanimura et al., 2020) have studied the cross-correlation between constructed weak CMB lensing convergence maps (κ) and large-scale structure. For example, it was shown that CMB lensing can be used to measure the masses of dark matter haloes (initial detections include Baxter et al., 2015, Madhavacheril et al., 2015, Planck Collaboration et al., 2016c) and to explore the non-linearities in structure formation through its correlation with cosmic filaments (He et al., 2018). However, unlike filaments and clusters, cosmic voids, as under-dense regions, cause an anti-lensing effect and imprint a negative κ signal on the constructed CMB lensing map.

The CMB lensing imprints of voids have been measured by various authors (Cai et al., 2017, Hang et al., 2021, Kovács et al., 2022, Raghunathan et al., 2019, Vielzeuf et al., 2021) with detection significances ranging from $\sim 3\sigma$ up to $\sim 9\sigma$. However, Kovács et al. (2022) found the amplitude of the lensing signal to be low, in moderate $\sim 2\sigma$ tension with predictions from simulations, and Hang et al. (2021) also found hints of lower-than-expected lensing from voids. Given the other tensions in the late-time measurements of cosmological parameters with the predicted values from ΛCDM (Abdalla et al., 2022, Heymans et al., 2021, Riess et al., 2019, Verde et al., 2019), any discrepancy in the CMB lensing signal from voids would be of great interest.

The stacked CMB lensing signal from voids is strongly influenced by specific void parameters. A typical void features a low-density core (with overdensity $\delta < 0$) which may be surrounded by a compensating marginally overdense region ($\delta > 0$). For most voids, the low central matter density gives rise to a de-lensing effect, characterized by $\kappa < 0$ around the line of sight through the void center. However, depending on the relative amplitudes of the density fluctuations in the core and the surrounding overdensity and their physical extents, the convergence profile $\kappa(\theta)$ at angle θ from the void centre may differ, showing dips and rings of different widths (Nadathur et al., 2017, Raghunathan et al., 2020). This in turn can depend on the properties of the void-finding algorithm used for identification.

The objective of our study is to re-examine the CMB lensing imprint of voids in the DES Y3 data using a matched filtering method, as outlined in (Raghunathan et al., 2019), and to employ the `Voxel` void finder algorithm, which has not been previously utilized in DES. Moreover, we explore the variation of the CMB lensing signal with respect to redshift and the type of void finder employed. In contrast to prior studies by (Hang et al., 2021, Kovács et al., 2022, Raghunathan et al., 2019), which each employed a single type of void finder, our study implements two different void finders to enhance the depth and range of our findings.

This paper is structured as follows: Section 2 explains our observed and simulated data sets. Section 3 outlines our methods for identifying voids and superclusters, as well as our matched filtering technique. Our primary observational findings

are detailed in Section 4, while Section 5 offers a comprehensive discussion and concludes the study.

4.2 Data and Simulations

4.2.1 Observational Data

Dark Energy Survey Year-3 Data

We identify cosmic voids using photometric redshift data from the first three years (Y3) of the Dark Energy Survey (DES). DES is a six-year sky survey, with Y3 covering approximately one-eighth of the sky (5000 deg^2) to a depth in the i_{AB} band of less than 24, imaging around 300 million galaxies in five broadband filters ($grizY$) up to redshift $z = 1.4$ (for details see e.g. Dark Energy Survey Collaboration, 2016, Flaugher et al., 2015).

We use a luminous red galaxy sample from the DES Y3 dataset. This Red-sequence Matched-filter Galaxy Catalogue (*redMaGiC*) (see Rozo et al., 2016, for DES science verification (SV) test results) is a catalog of photometrically identified luminous red galaxies, with the red-sequence Matched-filter Probabilistic Percolation (redMaPPer) cluster finder algorithm (Rykoff et al., 2014). This algorithm has been used in many DES analyses (Fang et al., 2019, Gruen et al., 2016, Kovács, 2018, Kovács et al., 2022, Sánchez et al., 2016, Vielzeuf et al., 2021).

The *redMaGiC* galaxies offer the benefit of a low photo-z error, approximately $\sigma_z/(1+z) \approx 0.013$. This error rate is half that of the *MagLim* galaxy sample from DES Y3, which stands at $\sigma_z/(1+z) \approx 0.027$ (Porredon et al., 2022). For comparison, we consider the study by (Kovács et al., 2022) which utilized an earlier version of *redMaGiC*. Hence, we adopt the updated *redMaGiC* v0.5.1 for this research.

The *redMaGiC* algorithm produces various catalogs, distinguished by the densities and luminosities of the galaxies. Specifically, the High Density (HD) catalog maintains a consistent galaxy density, roughly $\bar{n} \approx 10^{-3} h^3\,\mathrm{Mpc}^{-3}$ along the redshift range. Conversely, the High Luminosity (HL) catalog exhibits a galaxy density of $\bar{n} \approx 4 \times 10^{-4} h^3\,\mathrm{Mpc}^{-3}$, which is considerably lower than its HD counterpart.

In our analysis, we focus on the redshift range $0.2 < z < 0.8$ and make use of the empirically constructed DES Y3 survey mask, which excludes contaminated pixels, mainly due to nearby stars. This low photo-z error of *redMaGiC* allows us to robustly identify void environments. The details of the clustering analysis of the DES Y3 *redMaGiC* sample are documented in Pandey et al. (2022). It is also important to mention that this study identified certain systematic errors, to which our measurements are not sensitive, as we correlate them with an external LSS tracer, the CMB lensing map.

Planck CMB Lensing Map

We utilize the full-sky public Cosmic Microwave Background (CMB) lensing convergence (κ) maps from the Planck survey's 2018 data release (Planck Collaboration et al., 2020b).[1]

More specifically, we employ the `COM_Lensing_4096_R3.00` map, which is reconstructed using a minimum-variance (MV) quadratic estimator (Hu & Okamoto, 2002b). This estimator is based on a combination of foreground-cleaned *SMICA* (Planck Collaboration et al., 2016a) CMB temperature and polarization maps, with the mean field subtracted and a conservative mask applied to galaxy clusters to reduce contamination from thermal Sunyaev-Zel'dovich (tSZ) contributions. Throughout our analysis, we use $N_{\rm side} = 512$ *HEALPix* maps (Górski et al., 2005). We note that this $N_{\rm side} = 512$ resolution is an appropriate choice considering the degree-scale imprints of voids.

The gravitational lensing of the CMB, occurs due to spatial variations in the gravitational potential field, $\Phi(r, \theta)$, as CMB photons traverse the Universe. The convergence can be described by the following equation:

$$\kappa(\theta) = \frac{3H_0^2\Omega_m}{2c^2} \int_0^{r_{\rm max}} \frac{(r_{\rm max} - r)r}{r_{\rm max}} \delta(r, \theta)\, dr \tag{4.1}$$

where r is the comoving distance and $r_{\rm max}$ is the comoving distance to the last scattering surface of the CMB. This κ is a dimensionless quantity and measures all

[1]Downloaded from https://pla.esac.esa.int/#cosmology

the projected matter density up to the CMB surface and is weighted by a kernel for a given angular direction depending on the distance. The gravitational potential is also related to the matter density fluctuation δ via the Poisson equation:

$$\nabla^2\Phi = \frac{3H_0^2\Omega_m}{2a}\delta, \tag{4.2}$$

where δ is the perturbation in the matter density and $a(t)$ is the dimensionless scale factor.

4.2.2 Simulation - MICE CMB Lensing Map and *redMaGiC* Tracers

We utilize the publicly available MICE (Marenostrum Institut de Ciencies de l'Espai) simulation, which is an N-body light-cone extracted from the MICE Grand Challenge (MICE-GC). The MICE-GC contains approximately 70 billion dark-matter particles in a $(3h^{-1}\text{Gpc})^3$ comoving volume. This simulation was created using the Marenostrum supercomputer at the Barcelona Supercomputing Center (BSC)[2], running the `GADGET2` code (Springel, 2005). For details on the creation of the MICE simulation, see Crocce et al. (2015), and Fosalba et al. (2015).

The MICE simulation assumes a flat standard ΛCDM model with input fiducial parameters: $\Omega_m = 0.25$, $\Omega_\Lambda = 0.75$, $\Omega_b = 0.044$, $n_s = 0.95$, $\sigma_8 = 0.8$, and $h = 0.7$, derived from the Five-Year Wilkinson Microwave Anisotropy Probe (WMAP) best fit results (Dunkley et al., 2009a).

In this study, we utilize the CMB lensing map from the MICE simulation, generated using the "Onion Universe" methodology as detailed in Fosalba et al. (2008). The validity of this lensing map was subsequently confirmed through auto- and cross-correlations with foreground MICE galaxy and dark matter particles (refer to Fosalba et al. (2015) for an in-depth description of the map creation process). Initially, the MICE κ map was provided with a *HEALPix* pixel resolution of $N_{\text{side}} = 2048$. However, we downgraded the map to a lower resolution of $N_{\text{side}} = 512$. This adjustment significantly reduces the computational expense without causing a loss

[2] www.bsc.es

of much information, given that voids are degree-scale objects. We also downgrade the resolution of the *Planck* κ map to $N_{\rm side} = 512$ employed in our analysis.

We chose the *redMaGiC* tracers on our mock galaxy catalog from MICE, maintaining consistency with the methodology utilized in the analysis of the observed DES Y3 data Rozo et al. (2016). It is pertinent to note that the coverage of MICE dark matter halos is confined to an octant of the sky (5169.25 deg^2), which is larger than the effective footprint of DES Y3 (4147.15 deg^2). This MICE-*redMaGiC* mock galaxy catalog was constructed to match the number density of the DES Y3 *redMaGiC* sample. It served as our tool to trace the distribution of galaxies on a large scale and to identify voids.

It is important to emphasize that the MICE cosmological parameters are relatively distant from the best-fit *Planck* cosmological parameters Planck Collaboration et al. (2020a). For example, the difference in the values of Ω_m and the Hubble constant H_0 can affect the amplitude of the lensing signal. However, we assume that variances in cosmological parameters, particularly Ω_m, negligibly impact our lensing signal measurements. This postulation aligns with findings from Vielzeuf et al. (2021) and Kovács et al. (2022), who, utilizing the WebSky simulation Stein et al. (2020), showed minimal influence of Ω_m on the CMB lensing signal's amplitude. Additionally, our methodology encompasses a comprehensive error analysis, particularly addressing the MICE template uncertainties, ensuring the accuracy of our findings despite potential Ω_m discrepancies.

In this context, it is important to mention that, as detailed in Nadathur et al. (2019), Vielzeuf et al. (2021), the parameter that seems to have the most significant impact on the determination of the matter content and the lensing convergence of voids is σ_8. The value of σ_8 in the MICE simulation, which is 0.8, is not far off from the best-fit Planck value of $\sigma_8 = 0.811 \pm 0.006$. Additionally, (Nadathur, 2016) and (Nadathur & Hotchkiss, 2015a) have identified the primary factors influencing the size and number of voids in any galaxy sample as the mean galaxy number density, the amplitude of galaxy clustering and the linear galaxy bias. Furthermore, σ_8 also affects void density profiles, especially close to void center (e.g., see Figure 5 in Nadathur et al., 2019).

4.3 Method

Our approach aligns with the matched filtering technique detailed in Nadathur & Crittenden (2016), Raghunathan et al. (2019). Notably, Nadathur & Crittenden (2016) evaluated the ISW imprint of voids, emphasizing that this technique avoids dependence on arbitrary choices of additional tuning parameters (such as the smoothing scale for Gaussian filtering of the CMB) that could introduce biases.

Utilizing the `Voxel` void parameters, $\bar{\delta}_g$ and R_v, we introduce a dimensionless parameter:

$$\lambda_v \equiv \bar{\delta}_g \left(\frac{R_v}{1\ \mathrm{Mpc}/h} \right)^{1.2} . \tag{4.3}$$

This parameter, as empirically demonstrated by Nadathur et al. (2017), exhibits a strong correlation with void density profiles and their macroscopic environments. As such, λ_v serves as a pertinent proxy for the gravitational potential associated with voids. Given this relationship, we expect notable variations in the lensing convergence profiles of voids based on their respective λ_v values.

4.3.1 Void and Supercluster Finding

`Voxel` Voids

The main goal of this research is to measure the CMB lensing signal from voids using two different void definitions: `Voxel` and 2D. The `Voxel` method is designed specifically for datasets with fragmented survey footprints, like DES Y3. One of the key benefits of `Voxel` is that it estimates the galaxy density field by computing number counts on a mesh, normalised by the counts of unclustered random points whose distribution accounts for the survey window function. This is the same method as used for estimating densities when computing power spectra: its use provides a natural way to account for variations in the survey selection function, and makes the `Voxel` algorithm better at handling gaps or fragmented survey masks than algorithms that employ Voronoi tessellations to estimate the density field. However, after the density field has been estimated, `Voxel` identifies voids using a watershed algorithm similar to that used by other, tesellation-based, algorithms (Nadathur &

Percival, 2019, Neyrinck, 2008, Sutter et al., 2015b, e.g.).

The algorithm generates the mesh size, denoted as $N_{\rm mesh}$, based on the tracer mean number density. The size of the mesh is set based on the condition that every cubic grid unit, known as a voxel, should possess a side length represented by $a_{\rm vox} = 0.5 \times \left(\frac{4\pi\bar{n}}{3}\right)^{-\frac{1}{3}}$. Here, $\bar{n}$ stands for the estimated average density of galaxies. The galaxy density field is then subsequently smoothed using a Gaussian filter of size $n_t^{-1/3}$ where n_t is the mean number density of tracers. After this step, local minima are identified across the voxels. Basins are formed around each local minimum, mirroring the process used in earlier `ZOBOV` algorithm (Neyrinck, 2008). The addition of adjacent voxels with increasing overdensity to the basin halts when the next voxel shows a lower density than its predecessor. Each resulting basin signifies a `Voxel` void.

For each identified `Voxel` void, we compute an average galaxy overdensity $\bar{\delta}_g$ and define an effective spherical radius R_v, which equates to the radius of a sphere with a volume equivalent to that of the void.

We generate the `Voxel` void catalogs for both DES Y3 and MICE simulation using the open-source `REVOLVER` void-finding code Nadathur et al. (2019)[3].

Void sizes in the MICE simulation range from $1.95h^{-1}\text{Mpc} \leq R_v \leq 61.96\,h^{-1}\text{Mpc}$, peaking around the median value $R_v = 19.37\ h^{-1}\text{Mpc}$. Meanwhile, for the DES, void sizes range from $2.04h^{-1}\text{Mpc} \leq R_v \leq 59.41\ h^{-1}\text{Mpc}$, peaking around the median value $R_v = 19.98\ h^{-1}\text{Mpc}$. Both MICE and DES have a median void redshift of $z = 0.57$. We perform a comparative analysis of the number density of `Voxel` voids identified in both the MICE and DES Y3 datasets per comoving volume $(\text{Mpc}/h)^3$, as shown in Figure 4.1.

By applying the `Voxel` void finder to the updated `redMaGiC` galaxies, we obtained notable insights. Our preference for HD tracers of `redMaGiC` in identifying `Voxel` voids was influenced by their enhanced CMB lensing signal-to-noise ratio. Our tests confirmed that HD voids exhibit a higher S/N than HL voids, enhancing the efficacy of the matched filter method over other tracer densities. This outcome is primarily attributed to the reduced galaxy density in the HL.

[3]Available at https://github.com/seshnadathur/Revolver

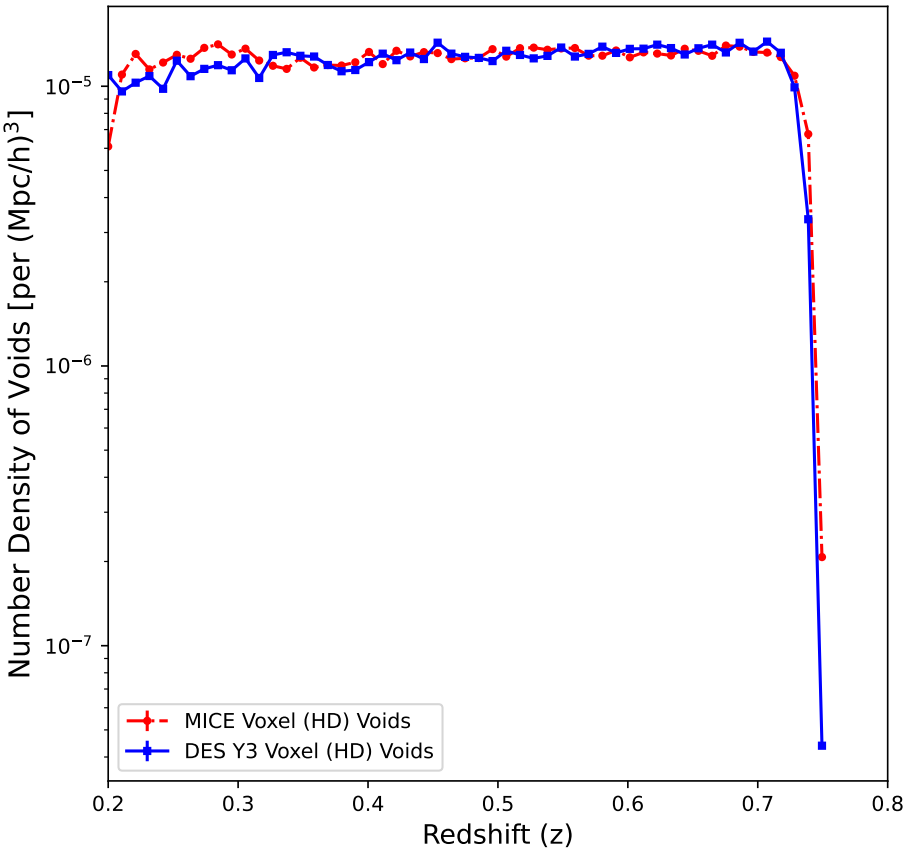

Figure 4.1: Histogram illustrating the distribution of `Voxel` void number density per unit volume in both the MICE and DES Y3 HD catalogs.

Table 4.2 outlines our findings: 44,426 voids in the MICE catalog and 33,427 voids in the DES Y3 catalog, both identified using High Density (HD) tracers. The disparity in void counts between MICE and DES Y3 is due to differences in effective sky coverage: MICE covers 5169.25 deg^2 while DES Y3 covers 4143.17 deg^2. Consequently, the total voxel void number densities for MICE and DES Y3 are 8.59 voids/deg^2 and 8.07 voids/deg^2, respectively. Although our primary interest lies in voids within the $0.2 < z < 0.8$ redshift range, data constraints restricted our `Voxel` void analysis in the MICE catalog to a maximum redshift of $z = 0.75$.

2D Voids

We also employ a 2D void finder, an algorithm initially developed for photometric redshift surveys. This algorithm identifies voids within tomographic redshift bins, which are slices of space at different redshift ranges (Sánchez et al., 2016). The 2D void finder has been employed in several DES studies Kovács et al. (2019, 2022), Vielzeuf et al. (2021).

The 2D algorithm inspects possible minima in the galaxy density field, which has been projected and smoothed for each redshift slice. The void radius R_v is defined when the density inside a thin annulus around the void center reaches the mean density of the redshift slice, increasing the annuli by 1 h^{-1}Mpc. While R_v is typically measured in degrees and then converted to h^{-1}Mpc for consistency, we opt to use degrees in our matched filtering analysis.

Key parameters for the 2D void finder include the smoothing scale for the galaxy density maps, the redshift slice thickness, and the central minimum pixel density. We adopt a smoothing parameter of $\sigma = 10\ h^{-1}$Mpc, a central pixel density that is at least 30% of the most underdense pixels in the redshift slice, and a slice thickness of $s \approx 100h^{-1}$Mpc. This results in 12610 and 10904 voids for MICE and DES Y3, respectively.

To remove potentially spurious objects due to variations in photometric redshift, a measure of redshift derived from the photometric observations of an object, we apply a cut of $R_v > 20h^{-1}$Mpc, following the precedent set in Vielzeuf et al. (2021) and Kovács et al. (2022). After this cut, the number of 2D voids reduces to 6295 for MICE2 and 5148 for DES Y3.

Normalizing by the effective area, the 2D void densities are approximately 1.22 voids/deg^2 for MICE2 and 1.25 voids/deg^2 for DES Y3 within the total redshift range. Just as with the `Voxel` voids, the 2D void densities of MICE and DES Y3 align closely. This implies that the discrepancies in absolute void count largely arise from the differences in effective areas: 5169 deg^2 for MICE2 and 4147 deg^2 for DESY3. Figure 4.2 shows the 2D void number density per unit volume as a function of redshift bins. Specifically, we find that MICE (voids/deg^2) = 1.22, while DES Y3 (voids/deg^2) = 1.25, which indicate a close alignment between the two. For a

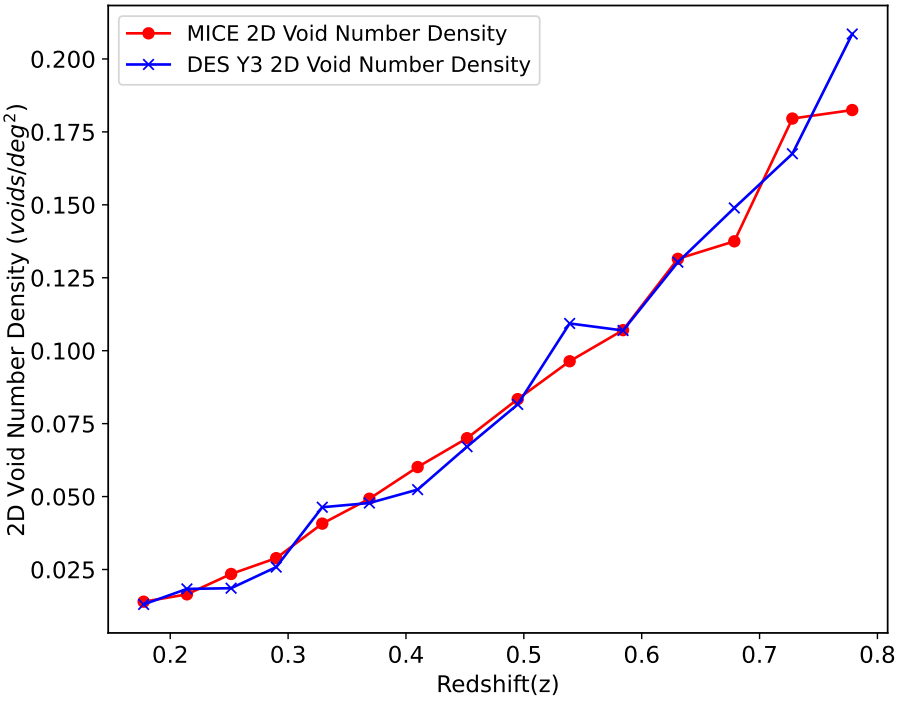

Figure 4.2: Histogram illustrating the distribution of 2D void number density per unit volume as a function of tomographic redshift bins for the MICE and DES Y3.

detailed view, refer to Table 4.1.

For this analysis, we utilize the High Luminosity (HL) tracers from our updated `redMaGiC` v0.5.1 sample, this tracer density type choice is consistent with Kovács et al. (2022) and has also been used with 2D voids in other DES studies (Kovács et al., 2022, 2021). The study conducted by Kovács et al. (2022) is particularly relevant to our analysis as it also examined DES Y3 2D voids defined on HL tracers and used the MICE simulation, similar to our approach. The key difference lies in their filtering and stacking method, which differs from ours. Therefore, it becomes intriguing to investigate the extent of the difference these distinct methods can cause, given the similarity in both the dataset and the simulation used. This choice was made with the aim of examining the effects of an alternative method, the matched filter, on our measurements.

Table 4.1: Comparison of 2D Voids and 2D Superclusters in MICE and DES Y3. Total numbers without any cut are as follows: MICE 2D Voids: 12610, MICE 2D Superclusters: 13167, DES Y3 2D Voids: 10904, DES Y3 2D Superclusters: 10592.

Category	Redshift	MICE (>20Mpc/h)	DES Y3 (>20Mpc/h)
2D Voids	Low	1201	921
	Mid	1840	1512
	High	3254	2715
	Total (>20Mpc/h)	6295	5148
2D Superclusters	Low	1043	809
	Mid	1556	1338
	High	2885	2285
	Total (>20Mpc/h)	5484	4432

2D Superclusters

In order to supplement our analysis of 2D voids and provide further validation of our results, we have expanded our study to include 2D superclusters. To identify these superclusters, we applied the same 2D void finder to the tomographic galaxy density maps used in the previous void analysis, but with a twist: we inverted the density maps by multiplying them by -1. This operation effectively flips the galaxy density map, facilitating the detection of voids in the newly inverted galaxy density landscape. As such, the detected 'voids' in this inverted landscape correspond to superclusters in the original data. It is important to mention that our main reason for using this supercluster definition is to be consistent with Kovács et al. (2022). The superclusters found in this way represent overdense structures on a large scale within the distribution of galaxies, though they may not be bound by gravity. Similar to how voids are associated with extensive troughs in the density field, superclusters are linked to prominent peaks in this field (Nadathur & Hotchkiss, 2014).

Using this method, we compiled a catalog of 2D superclusters, finding 5424 superclusters in the MICE simulation and 4432 superclusters in the DES Y3 dataset after applying a size cut of $R_v > 20h^{-1}$Mpc. We then apply the same redshift binning as in 2D voids and we obtain the 2D supercluster numbers in Table 4.1.

4.3.2 Void Lensing in MICE Simulation

To begin, we inspect the void lensing imprints within the MICE simulation to calibrate the void lensing profiles $\kappa(\theta)$. This involves stacking 10° x 10° patches, derived from the full-sky MICE κ map and centered on each void. These stacks reveal a negative κ imprint (divergent lensing) at the center of the void, signifying the void's central underdensity. In contrast, a less conspicuous positive imprint encircles this, denoting matter overdensities at the outer periphery of the void. The measured radial profiles from these stacks can be seen in Figure 4.3.

Unlike some studies (Cai et al., 2017, Hotchkiss et al., 2015, Kovács et al., 2019, 2022, Vielzeuf et al., 2023, Vielzeuf et al., 2021) that adopt a re-scaling method, our measure of void lensing signals is in units of degrees (θ). This choice stems from our use of the matched filtering approach, akin to Raghunathan et al. (2019), which necessitates that these simulation template void lensing profiles are defined as $\kappa(\theta)$. Importantly, by not re-scaling, we maintain uniformity in the noise power from the CMB lensing map across all void measurements. This is critical because the noise in the CMB lensing map is scale-dependent; thus, re-scaling might inadvertently mix different levels of noise power across various scales.

Additionally, Nadathur et al. (2017) has shown a stronger correlation between the void lensing signal and λ_v, as defined in Equation 4.3—a function of void radius R_v and void overdensity $\bar{\delta}_g$—than with the angular size of voids.

We organize the MICE void sample into three distinct redshift bins, labelled **LOWZ**, **MIDZ**, and **HIGHZ**. This allows us to account for possible redshift-dependent variations in the CMB lensing imprints of voids.

Further granularity is achieved by subdividing each redshift bin into three separate λ_v bins. Importantly, each λ_v bin is populated with an approximately equal quantity of voids, a methodological decision that aligns with the approach used in (Raghunathan et al., 2019). By proceeding in this way, we derive a total of nine bins for our `Voxel` void sample.

As anticipated, the void lensing imprint strongly depends on the value of λ_v. More explicitly, voids with negative λ_v values, such as those in bins 1 and 2, correlate with slightly larger, lower-density voids, exhibiting $\kappa \leq 0$. On the other

Table 4.2: This table presents the number of `Voxel` voids alongside the mean void size within each redshift bin for both MICE and DESY3 datasets with sky fraction being 0.125 and 0.100, respectively. For the detailed `Voxel` void size distribution across all 9 void bins see Figure A.2 in the Appendix.

	MICE Void Count	DES Y3 Void Count
LOWZ (0.2 - 0.43)	9,298	6,821
MIDZ (0.43 - 0.59)	14,679	10,861
HIGHZ (0.59 - 0.75)	20,449	15,027

	MICE Mean Void Size	DES Y3 Mean Void Size
LOWZ (0.2 - 0.43)	20.01 (Mpc/h)	20.57 (Mpc/h)
MIDZ (0.43 - 0.59)	20.22 (Mpc/h)	20.54 (Mpc/h)
HIGHZ (0.59 - 0.75)	19.58 (Mpc/h)	20.02 (Mpc/h)

hand, voids with higher λ_v values (as in bin 3) equate to "voids within voids" (Sheth & van de Weygaert, 2004), predominantly smaller voids enveloped within large-scale underdensities, which present a positive κ ring around the void boundary as seen from Figure 4.3.

We also take into account the fact that the MICE footprint is significantly larger than the DES Y3 footprint and as a result, contains more voids. To assess the impact of this difference, we apply the DES Y3 mask to the MICE octant and identify the voids within this overlapping area. Subsequently, we carry out our stacking analysis using these voids. As expected, and in line with previous studies, we do not observe any substantial differences in the stacked profiles, despite the varying footprints. Consequently, we opt to use all the voids in the MICE simulation without implementing any footprint cut. This approach is consistent with the methodologies adopted by (Kovács et al., 2022, Vielzeuf et al., 2021), providing further validation to our study.

4.3.3 Filtering the CMB lensing map

When handling the CMB lensing map, we focus on lensing modes with $L \leq 2048$. This is because the lensing signals from cosmic voids are typically found on degree scales, and higher L modes mostly consist of noise rather than useful signal. While we did consider the exclusion of the largest scale modes with $L < 8$ as was done in Planck Collaboration et al. (2020b), we found that this had a negligible impact. As

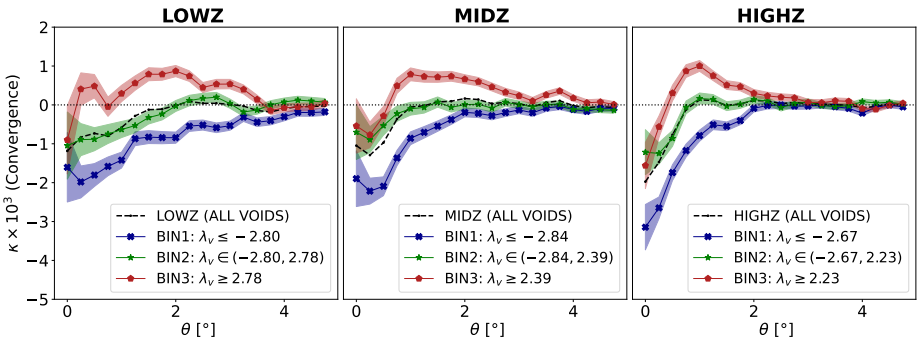

Figure 4.3: This figure presents the derived profiles from stacked images, each centered on identified `Voxel` voids within the MICE simulation. The data is segregated into three different redshift bins, and within each of these, there are three different λ_v bins. The representation thus illustrates the behaviors and properties of these `Voxel` voids across three redshift bins and different values of λ_v. The shaded areas in the figure represent 1σ uncertainty intervals, estimated through standard errors obtained from "void-by-void jackknife resampling." The dashed lines illustrate the aggregate result from all voids within the specified redshift category.

a result, we decided to exclude only the monopole and the dipole.

The key challenges in detecting the lensing signals are the lensing reconstruction noise present in the *Planck* κ map and the additional κ values contributed by unrelated structures in our line of sight. These noise sources are about ten times larger than the lensing signal from a single void, rendering it essentially invisible. Hence, our strategy involves stacking these signals together and dividing the voids based on their λ_v values. We then apply an optimized 'matched filter' to the κ map before stacking. This filter, derived from templates in the MICE simulations, combines with the original map in a way that highlights the parts of the map that match the filter, making the lensing signals stand out more.

The matched filter transforms the original lensing map, represented as κ, into a 'filtered' version, or κ^{MF}. This transformation involves convolving the filter with the original map, effectively amplifying the signals that match the filter. We created these filtered maps for each of nine different void 'bins'.

One of the key benefits of this matched filter technique is its neutrality - it is applied to the whole map uniformly so, it doesn't unfairly favor certain parts of the map over others. It also reduces the variability, or 'noise', at the locations of voids to the lowest possible level.

By comparing these measurements across all voids stacked together, we can see the benefits of our approach to split the data into bins based on λ_v values. We also find that the lensing signals are most easily detected in the two extreme λ_v bins rather than the middle bin.

To construct the matched filters, we initiate by defining the convergence field at a location $\boldsymbol{\theta}$, originating from the position $\boldsymbol{\theta}_0$ which corresponds to the κ value at the center of a void as illustrated in Figure 4.3. This is expressed as:

$$\kappa(\theta) = \kappa_{\text{template}}(|\theta - \theta_0|; \lambda_v) + p(\theta) \tag{4.4}$$

In this context, p is symbolic of the noise component in all the κ maps, excluding the void lensing signal itself. Meanwhile, the κ_{template} symbol represents the corresponding void lensing template profile, which is derived from the stacked images from MICE.

It is possible to separate this template profile as:

$$\kappa_{\text{template}}(\theta; \lambda_v) = \kappa_0(\lambda_v) k(\theta; \lambda_v) \tag{4.5}$$

$$= \kappa_0(\lambda_v) \sum_{L=0}^{\infty} k_{L0}(\lambda_v) Y_L^0(\cos\theta), \tag{4.6}$$

In the given equations, $\kappa_0(\lambda_v) \equiv \kappa_{\text{template}}(0; \lambda_v)$ is what we refer to as the 'amplitude term'. It informs us about the maximum intensity of the template profile at the void center. Furthermore, $k(\theta)$, which we call a shape function', standardizes the shape of the template profile based on the coefficients of its spherical harmonic, k_{L0}. To derive the k_{L0} coefficients, an interpolated univariate spline was employed to construct a HEALPix template map from the $k(\theta)$ measurements. This map's pixel values, calculated from spherical coordinates, were then normalized relative to the value of κ_0.

By taking these definitions into account, and making the assumption that the noise component is uniform, shows no directional bias, and averages out to zero, we are in a position to calculate the spherical harmonic coefficients for the ideal

matched filter:

$$\Psi^{MF}_{\mathrm{L0}}(\lambda_v) = \frac{\alpha k_{L0}(\lambda_v)}{C_L^{N_{\mathrm{tot}}}} \tag{4.7}$$

with α defined as

$$\alpha^{-1} \equiv \sum_{L=0}^{\infty} \frac{(k_{L0}(\lambda_v))^2}{C_L^{N_{\mathrm{tot}}}}\,, \tag{4.8}$$

where

$$C_L^{N_{\mathrm{tot}}} = C_L^{\kappa\kappa} + N_L^{\kappa\kappa}\,, \tag{4.9}$$

is the total power spectrum, and $C_L^{\kappa\kappa}$ and $N_L^{\kappa\kappa}$ are the lensing and noise power spectra, respectively, for the Planck lensing map.

The ideal matched filters for each void bin, constructed using previously acquired template profiles, are displayed in Figure 4.4. We calculate the sum in Eq. 4.8 up to $L = 700$, as the spherical harmonic coefficients for higher values of L rapidly approach zero, as seen in the figure. We have also transferred the jackknife errors from the template profiles into the matched filters.

An important takeaway from Figure 4.3 is that the templates for the λ_v bin 1 in every redshift category don't undergo a sign change, which suggests that the corresponding matched filters for these bins also stay the same. For all the remaining bins, a conspicuous crossover point is observed, resulting in filter profiles that are either partly or entirely compensated. In this context, a "compensated" profile refers to a matched filter profile where the areas under the curve with positive and negative values of kappa cancel each other out, leading to a net zero integral over the profile. This compensation phenomenon actually reflects a balance between the regions of under-density and over-density within the voids and superclusters, as captured by the lensing signal.

For each bin defined by the matched filter, based on λ_v, the lensing map which has been filtered, denoted by κ_{MF}, can be viewed as a convolution of the filter with the original map. Formally,

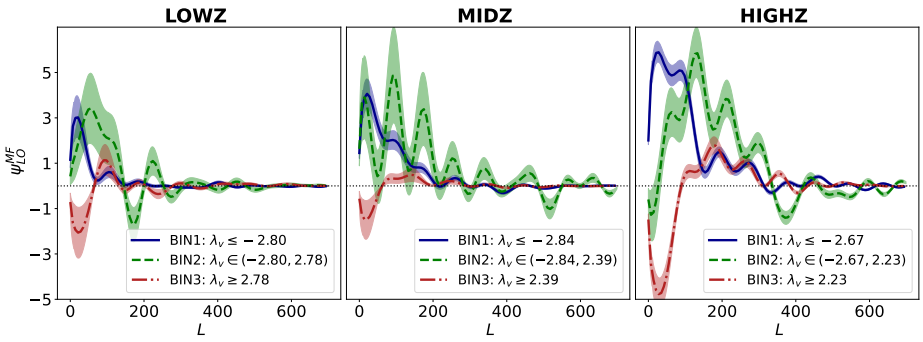

Figure 4.4: This figure shows the optimally determined spherical harmonic coefficients, known as the kernel of the matched filters ψ_{LO}^{MF}, derived from the MICE template profiles shown in Figure 4.3. The shaded regions represent uncertainty estimates calculated from 1000 synthetic datasets using jackknife standard errors, as detailed in Equation 4.15. In our analysis, we confine the application of spherical harmonics to $L = 700$, a convention based on the observation that the power of these coefficients approaches zero beyond this threshold.

$$\kappa^{\rm MF}(\eta) = \int d\Omega \kappa(\theta) \Psi^{\rm MF}(|\theta - \eta|), \tag{4.10}$$

This can also be transcribed into spherical harmonic space (Schäfer et al., 2006) as follows,

$$\kappa_{\rm LM}^{MF} = \sqrt{\frac{4\pi}{2L+1}} \kappa_{LM} \Psi_{\rm L0}^{MF}. \tag{4.11}$$

The matched filter is designed to ensure the expected value of the filtered field at the void locations is:

$$\langle \kappa^{\rm MF}(0; \lambda_v) \rangle = \kappa_0(\lambda_v), \tag{4.12}$$

such that the filter is unbiased. This is the κ_0 measured at the void center. This matched filter also minimizes the variance of the filtered field at this location, given by

$$\sigma^2_{\rm MF}(0; \lambda_v) = \sum_{L=0}^{\infty} C_L^{N_{\rm tot}} |\Psi_{\rm L0}^{MF}|^2 . \tag{4.13}$$

The maximum detection level of the optimal matched filter, for a single isolated void, can be quantified as (McEwen et al., 2008),

$$\Gamma_{single}(\lambda_v) \equiv \frac{\langle \kappa_{\rm MF}(0; \lambda_v) \rangle}{\sigma_{\rm MF}(0; \lambda_v)} = \alpha^{-1/2} \kappa_0(\lambda_v) . \tag{4.14}$$

In summary, matched filtering is applied to optimize the signal-to-noise ratio. This technique emphasizes the expected lensing signal in specific regions of the lensing map, following a predetermined template, while reducing non-relevant areas. The lensing signal, as represented by the void center pixel in the filtered map, enables a statistically optimized quantification of the lensing effect, which is suitable for stacking.

As observed in Figure 4.4, it is important to note that the power of the filter primarily lies in the L modes less than 500. This makes the final central pixel of voids susceptible to smaller-scale noise as we anticipate that high L modes are dominated by noise. This does not compromise its effectiveness but rather highlights its specificity. Given that cosmic voids are large-scale structures, it is reasonable that these L modes capture the most significant lensing information. Therefore, the efficiency of the matched filter is not predicated on capturing all possible information, but on maximizing the detectability of the specific lensing signal, assuming that the MICE template accurately characterizes this signal.

4.3.4 Error Estimation

We use the jackknife method to estimate the uncertainties in the MICE void lensing templates and their corresponding matched filters. This approach contrasts with the method used by Kovács et al. (2022) (hereafter referred to as K22), which assumes that errors in MICE are negligible. We set $N_{jk} = N_{\rm void}$ for each void bin in the MICE simulation. This process results in a jackknife sample of size $N_{\rm void}$. The standard errors of the MICE templates, as used in Figure 4.3, are given by:

$$\sigma_{\rm JK} = \sqrt{\frac{N_{\rm void} - 1}{N_{\rm void}} \sum_{i=1}^{N_{\rm void}} (\theta_i - \overline{\theta})^2} \tag{4.15}$$

where θ_i are the individual jackknife samples, $\overline{\theta}$ is the mean of the jackknife estimates, and $N_{\rm void}$ is the number of voids in that bin.

We then estimate the covariance matrix from these "void by void" jackknife

samples by using (Mohammad & Percival, 2022):

$$C_{ij}^{(jk)} = \frac{N_{\rm void} - 1}{N_{\rm void}} \sum_{k=1}^{N_{\rm void}} (\theta_{k_i} - \bar{\theta_i})(\theta_{k_j} - \bar{\theta_j}) \tag{4.16}$$

where the index k represents the jackknife samples and θ_{k_i} and θ_{j_i} are the corresponding θ measurements in the ith bin, as shown in Figure 4.3.

After this, a synthetic data vector is created as:

$$\xi_{\rm mock} = LZ + \xi_{\rm th}, \tag{4.17}$$

where $LL^T = C_{ij}$, L is obtained by a Cholesky decomposition of the covariance matrix $C_{\rm ij}$, and Z is a vector of independent standard normal random variables ($\mu = 0$ and $\sigma = 1$), and $\xi_{\rm th}$ is the mean signal template for the corresponding bin. In this way, we conserve the structure of the covariance and add random Gaussian noise by using Z, which makes our template error analysis more robust compared to previous CMB x LSS studies (Camacho-Ciurana et al., 2024, Kovács et al., 2019, Kovács et al., 2021, Vielzeuf et al., 2021)

We then obtained $N_{\rm void}$ synthetic data vectors using Equation 4.17 for each void bin and calculated the mean profile of these. This process was repeated $N = 1000$ times to obtain 1000 mean profiles. We applied our matched filter methodology to obtain the spherical harmonic coefficients based on these 1000 mean profiles, as shown in Fig 4.4.

Subsequently, we perform a convolution of these matched filters with 1000 randomly generated MICE κ maps, employing the synfast function from the Healpy library. This operation introduces an additional layer of randomness, derived from both the κ map and the coefficients of the matched filters, enabling us to observe the impact of errors in the MICE templates. Otherwise, we could have just used the mean template profile to convolve with 1000 randomly generated MICE κ maps, but we wanted to observe the effect of the uncertainty in the template profiles.

We further tested our error analysis by applying jackknife resampling to different sub-volumes and using various groupings with different N_{jk} values, such as 50, 64,

and 100, instead of treating each void as an individual jackknife sub-sample. Our findings indicated that when implementing Equation 4.17, the standard deviation of the resulting templates remained consistent across these different groupings. This consistency reinforced our decision to employ the "void by void" jackknife approach for our final error analysis. This error analysis was repeated for 2D superclusters as well.

Intriguingly, we find that the final stacked κ value emanating from the DES Y3 void centers remains unaffected by the randomness in the spherical harmonics coefficients of the matched filters. This can likely be attributed to the fact that the influence of this jackknife randomness is minimal at smaller scales, such as the center pixels of voids. We, therefore, conclude that our measurements are predominantly dominated by the noise in the Planck κ map.

We first extract κ_0 values from the randomly generated and matched filtered Planck-like convergence maps at the location of the central pixels of each bin of DES Y3 voids. We then average out these values to calculate κ_0. This process, involving 1000 random instances of κ_0, allows us to construct a covariance matrix for our measurements.

Next, we determine the κ_0 values at the central pixels of DES Y3 void positions for each bin on the corresponding matched filtered Planck map. These measured κ_0 values are subsequently compared with the corresponding MICE κ_0 values. Figure 4.5 illustrates the measured κ_0 values for each void bin, encompassing both `Voxel` and 2D voids. The standard errors incorporated into the plot correspond to the diagonal entries of our established covariance matrices.

To measure our CMB lensing detection significance, we use the χ^2 minimization technique as in Kovács et al. (2022), Vielzeuf et al. (2021). We make use of the following equation;

$$\chi^2 = \sum_{l,m} \left(\kappa_l^{\mathrm{DES}} - A_\kappa \cdot \kappa_l^{\mathrm{MICE}}\right) C_{lm}^{-1} \left(\kappa_m^{\mathrm{DES}} - A_\kappa \cdot \kappa_m^{\mathrm{MICE}}\right) \tag{4.18}$$

where κ_l denotes the mean CMB lensing signal within θ bin l, and C represents the related covariance matrix. We checked to identify the best-fitting amplitude,

represented as $A_\kappa \pm \sigma_{A_\kappa}$, by constraining the shape of the stacked convergence profile from DES Y3 x Planck to align with the shape calibrated from the MICE simulation. Moreover, in our matched filtering methodology, we apply the Percival correction factor when inverting covariance matrices as described in Percival et al. (2021). Conversely, for the covariance matrix derived from the template fitting methodology of K22, we employ the Anderson-Hartlap factor $h = (n_{\text{randoms}} - 1)/(n_{\text{randoms}} - n_{\text{data points}} - 2)$ before inverting the covariance matrix (Hartlap et al., 2007). This approach is adopted to maintain consistency with the methods utilized by K22. We then obtain the final results using the template fitting methodology of K22 as depicted in Figure 4.7.

4.4 Results

The results of our study confirm that both `Voxel` and 2D void results are in good agreement with expectation, as seen in Figure 4.5. The measured A_k values are $A_{Voxel} = 1.03 \pm 0.22$ and $A_{2D} = 1.02 \pm 0.17$. These represent a 4.61σ detection of CMB lensing in the case of `Voxel` voids, and a 5.92σ detection for 2D Voids. We attribute the marginally higher detection associated with 2D voids to their intrinsic elongation along the line of sight due to their projected nature in redshift shells. We then apply the same redshift binning to compare the results of 2D superclusters as seen in Figure 4.6, finding $A_{2D} = 0.87 \pm 0.15$, corresponding to a 5.94σ detection of CMB lensing.

4.4.1 Comparison with K22 Voids

In order to understand the differences that the employed method and type of tracers can make, we compare our results with K22 (Kovács et al., 2022). K22 uses the same dataset and simulation as in our study. The difference lies in our updated *redMaGiC* algorithm to select the galaxies both in DES Y3 and the MICE simulation.

In addition, we use the matched filtering method, and we do not re-scale when stacking the CMB cutouts around voids. However, to investigate if the employed method makes a significant difference in the results, we also use the same method

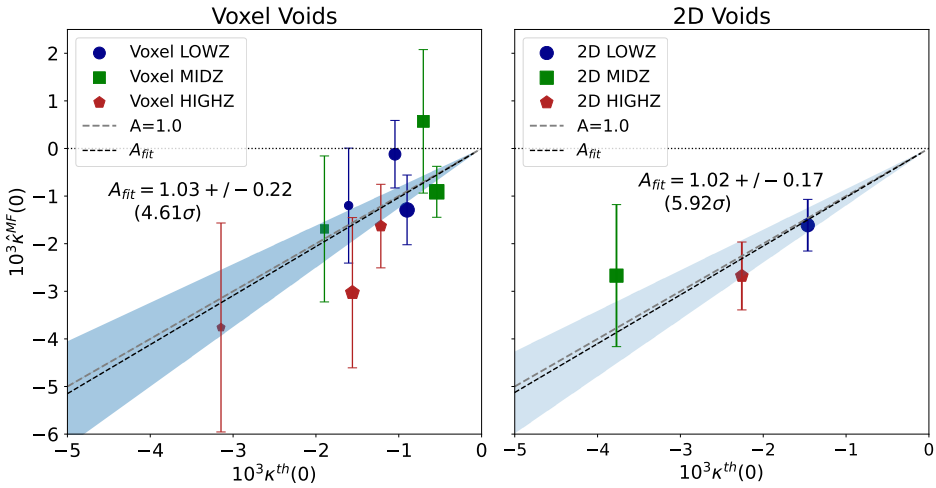

Figure 4.5: Comparison of `Voxel` and 2D Voids: This figure illustrates the correlation between the CMB lensing convergence (κ) derived from the Dark Energy Survey Year 3 (DESY3) and Planck data, and the simulated void lensing κ from the MICE simulation at the stacked center pixels of voids. Each redshift bin (LOWZ, MIDZ, and HIGHZ) is represented by different markers. Within each redshift category, the bin values of λ_v increase from the smallest to the largest. The plots include a reference line at $A_k = 1.0$ and the best-fit line. Our analysis reveals a significant correlation between DESY3 and MICE data, with best-fit amplitudes of $A_k = 1.03$ for `Voxel` voids and $A_k = 1.02$ for 2D voids, corresponding to 4.61σ and 5.92σ detection levels for CMB lensing in voids, respectively. These findings show a strong agreement with ΛCDM expectations.

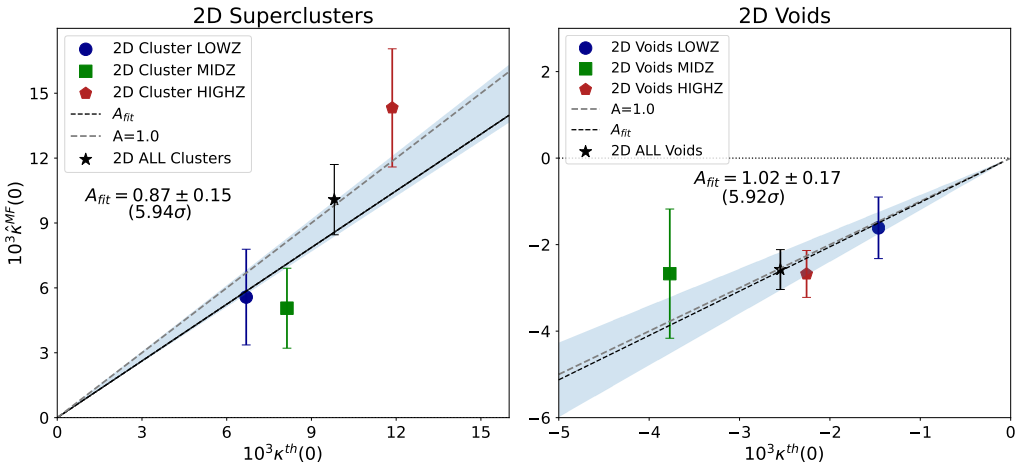

Figure 4.6: Comparative Analysis of 2D superclusters and 2D Voids: This figure presents stacked κ_0 values for each redshift bin of both 2D superclusters and 2D voids. Our joint fit utilizing different redshift categories yields a statistical significance of 5.94σ and an amplitude of $A_k = 0.87 \pm 0.15$ for 2D superclusters, while for 2D voids we find a statistical significance of 5.92σ and an amplitude of $A_k = 1.02 \pm 0.17$. The amplitude A_k observed for 2D superclusters is slightly lower than that for 2D voids, but still falls within 1σ of $A_k = 1.00$. These results are in line with Hang et al. (2021), which also found that 2D superclusters exhibit a slightly lower A_k value than their void counterparts. However, it's important to note that our measured A_k values imply a good agreement with $A_k = 1.00$, while Hang et al. (2021) demonstrate a marginally lower lensing amplitude for voids and superclusters.

as in the K22 study, rescaling the stacked CMB cutouts around void centers and filtering the CMB lensing maps with a Gaussian filter with a size Full Width at Half Maximum (FWHM) = 1°.

To determine the covariance matrix for this measurement, we generate 1000 random Planck maps in the same way as for our matched filtering approach, and repeat the Gaussian filtering and the re-scaled stacking of DES Y3 voids and superclusters, as carried out in K22. To estimate the lensing amplitude, we employ equation 4.18, consistent with our matched filtering methodology. The templates and observed signals are shown in Figure 4.7, and we find amplitudes $A_\kappa = 0.88 \pm 0.14$ (a 6.30σ detection of the lensing signal) for 2D voids, and $A_\kappa = 0.94 \pm 0.13$ (a 7.16σ detection) for 2D Clusters. Compared to the results of K22, who report values of A_κ lower than the MICE expectation at around the $\sim 2.3\sigma$ level, our results are perfectly consistent with $A_\kappa = 1$. The statistical uncertainty in our results is slightly larger than that of K22, although very compatible. We associate this difference between our result and that of K22 with the updated and improved *redMaGiC* galaxy sample, which affected both the Y3 data and the MICE mocks.

We further tested changing the cut used to define the superstructure sample, from $R_v < 20h^{-1}$Mpc as used by K22 to $R_v < 15h^{-1}$Mpc instead. This cut naturally substantially increases the number of 2D voids and 2D superclusters in the final sample, and leads to a reduction in the measurement uncertainties of $\sim 15\%$ in each case, while leaving the A_κ central values essentially unchanged. This suggests that the K22 size cut is not optimal, but we leave a fuller investigation of optimisation of the signal-to-noise to future work.

4.5 Discussion and Conclusion

In this study, we conducted an in-depth examination of superstructures and their interrelation with the CMB lensing, zeroing in on a pivotal instrument for the detection of the CMB lensing effect: the matched filter technique.

For the first time in the literature, we applied the `Voxel` void-finding algorithm to photo-z galaxies and gauged their CMB lensing footprints.

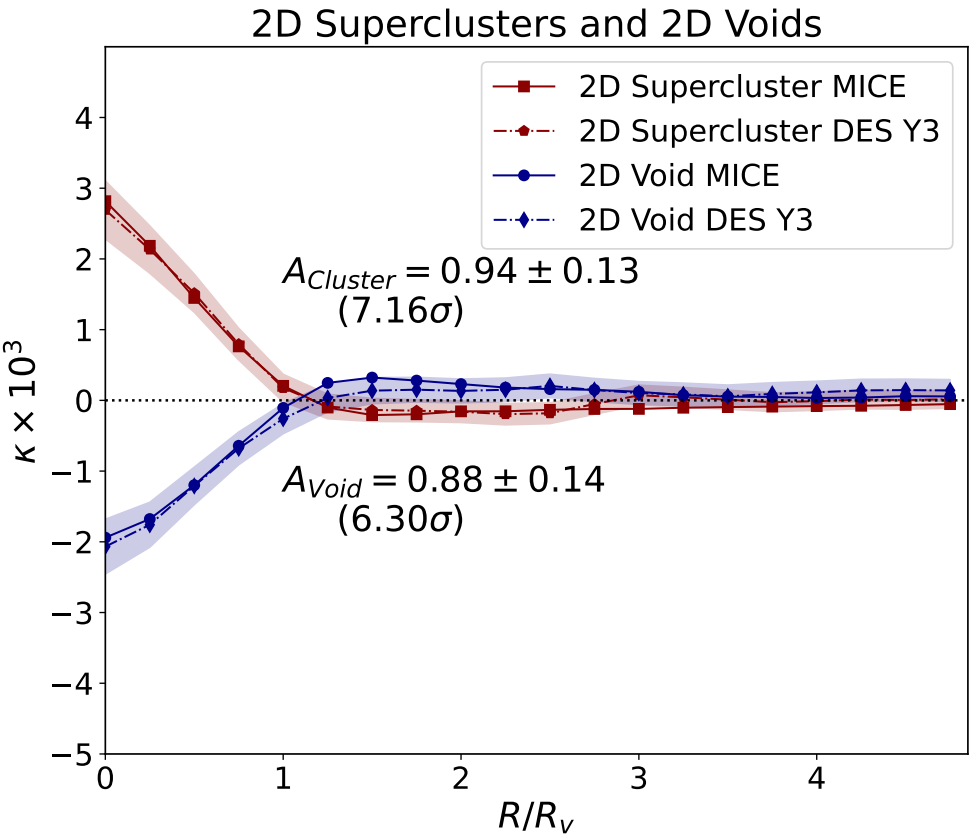

Figure 4.7: Stacked profile of 2D voids and 2D superclusters with the template fitting methodology from K22. The 2D superstructures with radius $R_v < 20h^{-1}$Mpc are not included in the analysis in accordance with K22.There is no further binning applied. The stacked images are obtained by rescaling the image up to $5R_v$ centered on void positions. We then measured the radial kappa profile from the final stacked images. The shaded regions show the 1σ error bars from the covariance matrix as explained in Section 4.4.1.

The CMB lensing footprints of cosmic voids, sourced from both the DES Y3 dataset and the MICE simulation for `Voxel` and 2D voids, demonstrated a robust agreement. This revelation provides compelling insights into the intricacies of delineating superstructures. It highlights the significance of not only the methodologies employed but also the noise properties associated with CMB lensing map and the choice of galaxies utilized in their definition.

Our results indicate a slight divergence from the weaker signal reported for DES Y3 voids in the study by Kovács et al. (2022), but align well with the findings for DES Y1 voids by Vielzeuf et al. (2021). The disparity with the previous DES Y3 results is primarily attributed to the enhancements made in the *redMaGiC* galaxy selection algorithm employed in our investigation. It became evident that the selection of tracer galaxies used to define superstructures wields a considerable influence on the CMB lensing outcomes of these, independent of the methodology employed in identifying the superstructures.

Our research emphasized significant observations of lensing stemming from `Voxel` voids, 2D voids, and 2D clusters, each uniformly demonstrating an amplitude consistent with $A_k = 1.00$. Such uniformity across a variety of void types and structures not only reinforces the robustness of our findings but also aligns with the predictions of the ΛCDM cosmological model, agreeing well with the results of previous studies (Cai et al., 2017, Camacho-Ciurana et al., 2024, Hang et al., 2021, Raghunathan et al., 2019, Vielzeuf et al., 2021).

Furthermore, we identified a notable correspondence between 2D and 3D (`Voxel`) voids in our study, where the 2D voids exhibited marginally lower uncertainties and enhanced levels of CMB lensing detection. This observation indicates the superior precision of 2D void analysis in capturing lensing signals. Such precision is presumably owed to the elongated structure of 2D voids along the line of sight, which are defined on projected tomographic redshift slices. The 2D algorithm finds structures elongated along the line of sight because they result in a big impact on the projected density field but structures aligned perpendicular do not. This structural characteristic possibly contributes to the increased sensitivity in detecting lensing phenomena which is the integral effect along the line of sight, further validating the

efficacy of employing 2D void analysis in studies of this nature.

Moreover, we demonstrated that `Voxel` voids can be effectively utilized for analyses involving the cross-correlation of lensing effects on the CMB. This study is the first to measure the CMB lensing imprints of `Voxel` voids. Our results provide evidence that these voids exist in regions of the Universe characterized by a true deficit in matter density as shown by their CMB lensing imprints. Encouragingly, our results align closely with those derived from 2D voids, a void finder methodology employed extensively in previous studies. Furthermore, as demonstrated by Radinović et al. (2024), `Voxel` voids serve as a viable choice for void-galaxy correlation analyses. Unlike 2D voids, whose tomographically projected nature precludes this type of analysis, `Voxel` voids do not suffer from this limitation. This key advantage makes `Voxel` voids particularly suited to forthcoming large-scale surveys such as the Dark Energy Spectroscopic Instrument (DESI) (DESI Collaboration et al., 2016a,b) and the Euclid mission (Laureijs et al., 2011).

In our comparison of the matched filter and Gaussian filtering methods, we observed consistent results for $A_k = 1.00$ across 2D voids and clusters, as detailed in Kovács et al. (2022), Vielzeuf et al. (2021). Our study demonstrated that the matched filter method can provide more precise A_k estimates, suggesting its potential for future research. In particular, it can be interesting to utilize the matched filtering method on the same dataset used in Kovács et al. (2022) to examine the detected ISW signals. The authors of the cited study reported an excess ISW signal without using matched filtering, which presents an intriguing opportunity for future analysis and verification of their claim.

In the near future, the final processed data of the full six years of DES observations will be available for such analyses. The DES Y6 dataset covers the same footprint as the Y3 data used here, but is deeper and thus has a factor of $\sim 2.3\times$ higher number density of galaxy tracers. Given the fixed footprint, we expect only a small change in the number of 2D voids in Y6, as these are less sensitive to the galaxy number density. In contrast, for `Voxel` voids, the number of voids is expected to change roughly proportional to the change in the tracer number density, so we expect a factor of $\sim 2.3\times$ increase in the number of voids for Y6. However,

this does not translate to a simple $1/\sqrt{N_{\rm voids}}$ reduction in the statistical uncertainty, because the nature of individual voids found also changes as the galaxy number density increases, with smaller voids being resolved. This means that the expected signal strength also changes. A full accounting of the net effect on the expected SNR requires dedicated studies using Y6 mocks.

This work provides the pivotal groundwork for upcoming studies from the Vera Rubin Observatory and the Euclid Survey, which aim to further investigate the Integrated Sachs-Wolfe (ISW) effect and CMB lensing due to cosmic superstructures. Our research not only contributes to the evolving understanding of lensing phenomena in the Universe but also lays a strong foundation for future studies. By applying the insights discussed in our analysis, future large-scale structure surveys can refine their strategies for exploring the universe's large-scale structure, potentially leading to enhanced accuracy and precision in cosmological constraints derived from these measurements.

Chapter 5

Discussion and Conclusion

In this thesis, the CMB lensing imprints of cosmic voids and superclusters are tested against ΛCDM predictions by using N-body simulations. We used 2D and `VIDE` voids from DES Y1 dataset and showed that they are in good agreement with predictions using MICE simulation and template fitting method with Gaussian filtering of the CMB. We showed how different Gaussian beam sizes affect the signal. We then cross correlated voids in DES Y3 dataset with weak lensing mass maps to show the consistency of different mass map making methods. We used three different void types and showed their effect on different mass maps. We then used optimal matched filtering method and apply it to `Voxel` voids identified in DES Y3 data set. For consistency, we also used 2D voids and apply both matched filtering and the template fitting method.

When considering additional findings from the DESI Legacy Imaging Survey DR8 (Hang et al., 2021) and Pan-STARRS (Camacho-Ciurana et al., 2024), which leverage the advantages of a full-sky survey, it is also important to note that an upcoming study by Sartori et al. (in preparation) using Legacy Imaging DR9 LRGs is expected to be published shortly and their preliminary results also show good agree with ΛCDM model as well by employing template fitting method and Gaussian filtering. In comparison, our research employs the matched filter methodology as also used in Raghunathan et al. (2019), wherein the authors use BOSS data. Morevoer, Vielzeuf et al. (2021) also shows good agreement with ΛCDM albeit lower detection significance. These collective findings are comprehensively illustrated in

Figure 5.1. These results show that different surveys by using different simulations generally find good agreement with theoretical ΛCDM predictions.

An important observation from Figure 5.1 is that supercluster CMB lensing amplitudes are mildy weaker than expectations in comparison to voids. Although consistent within 1σ in Demirbozan et al. (2024), this behavior is more prominent in Hang et al. (2021) and in Kovács et al. (2022). This behaviour potentially require additional research to confirm by changing supercluster definitions as opposed to using inverted 2D finder.

A particular concern whether the matched filter predominantly detects "expected signals" as calibrated by simulations or behaves like a Bayesian prior. However, the fundamental principle of the matched filter is to identify a predetermined (ΛCDM template) signal within background noise under the assumption of isotropic noise distribution. The most important feature of this method is its minimal parameter dependence, relying only on the template signal that is being searched within the embedded data. In contrast, Gaussian smoothing techniques have to specify the Gaussian beam size, thereby introducing additional parameters into the analysis.

In Chapter 3, different types of voids were shown to imprint distinct stacked profiles on mass maps. Similarly, Chapter 2 demonstrates that this variation is also evident in stacked CMB lensing profiles. These results show the importance of using multiple void finders on the same dataset to improve the robustness of the results. Using multiple void-finding algorithms on the same dataset can significantly benefit future void studies by providing more comprehensive results.

It should be noted that although ISW expectations are generally weaker than CMB lensing signals, the ISW-void anomaly claimed by Granett et al. (2008) and Kovács et al. (2022) is significantly stronger than the mild void × CMB lensing tension reported by Kovács et al. (2022). This discrepancy is further supported by findings in Cai et al. (2017), where superlarge voids (ZOBOV definition) exhibit mildly excess signals, albeit with lower detection significance compared to Kovács et al. (2022), while the CMB lensing signals for the same voids were entirely consistent with theoretical expectations. Furthermore, Hang et al. (2021) reported hints of a clearer ISW signal with increasing R_v (2D definition), potentially due to

the lower noise levels in large-scale void stacks. It is therefore important for future studies with more data to investigate the void size dependence of ISW and CMB lensing effects.

On this note, some studies analyze void ISW/CMB lensing signals in the context of the general tensions related to the ΛCDM model. In particular, Naidoo et al. (2024) proposes a model with an evolving dark matter equation of state, where void-ISW signals are enhanced, void-CMB lensing signals are somewhat weaker, and both the H_0 and S_8 tensions can be alleviated (Abdalla et al., 2022).

One of our more prominent finding is that void x CMB lensing signals presented in Chapter 2 and Chapter 4 both dominated by noise in κ maps. This shows that the data from South Pole Telescope , Simons Observatory and Atacama Cosmology Telescope can significantly increase the detection significance of these studies. The data from these CMB surveys when combined with Euclid and Vera Rubin data can refine the data presented in Figure 5.1 may significantly improve the precision to test concordance cosmological models by using CMB x LSS techniques.

5.1 Limitations

In comparison to the findings of Raghunathan et al. (2019), which used a spectroscopic galaxy sample (CMASS from Reid et al. (2016)) with approximately 7300 voids over 10000 $\deg^2$, Demirbozan et al. (2024) used the `Voxel` voids and identified a significantly higher number density of voids (33427 in 4200 $\deg^2$), resulting in higher density even after accounting for a thicker redshift range (`redMagic` $0.2 < z_{\rm redmagic} < 0.75$ and $0.43 < z_{\rm CMASS} < 0.7$).

This disparity arises primarily from two key factors. Firstly, the halo masses probed by the CMASS sample ($\sim 5\times10^{13}\,M_\odot$) are substantially higher than the ones probed by the redMaGiC sample ($\sim 2\times10^{13}\,M_\odot$) used in our analysis. Given the steepness of the halo mass function, lower mass halos are inherently more abundant, leading to the identification of a greater number of voids in our higher-density galaxy catalogue. Secondly, as detailed in Section 1.6, the `Voxel` algorithm is specifically designed to efficiently work on irregular survey masks which both DES and CMASS

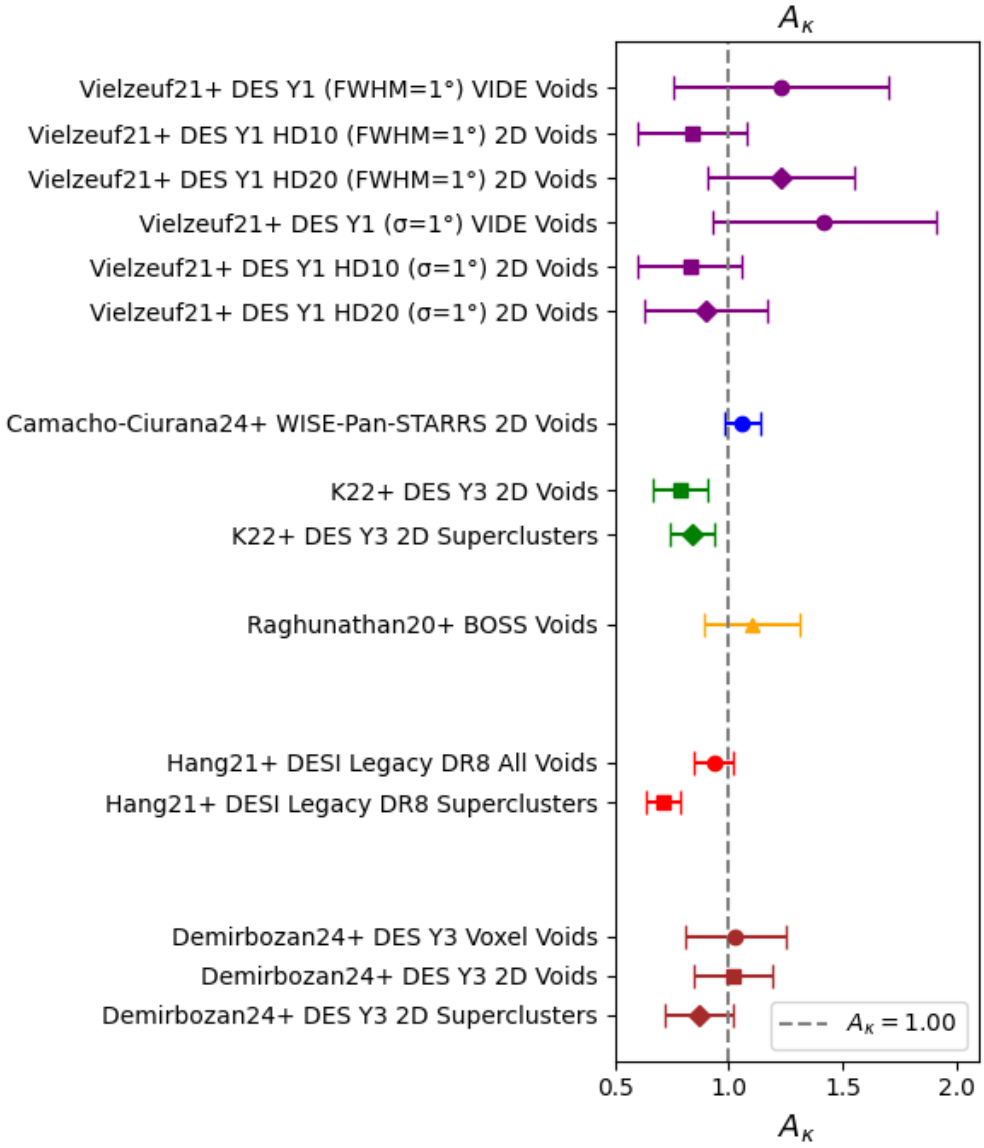

Figure 5.1: Comparison of all results presented and discussed in this thesis. DES Y3, BOSS, and WISE Pan-STARRS, with their extensive sky coverage relative to DES Y1, provide improved constraints on A_k. Among these surveys, Pan-STARRS achieves the tightest constraints, primarily due to its near full-sky coverage. When combined, the results from BOSS, Pan-STARRS, DESI Imaging Legacy Survey, and DES Y3 (Demirbozan24) exhibit good agreement with the ΛCDM model as calibrated by various simulations and different surveys. Moreover, superclusters demonstrate a slightly weaker amplitude compared to voids, as evidenced by the findings of Demirbozan24, Hang21, and K22. All three studies utilize an inverted 2D void finder to identify superclusters and this technique may not be optimal to identify superclusters.

datasets suffer from.

On the other hand, ZOBOV-based algorithm used by Raghunathan et al. (2019) needs the exclusion of voids from a substantial portion of the survey volume to account for boundary contamination issues. However, this is less of an issue in the `Voxel` approach. Therefore, `Voxel` voids result in higher number density of voids as well as reducing the incidence of false positives within the void sample.

It is also important to note that, as discussed previously, Raghunathan et al. (2019) used 108 realizations of Takahashi simulations to derive the mean CMB lensing template profile of stacked voids. This increaases the robustness of the mean lensing profile, which is then used to construct the corresponding matched filter. In contrast, DES studies (Demirbozan et al., 2024, Kovács et al., 2022, Vielzeuf et al., 2021) rely on a single realization of the MICE simulation. Moreover, Camacho-Ciurana et al. (2024) employs the WebSky simulation (Stein et al., 2020), which also consists of only one realization. Making use of multiple realizations of the same simulation accurately models the error estimation inherent in the mean stacked template and this approach should be preferred for future studies if possible.

Another consideration is that, instead of using DES `redMagic` sample in our analysis. For further robustness, MagLim galaxy sample from DES can be used for void analysis (Giannini et al., 2024, Porredon et al., 2021). The DES Y3 MagLim dataset includes up to 10 million galaxies, and comparing the results obtained from this sample with the findings presented in this thesis would be beneficial as MagLim has higher number density albeit larger redshift errors. Furthermore, the inclusion of CMB lensing maps from the South Pole Telescope (SPT) and the Atacama Cosmology Telescope (ACT) is advantageous, as these datasets overlap with DES in the regions covered by their observations (Madhavacheril et al., 2024, Pan et al., 2023, Qu et al., 2024, Shaikh et al., 2024). Using these CMB lensing maps would be additional cross check of the results in this thesis (Madhavacheril et al., 2024, Pan et al., 2023, Qu et al., 2024, Shaikh et al., 2024).

5.2 Future Research Directions

In this section, we explore potential research directions that can be pursued using the methods and techniques presented in this thesis. As explained in preceding chapters, cosmic voids serve as highly beneficial tools with considerable potential for revolutionary research in modern cosmology. One particularly promising avenue is the integration of rapidly advancing Artificial Intelligence (AI) methodologies into void studies.

For instance, Cousinou et al. (2019), Hawken et al. (2020) employed neural networks and boosted decision trees to differentiate between genuine cosmic voids and spurious ones. Additionally, Wang et al. (2023) explored the application of machine learning algorithms to extract cosmological constraints from void characteristics, successfully refining the estimations of Ω_m, σ_8, and n_s with their best models. The mean relative errors were determined to be 10%, 4%, and 3%, respectively, without the need for spatial information from the void catalogs.

Given the necessity of having full-sky void catalogs to probe the claimed ISW anomalies by voids, Storey-Fisher et al. (2024) full-sky Quasar catalogue can be an interesting choice. The Quaia catalog is an all-sky quasar catalog compiled from over 6.6 million quasar candidates identified by the Gaia mission (Gaia Collaboration et al., 2016), enhanced with redshift estimates and refined using unWISE (Lang, 2014) infrared data and proper motion filters. It boasts the largest comoving volume of any existing spectroscopic quasar sample, with a rigorous selection process that significantly reduces contaminants and improves redshift accuracy, making it a robust resource for cosmological studies.

For example, Manzotti & Dodelson (2014) used quasars from NRAO VLA Sky Survey (NVSS) (Condon et al., 1998) as fair tracers of the matter density matter field to map the ISW effect using cross-power spectrum. NVSS tracers have also been used in Ho et al. (2008) to measure ISW effect (ISW detection > 4σ). This is because NVSS tracers (i.e quasars) exhibit significant power and are detectable, particularly in the radio spectrum, at high redshifts. Consequently, they are good candidates to serve as probes of the extensive gravitational potential wells during

the initial phase of the dark energy-induced accelerated expansion of the universe, leading to the generation of the ISW effect.

Although quasars are promising candidates for tracing the gravitational potential, Hawken et al. (2020) showed that the QSO void sample is highly contaminated with spurious voids mainly due to their sparsity. Nevertheless, Kovács et al. (2022) reported the detection of a high-redshift ISW effect using eBOSS DR16 quasars. The number density of quasars remains roughly consistent between eBOSS DR14 and DR16 (Hawken et al., 2020). However, more recent findings by Curtis et al. (2024) indicate that up to 25% of void galaxies are QSOs (more than their high density counterparts), which may hinder the accurate tracing of dark matter distribution. Nevertheless, a full-sky analysis from QUAIA identified voids that hold significant potential for CMB lensing and ISW studies. Crittenden & Turok (1996) already demonstrated theoretically that a deep full-sky survey could detect the ISW effect with a signal-to-noise ratio of 7.6.

For example, an intriguing research direction involves the using of advanced machine learning techniques to harness the high-density, albeit partial-sky dataset obtained from DES LRGs. These LRGs exhibit the necessary sensitivity for accurate identification of cosmic voids with their high density and low photo-z error. Focusing on the overlapping regions between the QUAIA quasar catalog and DES data, we propose using the QUAIA catalog as a primary training dataset. By fine-tuning the model with insights derived from the observed DES voids, it could be possible to substantially improve QUAIA's capability in detecting voids in comparison to use void finder only on QUAIA data. This enhanced model could then be applied across the entire QUAIA dataset to compile a comprehensive, full-sky quasar-void catalog. Such a catalog would be invaluable for cross-correlation studies between CMB and LSS, particularly for investigating subtle ISW effect.

Similar to the methodology proposed for the DES-QUAIA data, it could be advantageous to combine high-resolution observations from the SPT and ACT with the extensive, although lower-resolution, datasets from the Planck survey. The application of machine learning techniques has demonstrated considerable efficacy in the analysis of CMB data, notably in tasks such as foreground cleaning (Petroff et al.,

2020, Yan et al., 2023). Investigating various deep learning methodologies, particularly super-resolution techniques using Convolutional Neural Networks (CNN) (Dong et al., 2014, Ledig et al., 2017a), has significant potential to improve data resolution. The super-resolution deep learning techniques have also been employed in cosmological simulations to increase the resolution of dark matter halos (Li et al., 2021).

Furthermore, Generative Adversarial Networks (GANs) (Goodfellow et al., 2014, Ledig et al., 2017b) have been effectively employed in the generation of CMB lensing maps, presenting an alternative to conventional quadratic estimator techniques (Li et al., 2022). The incorporation of these advanced methodologies could help exploit the Planck data with much detailed information. Such a CMB lensing or temperature map would definitely help CMB x LSS studies in the future.

Several studies have examined the assumption of isotropy in the cosmological principle through the analysis of galaxy clusters (Migkas, 2024). For instance, Colin et al. (2019) argued that the observed cosmic acceleration exhibits an alignment with the CMB dipole, providing evidence at the 1.4σ level against isotropic acceleration. This finding is further supported by Hu et al. (2024), who analyzed the Pantheon+ SN dataset and identified indications of anisotropy. However, Tang et al. (2023) conducted a similar analysis using the same dataset and found results consistent with cosmic isotropy, though they noted some evidence for anisotropy at lower redshifts. Furthermore, Secrest et al. (2021) analyzed a sample of 1.36 million quasars and identified a dipole in their number density, presenting a significant deviation from the expectation of cosmic isotropy.

It would be intriguing to map the full-sky ISW effect and test its isotropy by utilizing superstructures. Both template fitting with Gaussian filtering and matched filtering methods could be employed for this purpose. A key challenge, however, is that the ISW signal dominates on large angular scales (low multipoles), which are heavily influenced by cosmic variance. Nevertheless, the multipole range $10 < L < 50$ offers a promising "golden" region for precise measurements. Voids are particularly well-suited for these studies as they are relatively free from non-linear and complex gravitational effects that can complicate analyses in superclusters. In

such a study, it would be valuable to compare the differences between CMB lensing and ISW signals from the same void set. Voids could be grouped by redshift and position on the sky, ensuring that each group shares a similar gravitational potential. REVOLVER's λ_v is a perfect parameter to group voids for this purpose. These groups would ideally produce the same CMB lensing imprint and, assuming cosmic isotropy, should exhibit the same ISW imprint if cosmic acceleration is uniform in all directions. Such an approach holds great potential for providing a robust measure of cosmic acceleration. Additionally, tomographically probing both the CMB lensing and ISW imprints of these grouped voids, which share similar gravitational potentials, may aid in the extraction of cosmological parameters. Several studies have attempted to derive cosmological parameters from the CMB lensing signal of voids (Chantavat et al., 2017). However, to date, no study has explored how the ratio of the CMB lensing to the ISW effect of voids changes with redshift or used this ratio to extract cosmological parameters. Investigating this could be an interesting avenue for future research.

Furthermore, as explored in this thesis, different void finders are effective for different studies. The void size function, density, and the identified number of voids change quite substantially with the choice of void finder. We have shown that 2D void finders are effective for extracting high S/N from CMB lensing studies. However, their assumption of a circular shape is not well-founded, as voids are not inherently circular, and this approximation can oversimplify their true geometry. At this point, one may think of using density contours to define these 2D voids. Nonetheless, some analysis choices regarding the redshift slice thickness, smoothing parameters, and overlap fraction with the survey footprint still need to be made. Despite these considerations, this updated 2D void finder can provide significant improvements when stacking multiple voids and can potentially enhance S/N of measurements.

List of Figures

List of Tables

Appendix A

Additional Figures

Additional figures related to main content are shown. Figure A.1 taken from Vielzeuf et al. (2021) below shows the 2D void numbers identified in the MICE simulation with the DES Y1 footprint applied to two independent locations within the MICE octant. See Figure A.2 for the size distribution of `Voxel` voids and Figure A.3 for their correlation matrix.

We also present some results that were not included in Demirbozan et al. (2024). Figure A.4 shows the redshift distribution of 2D voids as described in Kovács et al. (2022) (K22), while Figure A.5 displays the redshift distribution of 2D voids from Demirbozan et al. (2024) (D24). It is clearly seen that the general trends between the two do not agree. Figure A.6 illustrates how the number of 2D voids changes when using the DES Y6 v0.8.6 `redMaGiC` catalogue compared to the DES Y3 v0.5.1 catalogue. Figure A.8 shows the results when our pipeline is applied to a $10^\circ \times 10^\circ$ fixed patch instead of rescaling and repeating the entire process. Furthermore, Figure A.9 demonstrates that, instead of the usual $R_v > 20, h^{-1}$, Mpc cut used in K22 and D24, using a more permissive $R_v > 15, h^{-1}$, Mpc cut increases the S/N ratio. This indicates that the less stringent cut may be more advantageous for future analyses.

Based on Figure A.9 and Figure 4.7, we estimate χ^2/dof values for voids and superclusters. This is given in Table A.1.

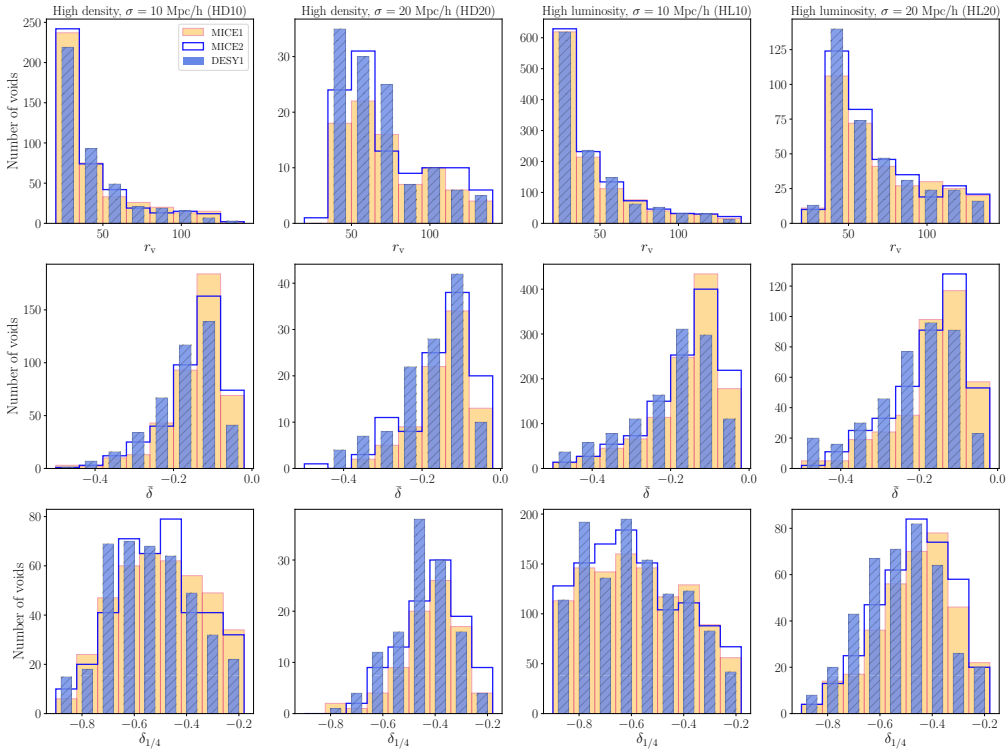

Figure A.1: Comparison of the 2D void catalogue characteristics constructed in simulated MICE1 and MICE2 (orange bars and blue steps) and observed DES Y1 samples (blue bars) across different void catalogue versions (HD10, HD20, HL10, HL20). We present results for the high-density sample (first and second columns) and the high-luminosity sample (third and fourth columns) using void finder smoothing scales of 10 Mpc/h and 20 Mpc/h.

	$R_v > 20$ Mpc/h	$R_v > 15$ Mpc/h
2D superclusters	1.23	1.32
2D voids	0.93	0.87

Table A.1: χ^2/dof values for 2D superclusters and 2D voids for different radius threshold.

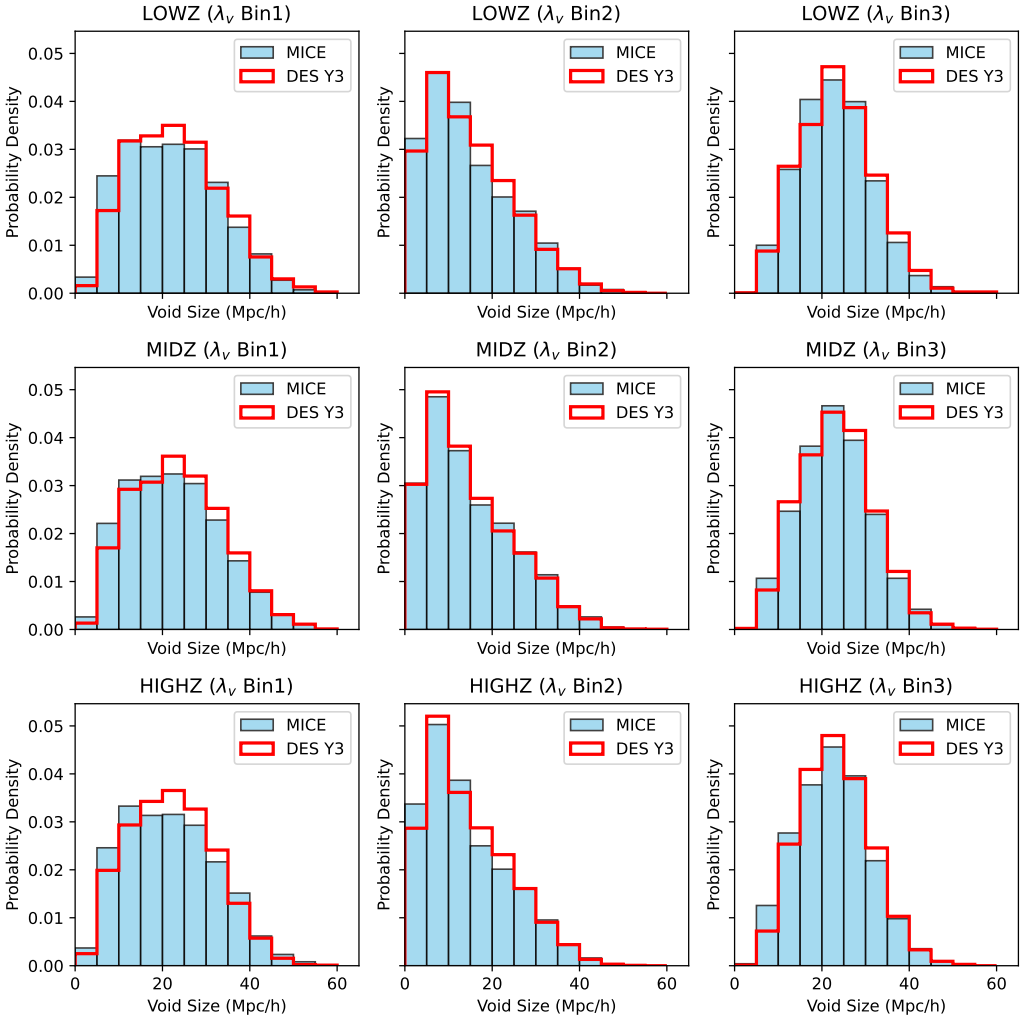

Figure A.2: This plot illustrates the `Voxel` void size distributions for both MICE and DESY3 using a normalized histogram, segmented across 9 redshift bins. Notably, the number of voids inreases with increasing redshift bin. Additionally, voids within the same λ_v bins, yet across differing redshift bins, exhibit a consistent size distribution pattern. This consistency emphasizes the functional relationship between λ_v and R_v, as shown in Equation 4.3.

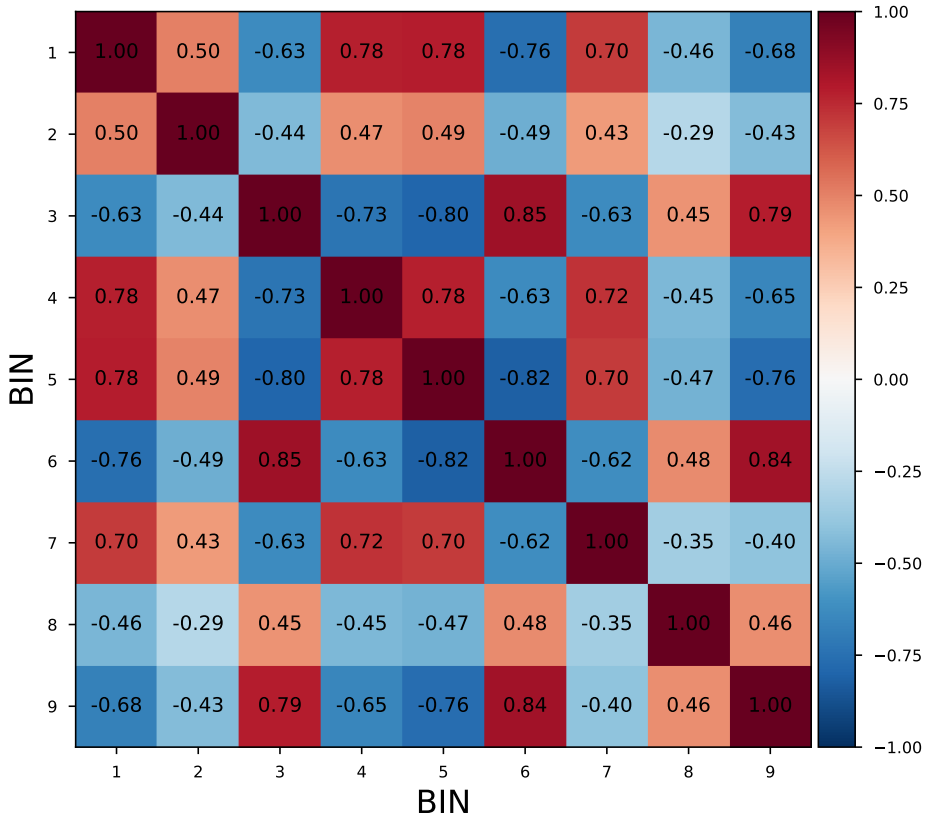

Figure A.3: This figure shows the correlation matrix of CMB lensing measurement from 9 `Voxel` bins. The bins range from BIN 1, representing LOWZ λ_v Bin 1, to BIN 9, representing HIGHZ λ_v Bin 3.

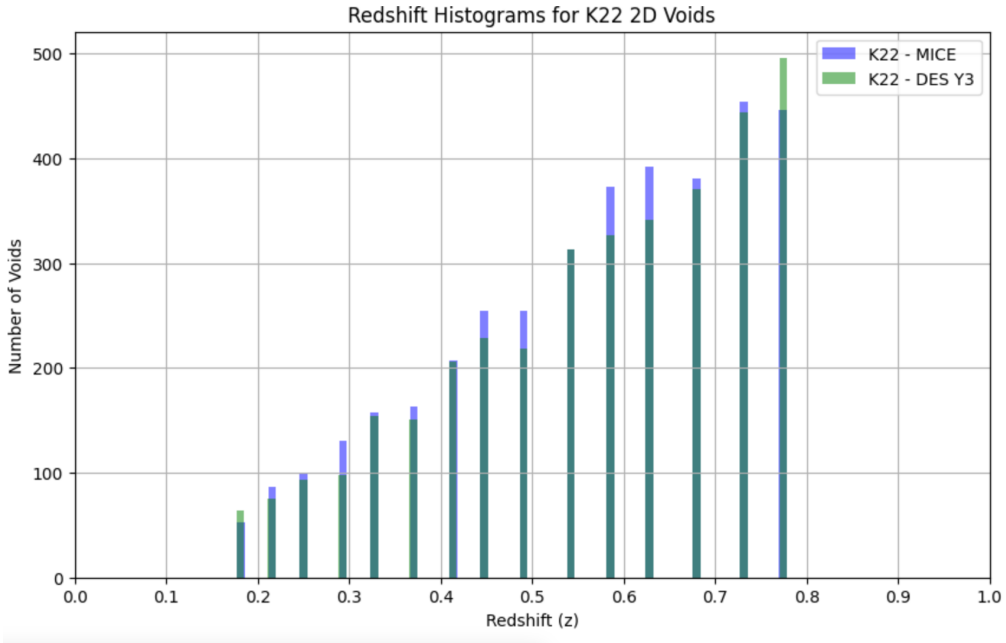

Figure A.4: This figure compares the 2D void redshift distribution from Kovács et al. (2022). There is a clear discrepancy between the MICE and DES Y3 2D void distributions. After applying our code pipeline to these voids, We obtain the best-fit value of $A_\kappa = 0.71 \pm 0.11$, which indicates an even stronger tension (lower lensing amplitude) than originally reported by Kovács et al. (2022).

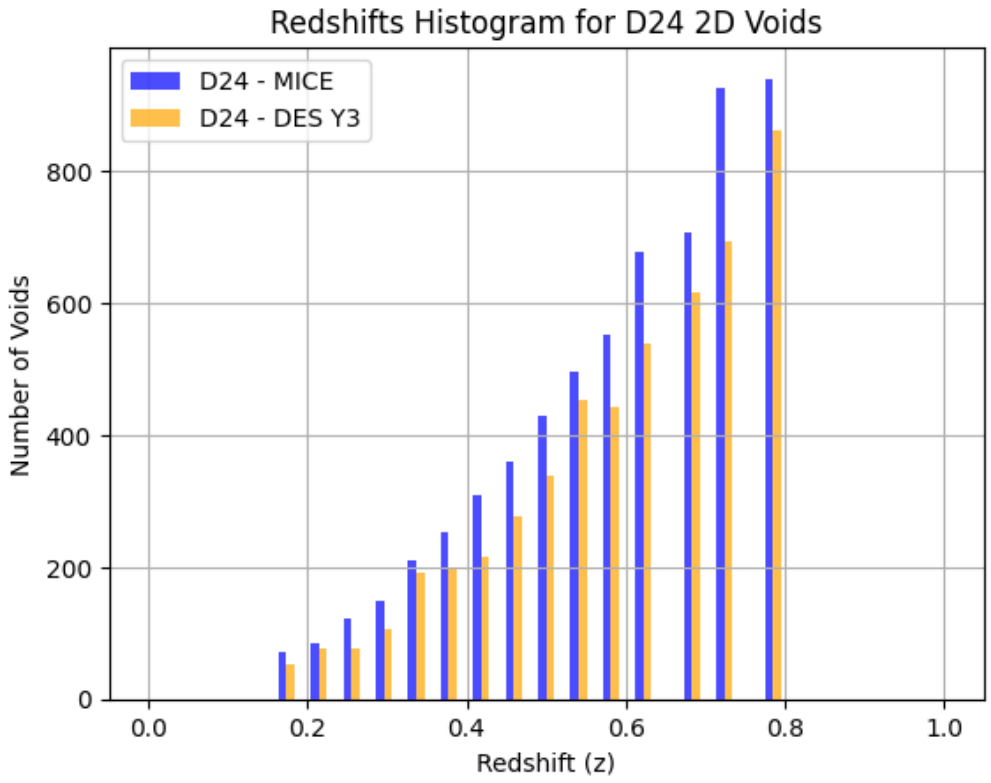

Figure A.5: Comparison of 2D void redshift distributions between MICE simulation and DES Y3 data, as presented in Demirbozan et al. (2024). The observed trends are consistent with expectations from the differing sky coverages of MICE and DES Y3. These differences and their implications are thoroughly discussed in Demirbozan et al. (2024).

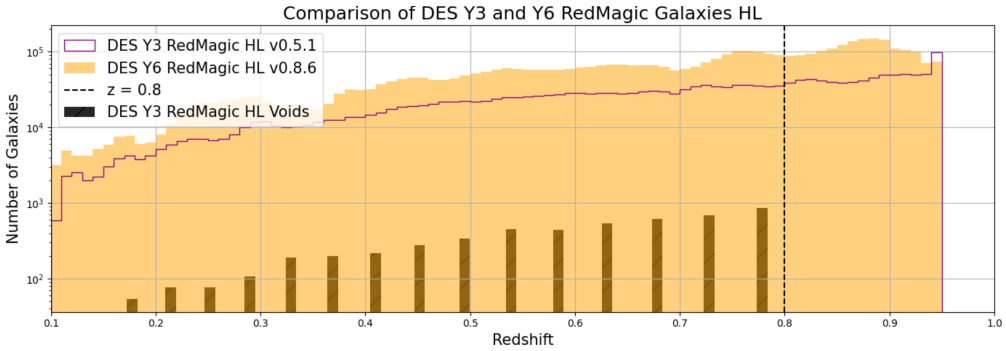

Figure A.6: This figure illustrates the changes in the number density distribution of `redMaGiC` galaxies between DES Y3 and DES Y6 datasets. The primary modification from Y3 to Y6 involves an updated selection function, while the redshift range remains constant. For comparison, 2D DES Y3 voids are also plotted.

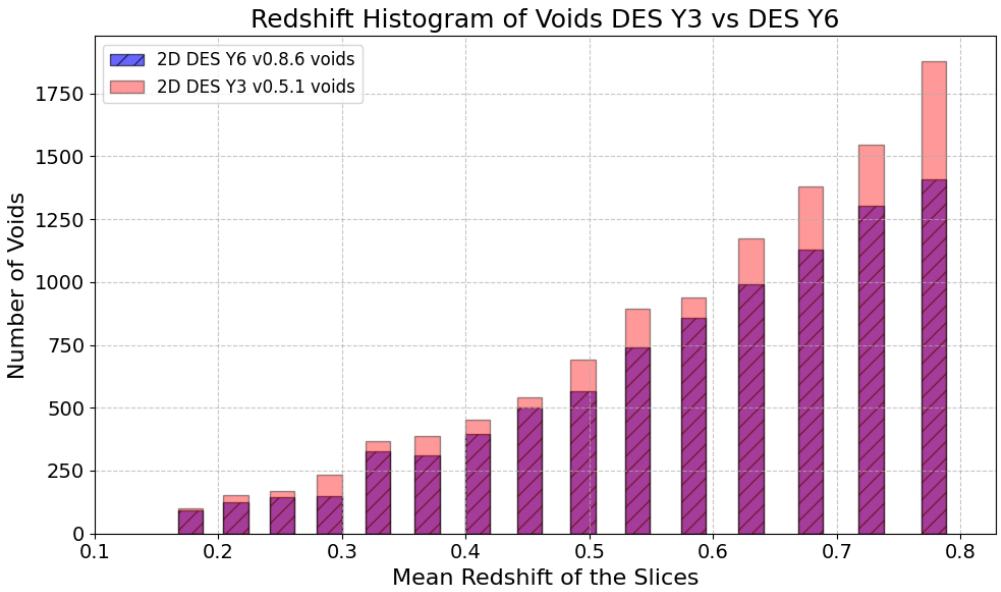

Figure A.7: We use the DES Y6 `redMaGiC` v0.8.6 galaxy catalogue and run a 2D void finder on these tracers to observe changes in void numbers for a potential DES Y6 void study. Our results show that, despite the increase in galaxy density, the number of 2D voids decreases.

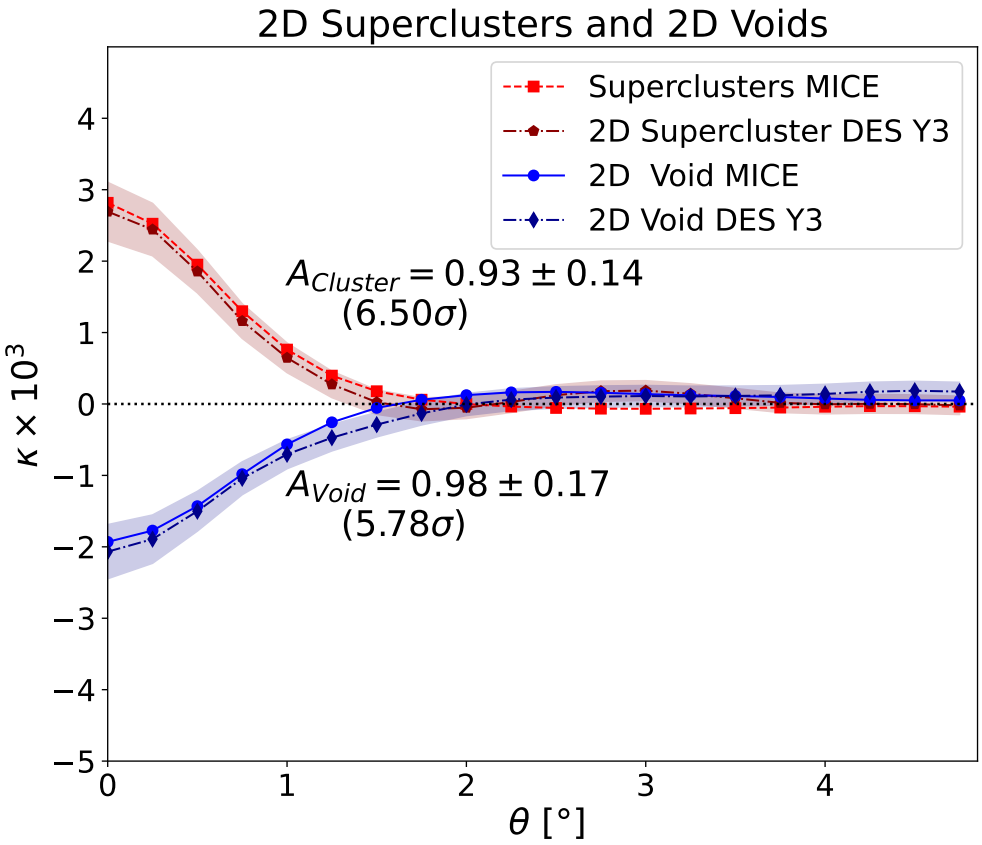

Figure A.8: This figures shows the results obtained without re-scaling the CMB cutouts, maintaining a fixed cutout size irrespective of void size and applying a smoothing scale of FWHM = 1° to the CMB map, consistent with the re-scaling method. The entire error estimation process was conducted using this fixed approach. It is important to note that the detection significances are reduced compared to the re-scaling technique, potentially attributable to the chosen smoothing scale. Nevertheless, the results exhibit strong agreement with MICE, thereby further strengthening the findings in Demirbozan et al. (2024).

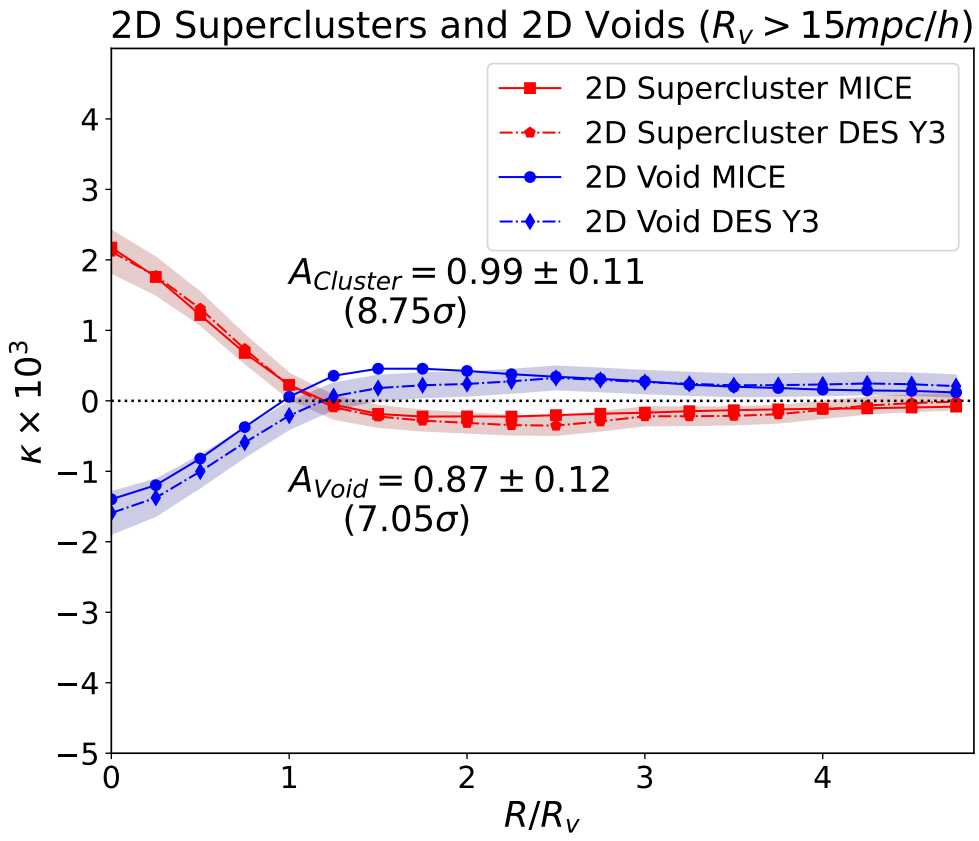

Figure A.9: This figure shows the results when the void catalogue is expanded by including voids with $R_v > 15\ h^{-1}$ Mpc instead of the previous cutoff at $20\ h^{-1}$ Mpc. We observe a significant increase in the signal-to-noise ratio, indicating that the $20\ h^{-1}$ Mpc threshold applied by Sánchez et al. (2016) and Kovács et al. (2022) may not represent a justified value. Again, the results show good agreement with MICE, with an increased S/N, strengthening the results of Demirbozan et al. (2024) even more.

Bibliography

Abbott, B., Abbott, R., Abbott, T., et al. 2016, Physical Review Letters, 116

Abbott, T. M. C., Aguena, M., Alarcon, A., et al. 2022, Phys. Rev. D, 105, 023520

Abbott, T., Abdalla, R., Weller, J., et al. 2019, Physical Review D, 100

Abbott, T., Aguena, M., Alarcon, A., et al. 2023, Physical Review D, 107

Abdalla, E., Abellán, G. F., Aboubrahim, A., et al. 2022, Journal of High Energy Astrophysics, 34, 49

Ade, P., Aguirre, J., Ahmed, Z., et al. 2019, Journal of Cosmology and Astroparticle Physics, 2019, 056

Afshordi, N., Loh, Y.-S., & Strauss, M. A. 2004, Phys. Rev. D, 69, 083524

Alam, S., Ata, M., Bailey, S., et al. 2017, Monthly Notices of the Royal Astronomical Society, 470, 2617

Albrecht, A., & Steinhardt, P. J. 1982, Physical Review Letters, 48, 1220

Alestas, G., & Perivolaropoulos, L. 2021, Monthly Notices of the Royal Astronomical Society, 504, 3956

Alpher, R. A., Bethe, H., & Gamow, G. 1948, Physical Review, 73, 803

Alpher, R. A., & Herman, R. 1948b, Nature, 162, 774

Alpher, R. A., & Herman, R. C. 1948a, Phys. Rev., 74, 1737

Alpher, R. A., & Herman, R. C. 1949, Phys. Rev., 75, 1089

Amendola, L., Appleby, S., Bacon, D., et al. 2013, Living Reviews in Relativity, 16, 6

Amendola, L., Frieman, J. A., & Waga, I. 1999, Monthly Notices of the Royal Astronomical Society, 309, 465

Amon, A., Gruen, D., Troxel, M. A., et al. 2022, Phys. Rev. D, 105, 023514

Arcari, S., Pinetti, E., & Fornengo, N. 2022, Journal of Cosmology and Astroparticle Physics, 2022, 011

Babcock, H. W. 1939, Lick Observatory Bulletin, 19, 41

Bahr-Kalus, B., Parkinson, D., Asorey, J., et al. 2022, Monthly Notices of the Royal Astronomical Society, 517, 3785

Baker, T., Clampitt, J., Jain, B., & Trodden, M. 2018, Physical Review D, 98, 023511

Balkenhol, L., Dutcher, D., Spurio Mancini, A., & d SPT-3G Collaboration. 2023, Physical Review D, 108, 023510

Banik, I., Pittordis, C., Sutherland, W., et al. 2024, Monthly Notices of the Royal Astronomical Society, 527, 4573

Bartelmann, M., & Schneider, P. 2001, Physics Reports, 340, 291–472

Baushev, A. N. 2021, Monthly Notices of the Royal Astronomical Society, 504, L56

Baxter, E. J., Keisler, R., Dodelson, S., et al. 2015, The Astrophysical Journal, 806, 247

Bekenstein, J. D. 2004, Physical Review D, 70, 083509

Benson, A. J., Cole, S., Frenk, C. S., Baugh, C. M., & Lacey, C. G. 2000, Monthly Notices of the Royal Astronomical Society, 311, 793

Berlind, A. A., & Weinberg, D. H. 2002, The Astrophysical Journal, 575, 587

Berti, E., Barausse, E., Cardoso, V., et al. 2015, Classical and Quantum Gravity, 32, 243001

Bertone, G., Hooper, D., & Silk, J. 2005, Physics Reports, 405, 279

Bertotti, B., Iess, L., & Tortora, P. 2003, Nature, 425, 374

Beygu, B., Peletier, R. F., van der Hulst, J. M., et al. 2017, Monthly Notices of the Royal Astronomical Society, 464, 666

Bocquet, S., Grandis, S., Bleem, L. E., et al. 2024, SPT Clusters with DES and HST Weak Lensing. II. Cosmological Constraints from the Abundance of Massive Halos, arXiv:2401.02075

Bond, J. R., Kofman, L., & Pogosyan, D. 1996, Nature, 380, 603

Bos, E. G. P., van de Weygaert, R., Dolag, K., & Pettorino, V. 2012, Monthly Notices of the Royal Astronomical Society, 426, 440

Boughn, S. P., & Crittenden, R. G. 2005, New Astronomy Reviews, 49, 75

Braden, J., Burrage, C., Elder, B., & Saadeh, D. 2021, Journal of Cosmology and Astroparticle Physics, 2021, 010

Brax, P. 2013, Classical and Quantum Gravity, 30, 214005

Burles, S., & Tytler, D. 1998, The Astrophysical Journal, 499, 699

Cai, R.-G., Guo, Z.-K., Wang, S.-J., Yu, W.-W., & Zhou, Y. 2022, Physical Review D, 105, L021301

Cai, Y.-C., Cole, S., Jenkins, A., & Frenk, C. S. 2010, Monthly Notices of the Royal Astronomical Society, 407, 201

Cai, Y.-C., Neyrinck, M., Mao, Q., et al. 2017, Monthly Notices of the Royal Astronomical Society, 466, 3364

Cai, Y.-C., Padilla, N., & Li, B. 2015, Monthly Notices of the Royal Astronomical Society, 451, 1036

Camacho-Ciurana, G., Lee, P., Arsenov, N., et al. 2024, Astronomy & Astrophysics, 689, A171

Carbone, C., Baccigalupi, C., Bartelmann, M., Matarrese, S., & Springel, V. 2009, Monthly Notices of the Royal Astronomical Society, 396, 668–679

Carlip, S. 2001, Reports on Progress in Physics, 64, 885

Carlstrom, J. E., Ade, P. A. R., Aird, K. A., et al. 2011, Publications of the Astronomical Society of the Pacific, 123, 568

Carron, J., & Lewis, A. 2017, Physical Review D, 96, 063510

Cautun, M., Cai, Y.-C., & Frenk, C. S. 2016, Monthly Notices of the Royal Astronomical Society, 457, 2540–2553

Cautun, M., Paillas, E., Cai, Y.-C., et al. 2018, Monthly Notices of the Royal Astronomical Society, 476, 3195

Cawthon, R., Davis, C., Gatti, M., et al. 2018, Monthly Notices of the Royal Astronomical Society, 481, 2427

Chang, C., Vikram, V., Jain, B., et al. 2015, Physical Review Letters, 115, 051301

Chang, C., Pujol, A., Mawdsley, B., et al. 2018, Monthly Notices of the Royal Astronomical Society, 475, 3165–3190

Chantavat, T., Sawangwit, U., & Wandelt, B. D. 2017, The Astrophysical Journal, 836, 156

Chevallier, M., & Polarski, D. 2001, International Journal of Modern Physics D, 10, 213–223

Clampitt, J., Cai, Y.-C., & Li, B. 2013, Monthly Notices of the Royal Astronomical Society, 431, 749

Clampitt, J., & Jain, B. 2015, Monthly Notices of the Royal Astronomical Society, 454, 3357

Clifton, T., Ferreira, P. G., Padilla, A., & Skordis, C. 2012, Physics Reports, 513, 1

Colin, J., Mohayaee, R., Rameez, M., & Sarkar, S. 2019, Astronomy & Astrophysics, 631, L13

Condon, J. J., Cotton, W. D., Greisen, E. W., et al. 1998, The Astronomical Journal, 115, 1693

Contarini, S., Verza, G., Pisani, A., et al. 2022, Euclid: Cosmological Forecasts from the Void Size Function

Cooke, R. J., Pettini, M., & Steidel, C. C. 2018, The Astrophysical Journal, 855, 102

Cousinou, M. C., Pisani, A., Tilquin, A., et al. 2019, Astronomy and Computing, 27, 53

Crittenden, R. G., & Turok, N. 1996, Physical Review Letters, 76, 575

Crocce, M., Castander, F. J., Gaztañaga, E., Fosalba, P., & Carretero, J. 2015, Monthly Notices of the Royal Astronomical Society, 453, 1513

Cruz, M., Tucci, M., Martínez-González, E., & Vielva, P. 2006, Monthly Notices of the Royal Astronomical Society, 369, 57

Curtis, O., McDonough, B., & Brainerd, T. G. 2024, The Astrophysical Journal, 962, 58

Dark Energy Survey Collaboration. 2016, Monthly Notices of the Royal Astronomical Society, 460, 1270

Das, S., & Bode, P. 2008, The Astrophysical Journal, 682, 1–13

Das, S., Sherwin, B. D., Aguirre, P., et al. 2011, Physical Review Letters, 107, 021301

Davies, C. T., Cautun, M., & Li, B. 2018, Monthly Notices of the Royal Astronomical Society, 480, L101

Davies, C. T., Cautun, M., & Li, B. 2019, Monthly Notices of the Royal Astronomical Society, 490, 4907

Davis, M., Efstathiou, G., Frenk, C. S., & White, S. D. M. 1985, The Astrophysical Journal, 292, 371

Daylan, T., Finkbeiner, D. P., Hooper, D., et al. 2016, Physics of the Dark Universe, 12, 1

De Felice, A., & Tsujikawa, S. 2010, Living Reviews in Relativity, 13, 3

Demirbozan, U., Nadathur, S., Ferrero, I., et al. 2024, Monthly Notices of the Royal Astronomical Society, 534, 2328

DES Collaboration. 2024a, arXiv:2401.02929

DES Collaboration, e. a. 2024b, arXiv e-prints, arXiv:2402.10696

DESI Collaboration, Aghamousa, A., Aguilar, J., et al. 2016a, arXiv e-prints, arXiv:1611.00037

DESI Collaboration, Aghamousa, A., Aguilar, J., et al. 2016b, arXiv e-prints, arXiv:1611.00036

Di Valentino, E., Mena, O., Pan, S., et al. 2021, Classical and Quantum Gravity, 38, 153001

Domínguez-Gómez, J., Pérez, I., Ruiz-Lara, T., et al. 2023, Nature, 619, 269

Dong, C., Loy, C. C., He, K., & Tang, X. 2014, in Lecture Notes in Computer Science, Vol. 8692, Computer Vision – ECCV 2014, ed. D. Fleet, T. Pajdla, B. Schiele, & T. Tuytelaars, Springer, Cham, 184

Dong, F., Yu, Y., Zhang, J., Yang, X., & Zhang, P. 2021, Monthly Notices of the Royal Astronomical Society, 500, 3838

Dunkley, J., Komatsu, E., Nolta, M. R., et al. 2009a, The Astrophysical Journal Supplement Series, 180, 306

Dunkley, J., Komatsu, E., Nolta, M. R., et al. 2009b, The Astrophysical Journal Supplement Series, 180, 306–329

Dvali, G., Gabadadze, G., & Porrati, M. 2000, Physics Letters B, 485, 208–214

Dyson, F. W., Eddington, A. S., & Davidson, C. 1920, Philosophical Transactions of the Royal Society of London Series A, 220, 291

Einasto, J., Saar, E., Kaasik, A., & Chernin, A. D. 1974, Nature, 252, 111

Einstein, A. 1905, Annalen der Physik, 323, 639

Einstein, A. 1915, Sitzungsberichte der Preussischen Akademie der Wissenschaften zu Berlin (Mathematical Physics), 778, available at the library of the Max Planck Institute for the History of Science

Eisenstein, D. J., Zehavi, I., Hogg, D. W., et al. 2005, The Astrophysical Journal, 633, 560

Elvin-Poole, J., Crocce, M., Ross, A. J., et al. 2018, Physical Review D, 98, 042006

Fang, Y., Hamaus, N., Jain, B., et al. 2019, Monthly Notices of the Royal Astronomical Society, 490, 3573

Ferrero, I., Crocce, M., Tutusaus, I., et al. 2021, Astronomy & Astrophysics, 656, A106

Finelli, F., García-Bellido, J., Kovács, A., Paci, F., & Szapudi, I. 2016, Monthly Notices of the Royal Astronomical Society, 455, 1246

Flaugher, B., Diehl, H. T., Honscheid, K., & The DES Collaboration. 2015, The Astronomical Journal, 150, 150

Fosalba, P., & Gaztañaga, E. 2004, Monthly Notices of the Royal Astronomical Society, 350, L37

Fosalba, P., Gaztañaga, E., & Castander, F. J. 2003, Astrophysical Journal Letters, 597, L89

Fosalba, P., Gaztañaga, E., Castander, F. J., & Manera, M. 2008, Monthly Notices of the Royal Astronomical Society, 391, 435

Fosalba, P., Gaztañaga, E., Castander, F. J., & Crocce, M. 2015, Monthly Notices of the Royal Astronomical Society, 447, 1319

Fowler, J. W., Niemack, M. D., Dicker, S. R., et al. 2007, Applied Optics, 46, 3444

Francis, C. L., & Peacock, J. A. 2010, Monthly Notices of the Royal Astronomical Society, 406, 2

Freedman, W. L., Madore, B. F., Jang, I. S., et al. 2024, arXiv e-prints, arXiv:2408.06153

Frenk, C. S., & White, S. D. M. 2012, Annalen der Physik, 524, 507

Gaia Collaboration, Prusti, T., de Bruijne, J. H. J., et al. 2016, Astronomy & Astrophysics, 595, A1

Gatti, M., Sheldon, E., Amon, A., et al. 2021, Monthly Notices of the Royal Astronomical Society, 504, 4312

Gautam, A., Crocker, R. M., Ferrario, L., et al. 2022, Nature Astronomy, 6, 703

Giannantonio, T., Fosalba, P., Cawthon, R., et al. 2016, Monthly Notices of the Royal Astronomical Society, 456, 3213

Giannini, G., Alarcon, A., Gatti, M., et al. 2024, Monthly Notices of the Royal Astronomical Society, 527, 2010

Goodfellow, I. J., Pouget-Abadie, J., Mirza, M., et al. 2014, in Advances in neural information processing systems, 2672

Górski, K. M., Hivon, E., Banday, A. J., et al. 2005, The Astrophysical Journal, 622, 759

Granett, B. R., Neyrinck, M. C., & Szapudi, I. 2008, The Astrophysical Journal, 683, L99

Granett, B. R., Neyrinck, M. C., & Szapudi, I. 2008, Astrophysical Journal Letters, 683, L99

Granett, B. R., Neyrinck, M. C., & Szapudi, I. 2008, ApJL, 683, L99

Gregory, S. A., & Thompson, L. A. 1978, The Astrophysical Journal, 222, 784

Gruen, D., Friedrich, O., Amara, A., et al. 2016, Monthly Notices of the Royal Astronomical Society, 455, 3367

Guth, A. H. 1981, Physical Review D, 23, 347

Hahn, C., Lemos, P., Parker, L., et al. 2024, Nature Astronomy

Hamaus, N., Cousinou, M.-C., Pisani, A., et al. 2017, Journal of Cosmology and Astroparticle Physics, 7, 014

Hamaus, N., Pisani, A., Choi, J.-A., et al. 2020, Journal of Cosmology and Astroparticle Physics, 2020, 023

Hamaus, N., Pisani, A., Sutter, P. M., et al. 2016, Physical Review Letters, 117, 091302

Hamaus, N., Sutter, P. M., & Wandelt, B. D. 2014, Physical Review Letters, 112, 251302

Hamilton, A. J. S. 1998, in Astrophysics and Space Science Library, Vol. 231, The Evolving Universe, ed. D. Hamilton, 185

Hang, Q., Alam, S., Cai, Y.-C., & Peacock, J. A. 2021, Monthly Notices of the Royal Astronomical Society, 507, 510

Hartlap, J., Simon, P., & Schneider, P. 2007, Astronomy & Astrophysics, 464, 399

Hawken, A. J., Aubert, M., Pisani, A., et al. 2020, Journal of Cosmology and Astroparticle Physics, 2020, 012

He, S., Alam, S., Ferraro, S., Chen, Y.-C., & Ho, S. 2018, Nature Astronomy, 2, 401

Heymans, C., Tröster, T., Asgari, M., et al. 2021, Astronomy & Astrophysics, 646, A140

Hinshaw, G., et al. 2013, The Astrophysical Journal Supplement Series, 208, 19

Hlozek, R., Grin, D., Marsh, D. J. E., & Ferreira, P. G. 2015, Physical Review D, 91, 103512

Ho, S., Hirata, C., Padmanabhan, N., Seljak, U., & Bahcall, N. 2008, Physical Review D, 78, 043519

Honscheid, K., & DePoy, D. L. 2008, The Dark Energy Camera (DECam), arXiv:0810.3600

Hotchkiss, S., Nadathur, S., Gottlöber, S., et al. 2015, Monthly Notices of the Royal Astronomical Society, 446, 1321

Hu, J. P., Wang, Y. Y., Hu, J., & Wang, F. Y. 2024, Astronomy & Astrophysics, 681, A88

Hu, W. 2000, Physical Review D, 62, 043007, arXiv:astro-ph/0001303

Hu, W., & Okamoto, T. 2002a, The Astrophysical Journal, 574, 566, arXiv:astro-ph/0111606

Hu, W., & Okamoto, T. 2002b, The Astrophysical Journal, 574, 566

Hu, W., & Sawicki, I. 2007, Physical Review D, 76, 064004

Hubble, E. 1929, Proceedings of the National Academy of Science, 15, 168

Hubble, E. P. 1926, The Astrophysical Journal, 64, 321

Huterer, D. 2002, Physical Review D, 65

Ibitoye, A., Dai, W.-M., Ma, Y.-Z., et al. 2024, The Astrophysical Journal Supplement Series, 270, 16

Ilić, S., Langer, M., & Douspis, M. 2013, Astronomy & Astrophysics, 556, A51

Ivezić, Ž., Kahn, S. M., Tyson, J. A., et al. 2019, The Astrophysical Journal, 873, 111

Jeffrey, N., Gatti, M., Chang, C., et al. 2021, Monthly Notices of the Royal Astronomical Society, 505, 4626

Jing, Y. P., Mo, H. J., & Börner, G. 1998, The Astrophysical Journal, 494, 1

Joyce, A., Jain, B., Khoury, J., & Trodden, M. 2015, Physics Reports, 568, 1

Jungman, G., Kamionkowski, M., & Griest, K. 1996, Physics Reports, 267, 195

Kahn, F. D., & Woltjer, L. 1959, The Astrophysical Journal, 130, 705

Kaiser, N. 1984, Astrophysical Journal Letters, 284, L9

Kaiser, N. 1987, Monthly Notices of the Royal Astronomical Society, 227, 1

Kaiser, N. 1992, The Astrophysical Journal, 388, 272

Kaiser, N., & Squires, G. 1993, The Astrophysical Journal, 404, 441

Khalife, A. R., Zanjani, M. B., Galli, S., et al. 2024, Journal of Cosmology and Astroparticle Physics, 2024, 059

Khoury, J., & Weltman, A. 2004, Physical Review D, 69, 044026

Kilbinger, M. 2015, Reports on Progress in Physics, 78, 086901

Kirk, D., Omori, Y., Benoit-Lévy, A., et al. 2016, Monthly Notices of the Royal Astronomical Society, 459, 21

Kirshner, R. P., Oemler, A., J., Schechter, P. L., & Shectman, S. A. 1981, Astrophysical Journal Letters, 248, L57

Kitaura, F.-S., Chuang, C.-H., Liang, Y., et al. 2016, Physical Review Letters, 116, 171301

Kovács, A. 2018, Monthly Notices of the Royal Astronomical Society, 475, 1777

Kovács, A., Beck, R., Smith, A., et al. 2022, Monthly Notices of the Royal Astronomical Society, 513, 15

Kovács, A., Beck, R., Szapudi, I., et al. 2020, Monthly Notices of the Royal Astronomical Society, 499, 320

Kovács, A., Sánchez, C., García-Bellido, J., & the DES collaboration. 2017, Monthly Notices of the Royal Astronomical Society, 465, 4166

Kovács, A., Sanchez, C., García-Bellido, J., et al. 2019, Monthly Notices of the Royal Astronomical Society, 484, 5267

Kovács, A., Jeffrey, N., Gatti, M., et al. 2021, Monthly Notices of the Royal Astronomical Society, 510, 216

Kovács, A., Vielzeuf, P., Ferrero, I., et al. 2022, Monthly Notices of the Royal Astronomical Society, 515, 4417

Krause, E., Chang, T.-C., Doré, O., & Umetsu, K. 2013, Astrophysical Journal Letters, 762, L20

Kravtsov, A. V., Vikhlinin, A. A., & Meshcheryakov, A. V. 2018, Astronomy Letters, 44, 8

Kreisch, C. D., Pisani, A., Carbone, C., et al. 2019, Monthly Notices of the Royal Astronomical Society, 488, 4413

Lang, D. 2014, The Astronomical Journal, 147, 108

Laureijs, R., Amiaux, J., Arduini, S., et al. 2011, arXiv e-prints, arXiv:1110.3193

Lavaux, G., & Wandelt, B. D. 2012, The Astrophysical Journal, 754, 109

Ledig, C., Theis, L., Huszár, F., et al. 2017a, in 2017 IEEE Conference on Computer Vision and Pattern Recognition (CVPR), 105

Ledig, C., Theis, L., Huszár, F., et al. 2017b, in Proceedings of the IEEE conference on computer vision and pattern recognition, 4681

Lee, J., & Park, D. 2009, Astrophysical Journal Letters, 696, L10

Lemaître, G. 1927, Annales de la Société Scientifique de Bruxelles, 47, 49, bibliographic Code: 1927ASSB...47...49L

Lesgourgues, J., Mangano, G., Miele, G., & Pastor, S. 2013, Neutrino Cosmology (Cambridge University Press)

Lesgourgues, J., & Pastor. 2006, Physics Reports, 429, 307

Levi, M., Bebek, C., Beers, T., et al. 2013, arXiv:1308.0847

Lewis, A., & Challinor, A. 2006, Physics Reports, 429, 1, arXiv:astro-ph/0601594

Lewis, G. F., & Brewer, B. J. 2023, Nature Astronomy, 7, 1265

Li, B., Zhao, G.-B., & Koyama, K. 2012, Monthly Notices of the Royal Astronomical Society, 421, 3481

Li, P., Ilayda Onur, I., Dodelson, S., & Chaudhari, S. 2022, arXiv e-prints, arXiv:2205.07368

Li, Y., Ni, Y., Croft, R. A. C., et al. 2021, Proceedings of the National Academy of Science, 118, e2022038118

Liddle, A. R., & Lyth, D. H. 2000, Cosmological Inflation and Large-Scale Structure (Cambridge, UK: Cambridge University Press)

Linde, A. 1982, Physics Letters B, 108, 389

Linder, E. V. 2003, Physical Review Letters, 90

Linder, E. V. 2007, The Mirage of w=-1, arXiv:0708.0024

Liu, J., Petri, A., Haiman, Z., et al. 2015, Physical Review D, 91, 063507

Macaulay, E., Nichol, R. C., Bacon, D., et al. 2019, Monthly Notices of the Royal Astronomical Society, 486, 2184

Mackenzie, R., Shanks, T., Bremer, M. N., et al. 2017, Monthly Notices of the Royal Astronomical Society, 470, 2328

Madhavacheril, M. S., Qu, F. J., Sherwin, B. D., et al. 2024, The Astrophysical Journal, 962, 113

Madhavacheril, M., Sehgal, N., Allison, R., et al. 2015, Physical Review Letters, 114, 151302

Mandelbaum, R. 2018, Annual Review of Astronomy and Astrophysics, 56, 393

Manzotti, A., & Dodelson, S. 2014, Physical Review D, 90, 123009

Martino, M. C., & Sheth, R. K. 2009, arxiv:0911.1829

Massara, E., Percival, W. J., Dalal, N., et al. 2022, Monthly Notices of the Royal Astronomical Society, 517, 4458

Massara, E., Villaescusa-Navarro, F., Viel, M., & Sutter, P. M. 2015, Journal of Cosmology and Astroparticle Physics, 2015, 018

Mauland, R., Elgarøy, Ø., Mota, D. F., & Winther, H. A. 2023, Astronomy & Astrophysics, 674, A185

McEwen, J. D., Hobson, M. P., & Lasenby, A. N. 2008, IEEE Transactions on Signal Processing, 56, 3813

Melchior, P., Sutter, P. M., Sheldon, E. S., Krause, E., & Wandelt, B. D. 2014, Monthly Notices of the Royal Astronomical Society, 440, 2922

Migkas, K. 2024, arXiv e-prints, arXiv:2406.01752

Milgrom, M. 1983, The Astrophysical Journal, 270, 365

Minor, Q., Gad-Nasr, S., Kaplinghat, M., & Vegetti, S. 2021, Monthly Notices of the Royal Astronomical Society, 507, 1662

Mohammad, F. G., & Percival, W. J. 2022, Monthly Notices of the Royal Astronomical Society, 514, 1289

Moresco, M., Amati, L., Amendola, L., et al. 2022, Living Reviews in Relativity, 25, 6

Nadathur, S. 2016, Monthly Notices of the Royal Astronomical Society, 461, 358

Nadathur, S., Carter, P. M., Percival, W. J., Winther, H. A., & Bautista, J. E. 2019, Physical Review D, 100, 023504

Nadathur, S., Carter, P. M., Percival, W. J., Winther, H. A., & Bautista, J. E. 2019, Physical Review D, 100

Nadathur, S., Carter, P. M., Percival, W. J., Winther, H. A., & Bautista, J. E. 2019, REVOLVER: REal-space VOid Locations from suVEy Reconstruction, Astrophysics Source Code Library, record ascl:1907.023

Nadathur, S., Carter, P., & Percival, W. J. 2018, Monthly Notices of the Royal Astronomical Society, 482, 2459–2470

Nadathur, S., & Crittenden, R. 2016, Astrophysical Journal Letters, 830, L19

Nadathur, S., & Hotchkiss, S. 2014, Monthly Notices of the Royal Astronomical Society, 440, 1248

Nadathur, S., & Hotchkiss, S. 2015a, Monthly Notices of the Royal Astronomical Society, 454, 2228

Nadathur, S., & Hotchkiss, S. 2015b, Monthly Notices of the Royal Astronomical Society, 454, 889

Nadathur, S., Hotchkiss, S., & Crittenden, R. 2017, Monthly Notices of the Royal Astronomical Society, 467, 4067

Nadathur, S., Lavinto, M., Hotchkiss, S., & Räsänen, S. 2014, Physical Review D, 90, 103510

Nadathur, S., & Percival, W. J. 2019, Monthly Notices of the Royal Astronomical Society, 483, 3472

Nadathur, S., Percival, W. J., Beutler, F., & Winther, H. A. 2020a, Physical Review Letters, 124, 221301

Nadathur, S., Woodfinden, A., Percival, W. J., et al. 2020b, Monthly Notices of the Royal Astronomical Society, 499, 4140

Naidoo, K., Benoit-Lévy, A., & Lahav, O. 2016, Monthly Notices of the Royal Astronomical Society: Letters, 459, L71

Naidoo, K., Jaber, M., Hellwing, W. A., & Bilicki, M. 2024, Physical Review D, 109, 083511

NASA. 2020, Astronomy Picture of the Day Debate

Navarro, J. F., Frenk, C. S., & White, S. D. M. 1996, The Astrophysical Journal, 462, 563

Neyrinck, M. C. 2008, arXiv e-prints, 386, 2101

Neyrinck, M. C., Gnedin, N. Y., & Hamilton, A. J. S. 2005, Monthly Notices of the Royal Astronomical Society, 356, 1222

Nolta, M. R., Wright, E. L., & et al. 2004, ApJL, 608, 10

Ntelis, P., & Morris, A. 2023, Found. Phys., 53, 29

Năstase, H. 2019, Fundamental Theories of Physics, Vol. 197, Cosmology and String Theory (Springer)

Offer, A., & Lahav, O. 2023, The Social Value of Dark Energy, arXiv:2305.17982

Oguri, M., Miyazaki, S., Hikage, C., et al. 2018, Publications of the Astronomical Society of Japan, 70, S26

Okamoto, T., & Hu, W. 2003, Physical Review D, 67, 083002

Ostriker, J. P., & Peebles, P. J. E. 1973, The Astrophysical Journal, 186, 467

Ostriker, J. P., Peebles, P. J. E., & Yahil, A. 1974, The Astrophysical Journal Letters, 193, L1

Owusu, S., da Silveira Ferreira, P., Notari, A., & Quartin, M. 2023, Journal of Cosmology and Astroparticle Physics, 2023, 040

Padilla, N. D., Ceccarelli, L., & Lambas, D. G. 2005, Monthly Notices of the Royal Astronomical Society, 363, 977

Paillas, E., Cautun, M., Li, B., et al. 2019, Monthly Notices of the Royal Astronomical Society, 484, 1149

Pan, Z., Bianchini, F., Wu, W. L. K., et al. 2023, Physical Review D, 108, 122005

Pandey, S., Krause, E., DeRose, J., et al. 2022, Physical Review D, 106, 043520

Patiri, S. G., Betancort-Rijo, J., & Prada, F. 2012, Astronomy & Astrophysics, 541, L4

Paz, D., Lares, M., Ceccarelli, L., Padilla, N., & Lambas, D. G. 2013, Monthly Notices of the Royal Astronomical Society, 436, 3480

Peacock, J. A., & Smith, R. E. 2000, Monthly Notices of the Royal Astronomical Society, 318, 1144

Pearson, R., & Zahn, O. 2014, Physical Review D, 89, 043516

Peebles, P. 2014, EPJ H, 39, 205

Peebles, P. J. E. 1980, The Large-Scale Structure of the Universe (Princeton University Press)

Penzias, A. A., & Wilson, R. W. 1965, The Astrophysical Journal, 142, 419

Percival, W. J., Friedrich, O., Sellentin, E., & Heavens, A. 2021, Monthly Notices of the Royal Astronomical Society, 510, 3207

Perico, E., Voivodic, R., Lima, M., & Mota, D. 2019, Astronomy & Astrophysics

Perlmutter, S., Aldering, G., Goldhaber, G., & et al. 1999, The Astrophysical Journal, 517, 565

Petroff, M. A., Addison, G. E., Bennett, C. L., & Weiland, J. L. 2020, The Astrophysical Journal, 903, 104

Philcox, O. H. E., Farren, G. S., Sherwin, B. D., Baxter, E. J., & Brout, D. J. 2022, Phys. Rev. D, 106, 063530

Pisani, A., Sutter, P. M., Hamaus, N., et al. 2015, Physical Review D, 92, 083531

Pisani, A., Massara, E., Spergel, D. N., et al. 2019, Bulletin of the American Astronomical Society, 51, 40

Planck 2015 results. XVI. 2015, arxiv:1506.07135

Planck Collaboration. 2018, arXiv e-prints, arXiv:1807.06209

Planck Collaboration. 2020, Astronomy & Astrophysics, 641, A1

Planck Collaboration, Ade, P. A. R., Aghanim, N., Armitage-Caplan, C., & al., e. 2013, arxiv:1303.5083

Planck Collaboration, Aghanim, N., Akrami, Y., et al. 2020a, Astronomy & Astrophysics, 641, A6

Planck Collaboration, Adam, R., Ade, P. A. R., et al. 2016a, Astronomy & Astrophysics, 594, A9

Planck Collaboration, Ade, P. A. R., Aghanim, N., et al. 2016b, Astronomy & Astrophysics, 594, A15

Planck Collaboration, Ade, P. A. R., Aghanim, N., et al. 2016c, Astronomy & Astrophysics, 594, A24

Planck Collaboration, Aghanim, N., Akrami, Y., et al. 2020b, Astronomy & Astrophysics, 641, A8

Platen, E., van de Weygaert, R., & Jones, B. J. T. 2007, Monthly Notices of the Royal Astronomical Society, 380, 551

Pollina, G., Hamaus, N., Paech, K., et al. 2019, Monthly Notices of the Royal Astronomical Society, 487, 2836

Porredon, A., Crocce, M., Fosalba, P., et al. 2021, Physical Review D, 103, 043503

Porredon, A., Crocce, M., Elvin-Poole, J., et al. 2022, Physical Review D, 106

Press, W. H., & Schechter, P. 1974, The Astrophysical Journal, 187, 425

Qu, F. J., Sherwin, B. D., Madhavacheril, M. S., et al. 2024, The Astrophysical Journal, 962, 112

Radinović, S., Winther, H. A., Nadathur, S., et al. 2024, arXiv e-prints, arXiv:2407.02699

Raghunathan, S., Nadathur, S., Sherwin, B. D., & Whitehorn, N. 2020, The Astrophysical Journal, 890, 168

Raghunathan, S., Patil, S., Baxter, E., et al. 2019, The Astrophysical Journal, 872, 170

Rassat, A., Land, K., Lahav, O., & Abdalla, F. B. 2007, Monthly Notices of the Royal Astronomical Society, 377, 1085

Rees, M. J., & Sciama, D. W. 1968, Nature, 217, 511

Reid, B., Ho, S., Padmanabhan, N., et al. 2016, Monthly Notices of the Royal Astronomical Society, 455, 1553

Riess, A. G., Casertano, S., Yuan, W., et al. 2021, The Astrophysical Journal, 908, L6

Riess, A. G., Casertano, S., Yuan, W., Macri, L. M., & Scolnic, D. 2019, The Astrophysical Journal, 876, 85

Riess, A. G., Filippenko, A. V., Challis, P., et al. 1998, The Astronomical Journal, 116, 1009

Riess, A. G., et al. 2022, The Astrophysical Journal, 934, L7

Ross, A. J., Ho, S., Cuesta, A. J., et al. 2011, Monthly Notices of the Royal Astronomical Society, 417, 1350

Rovelli, C. 1998, Living Rev. Rel., 1, 1

Rozo, E., Rykoff, E. S., Abate, A., et al. 2016, Monthly Notices of the Royal Astronomical Society, 461, 1431

Ruhl, J., Ade, P. A. R., Carlstrom, J. E., et al. 2004, in Society of Photo-Optical Instrumentation Engineers (SPIE) Conference Series, Vol. 5498, Z-Spec: a broadband millimeter-wave grating spectrometer: design, construction, and first cryogenic measurements, ed. C. M. Bradford, P. A. R. Ade, J. E. Aguirre, J. J. Bock, M. Dragovan, L. Duband, L. Earle, J. Glenn, H. Matsuhara, B. J. Naylor, H. T. Nguyen, M. Yun, & J. Zmuidzinas, 11

Rykoff, E. S., Rozo, E., Busha, M. T., et al. 2014, The Astrophysical Journal, 785, 104

Sachs, R. K., & Wolfe, A. M. 1967, ApJL, 147, 73

Sánchez, C., Clampitt, J., Kovacs, A., et al. 2016, Monthly Notices of the Royal Astronomical Society, 465, 746

Schäfer, B. M., Pfrommer, C., Hell, R. M., & Bartelmann, M. 2006, Monthly Notices of the Royal Astronomical Society, 370, 1713

Schmittfull, M., & Seljak, U. 2018, Physical Review D, 97, 123540

Schöneberg, N., Lesgourgues, J., & Hooper, D. C. 2019, Journal of Cosmology and Astroparticle Physics, 10, 029

Schuster, N., Hamaus, N., Dolag, K., & Weller, J. 2024, Journal of Cosmology and Astroparticle Physics, 2024, 065

Secco, L. F., Samuroff, S., Krause, E., et al. 2022, Physical Review D, 105, 023515

Secrest, N. J., von Hausegger, S., Rameez, M., et al. 2021, Astrophysical Journal Letters, 908, L51

Seljak, U. 2000, Monthly Notices of the Royal Astronomical Society, 318, 203

Shaikh, S., Harrison, I., van Engelen, A., et al. 2024, Monthly Notices of the Royal Astronomical Society, 528, 2112

Sherwin, B. D., Dunkley, J., Das, S., et al. 2011, Physical Review Letters, 107, 021302

Sheth, R. K., & van de Weygaert, R. 2004, Monthly Notices of the Royal Astronomical Society, 350, 517

Shimakawa, R., Higuchi, Y., Shirasaki, M., et al. 2021, Monthly Notices of the Royal Astronomical Society, 503, 3896

Simon, J. D., Geha, M., Minor, Q. E., et al. 2011, The Astrophysical Journal, 733, 46

Smith, K. M., & Huterer, D. 2010, Monthly Notices of the Royal Astronomical Society, 403, 2

Springel, V. 2005, Monthly Notices of the Royal Astronomical Society, 364, 1105

Springel, V., White, S. D. M., Jenkins, A., et al. 2005, Nature, 435, 629

Stein, G., Alvarez, M. A., Bond, J. R., van Engelen, A., & Battaglia, N. 2020, Journal of Cosmology and Astroparticle Physics, 2020, 012

Storey-Fisher, K., Hogg, D. W., Rix, H.-W., et al. 2024, The Astrophysical Journal, 964, 69

Stoughton, C., Lupton, R. H., Bernardi, M., et al. 2002, The Astronomical Journal, 123, 485

Sutter, P. M., Carlesi, E., Wandelt, B. D., & Knebe, A. 2015a, Monthly Notices of the Royal Astronomical Society: Letters, 446, L1

Sutter, P. M., Lavaux, G., Hamaus, N., et al. 2014, Monthly Notices of the Royal Astronomical Society, 442, 462

Sutter, P. M., Lavaux, G., Wandelt, B. D., & Weinberg, D. H. 2012, The Astrophysical Journal, 761, 187

Sutter, P. M., Pisani, A., Wandelt, B. D., & Weinberg, D. H. 2014, Monthly Notices of the Royal Astronomical Society, 443, 2983

Sutter, P. M., Lavaux, G., Hamaus, N., et al. 2015b, Astronomy and Computing, 9, 1

Takahashi, R., Hamana, T., Shirasaki, M., et al. 2017, The Astrophysical Journal, 850, 24

Tang, L., Lin, H.-N., Liu, L., & Li, X. 2023, Chinese Physics C, 47, 125101

Tanimura, H., Aghanim, N., Bonjean, V., Malavasi, N., & Douspis, M. 2020, Astronomy & Astrophysics, 637, A41

Tauber, J. A., Mandolesi, N., Puget, J. L., et al. 2010, Astronomy & Astrophysics, 520, A1

Tegmark, M., Blanton, M. R., Strauss, M. A., et al. 2004, The Astrophysical Journal, 606, 702

Tinker, J. L., Sheldon, E. S., Wechsler, R. H., et al. 2012, The Astrophysical Journal, 745, 16

Vagnozzi, S., & Loeb, A. 2022, The Astrophysical Journal Letters, 939, L22

Vainshtein, A. I. 1972, Physics Letters B, 39, 393

Vallés-Pérez, D., Quilis, V., & Planelles, S. 2021, Astrophysical Journal Letters, 920, L2

van de Weygaert, R., Shandarin, S., Saar, E., & Einasto, J., eds. 2016, IAU Symposium, Vol. 308, The Zeldovich Universe: Genesis and Growth of the Cosmic Web

van Engelen, A., Keisler, R., Zahn, O., et al. 2012, The Astrophysical Journal, 756, 142

Vegetti, S., Koopmans, L. V. E., Bolton, A., Treu, T., & Gavazzi, R. 2010, Monthly Notices of the Royal Astronomical Society, 408, 1969

Verde, L., Schöneberg, N., & Gil-Marín, H. 2023, arXiv e-prints, arXiv:2311.13305

Verde, L., Treu, T., & Riess, A. G. 2019, Nature Astronomy, 3, 891

Verrier, U. J. J. L. 1859, Comptes Rendus de l'Académie des Sciences, 49, 379, presented to the French Academy of Sciences

Verza, G., Pisani, A., Carbone, C., Hamaus, N., & Guzzo, L. 2019, arXiv e-prints, arXiv:1906.00409

Vielzeuf, P., Calabrese, M., Carbone, C., Fabbian, G., & Baccigalupi, C. 2023, Journal of Cosmology and Astroparticle Physics, 2023, 010

Vielzeuf, P., Kovács, A., Demirbozan, U., et al. 2021, Monthly Notices of the Royal Astronomical Society, 500, 464

Vikram, V., Chang, C., Jain, B., et al. 2015, Phys. Rev. D, 92, 022006

Villaescusa-Navarro, F., Vogelsberger, M., Viel, M., & Loeb, A. 2013, Monthly Notices of the Royal Astronomical Society, 431, 3670

Vincenzi, M., Brout, D., Armstrong, P., et al. 2024, The Dark Energy Survey Supernova Program: Cosmological Analysis and Systematic Uncertainties, arXiv:2401.02945

Voivodic, R., Lima, M., Llinares, C., & Mota, D. 2016, Physical Review D, 95, 024018

Wang, B. Y., Pisani, A., Villaescusa-Navarro, F., & Wandelt, B. D. 2023, The Astrophysical Journal, 955, 131

Wang, D., & Mena, O. 2024, arXiv e-prints, arXiv:2402.18248

Wen, R. Y., Hergt, L. T., Afshordi, N., & Scott, D. 2024, Journal of Cosmology and Astroparticle Physics, 2024, 045

White, R. M. T., Davis, T. M., Lewis, G. F., et al. 2024, arXiv:2406.05050

Will, C. M. 2014, Living Reviews in Relativity, 17

Woodfinden, A., Nadathur, S., Percival, W. J., et al. 2022, Monthly Notices of the Royal Astronomical Society, 516, 4307

Woodfinden, A., Percival, W. J., Nadathur, S., et al. 2023, Monthly Notices of the Royal Astronomical Society, 523, 6360

Yan, Y.-P., Wang, G.-J., Li, S.-Y., & Xia, J.-Q. 2023, The Astrophysical Journal, 947, 29

Zaldarriaga, M., & Seljak, U. c. v. 1999, Phys. Rev. D, 59, 123507

Zhang, G., Li, Z., Liu, J., et al. 2019, arXiv e-prints, arXiv:1910.07553

Zhao, R., Mu, X., Gsponer, R., et al. 2024, Monthly Notices of the Royal Astronomical Society, 532, 783

Zheng, Z., Coil, A. L., & Zehavi, I. 2007, The Astrophysical Journal, 667, 760

Zheng, Z., Zehavi, I., Eisenstein, D. J., Weinberg, D. H., & Jing, Y. P. 2009, The Astrophysical Journal, 707, 554

Zwicky, F. 1933, Helvetica Physica Acta, 6, 110